THESIS / THÈSE

MASTER IN CHEMISTRY RESEARCH FOCUS

Modeling and analysis of nonlinear optical properties of dyes embedded in increasingly complex environments, up to the lipid bilayer
A quantum mechanics and molecular dynamics study

Bouquiaux, Charlotte

Award date:
2019

Awarding institution:
University of Namur

Link to publication

Université de Namur
Faculté des Sciences

MODELING AND ANALYSIS OF NONLINEAR OPTICAL PROPERTIES OF DYES EMBEDDED IN INCREASINGLY COMPLEX ENVIRONMENTS, UP TO THE LIPID BILAYER. A QUANTUM MECHANICS AND MOLECULAR DYNAMICS STUDY

Mémoire présenté pour l'obtention

du grade académique de Master Chimie «Chimie du Vivant et des Nanomatériaux»: Finalité Approfondie

Charlotte BOUQUIAUX

Janvier 2019

UNIVERSITE DE NAMUR
Faculté des Sciences
Secrétariat du Département de Chimie
Rue de Bruxelles 61 - 5000 NAMUR
Téléphone : +32(0)81 72.54.44 - Téléfax : +32(0)81 72.54.40
E-mail : enseignement.chimie@unamur.be - www.unamur.be/sciences

MODÉLISATION ET ANALYSE DES PROPRIÉTÉS OPTIQUES NON LINÉAIRES DE COLORANTS INSÉRÉS DANS DES ENVIRONNEMENTS DE PLUS EN PLUS COMPLEXES, JUSQU'À LA BICOUCHE LIPIDIQUE. UNE ETUDE DE MÉCANIQUE QUANTIQUE ET DYNAMIQUE MOLÉCULAIRE

BOUQUIAUX Charlotte

Résumé

La plupart des molécules biologiques possèdent peu de groupements avec des propriétés optiques exploitables. L'utilisation de chromophores extrinsèques peut donc augmenter le contraste des tissus lors de la collection de données de microscopie. Les colorants de la famille AminoNaphtylEthenylPyridinium (ANEP) sont habituellement utilisés comme sondes fluorescentes. De plus, ces chromophores sont, depuis quelques années, également employés dans le cadre de la Génrération de Seconde Harmonique (SHG). En effet, la SHG un phénomène optique non linéaire (NLO) du second ordre qui possède, par rapport à la fluorescence, l'avantage que le signal ne provient que de regions non centrosymetriques, ce qui fournit de meilleurs contrastes.

Ce travail se concentre sur la characterisation des propriétés SHG des chromophores du type ANEP, la première hyperpolarisabilité (β) au niveau moléculaire, en employant des méthodes de chimie quantique. En particulier, une procédure à deux étapes a été élaborée et mise au point afin de décrire ces colorants dans des environnements de plus en plus complexes, de la phase gas diluée, à la solution, pour finir par les bicouches lipidiques (ici construite à partir de dipalmitoyl-phosphatidylcholine, DPPC). La première étape de la méthode utilise la Dynamique Moléculaire (MD) pour prendre en compte le comportement dynamique du chromophore d'intérêt, ainsi que ses environnements. Pour ces simulations, les champs de forces sont soit validés par confrontation à des données expériementales soit re-parametrisés en fonction de calculs de théorie de la fonctionnelle de la densité. Ensuite, pour des snapshots sélectionés extraits des simulations de MD, les réponses NLO du chromophore avec son environnement le plus proche sont calculées en utilisant la théorie de la fonctionnelle de la densité dépendante du temps. Les simulations ont révélé une augmentation significative de la réponse SHG en prenant en compte les fluctuations géométriques, ainsi qu'en allant de la solution aqueuse à la bicouche lipidique. Dans tous les cas, ces variations peuvent être reliées à des variations géométriques (alternance de longueurs de liaison et angles dihèdres). Une étude compémentaire s'est interessée aux relations structure-β dans des composés dérivés d'ANEP, à l'analyse de l'impact de la taille des substituants et du pont π-conjugué ainsi que la position de substituants donneur/accepteur, avec le but de concevoir des colorants SHG efficaces.

UNIVERSITE DE NAMUR
Faculté des Sciences
Secrétariat du Département de Chimie
Rue de Bruxelles 61 - 5000 NAMUR
Téléphone : +32(0)81 72.54.44 - Téléfax : +32(0)81 72.54.40
E-mail : enseignement.chimie@unamur.be - www.unamur.be/sciences

MODELING AND ANALYSIS OF NONLINEAR OPTICAL PROPERTIES OF DYES EMBEDDED IN INCREASINGLY COMPLEX ENVIRONMENTS, UP TO THE LIPID BILAYER. A QUANTUM MECHANICS AND MOLECULAR DYNAMICS STUDY

BOUQUIAUX Charlotte

Abstract

Most biomolecules possess few natural moieties with exploitable optical properties for bioimaging. The use of exogenous dyes can improve the contrast in tissues for being detected by commercially available microscopes. AminoNaphtylEthenylPyridinium (ANEP) dyes constitute a family of broadly employed fluorescent dyes. Moreover, in the last few years, these compounds have gained interest in the field of Second Harmonic Generation (SHG) imaging. Indeed, SHG is a nonlinear optical (NLO) phenomenon, which possesses the advantage, with respect to fluorescence, that only non-centrosymmetric compounds and structures can produce a signal, leading to stronger contrasts. This work focuses on the characterization of the SHG properties of ANEP-like dyes, the first hyperpolarizability (β) at the molecular scale, by employing methods of theoretical chemistry. In particular, a two-step procedure has been elaborated and tuned in order to describe these chromophores in increasingly complex environments, from the diluted gas phase, to the solution, and finally, to lipid bilayers (here built from dipalmitoylphosphatidylcholine, DPPC). The first step of the method employs Molecular Dynamics (MD) to account for the dynamical behavior of the target chromophores, as well as of their environment. For those simulations the force fields are either validated with respect to experimental data or re-parameterized with respect to density functional theory calculations. Then, for selected snapshots extracted from the MD simulations, the NLO responses of the chromophore with its nearest environment are computed using time-dependent density functional theory. Simulations have revealed a strong increase of the SHG response when accounting for geometrical fluctuations, as well as when going for aqueous solutions to the lipid bilayer environment. In all cases, these variations have been traced back by analyzing the corresponding geometrical changes (bond length alternation and dihedral angles). Complementary studies have investigated the structure-β property relationships in ANEP-derivatives, analyzing the impact of the size of the substituents and of the π-conjugated linker as well as of the position of donor/acceptor substituents, with the aim of designing efficient SHG dyes.

A la fin de la rédaction de ce manuscrit, l'écriture de ces remerciements semble arriver comme une note finale pour cloturer cette belle année de travail. Travail qui a été rendu possible grâce à l'aide et à la collaboration de nombreuses personnes, tant dans ma vie privée que dans ma vie aux facultés. Dans ces quelques lignes, j'espère n'oublier personne.

Je voudrais premièrement remercier le Professeur Frédéric Caster et le Docteur Claire Tonnelé de l'Unniversité de Bordeaux pour leur aide précieuse dans la re-parametrization du champs de force.

Bien entendu, je remercie également le Professeur Benoît Champagne qui m'a transmit le goût de la chimie théorique et qui m'a donné l'opportunité de réaliser ce travail. Ses connaissances et son expertises ont permis d'enrichir ainsi que des guider mes recherches. Plus largement, j'ai également une pensée pour tous les membres du Laboratoire de Chimie Théorique. Ils ont tous, à leur manière, égayé cette année. Que ce soit les moments partagés lors des temps de midi ou en dehors des facs. Un merci tout particulier Pierre, toujours disponible pour venir saupoudrer un peu de sa magie noire lorsqu'un calcul ou un programme plante. Et évidemment, comment faire pour ne pas mentionner Jean qui a réussi à "s'infiltrer" autant dans ma vie privée que dans ma vie au laboratoire. Merci de garder ton calme quand je n'y arrive pas.

Je voudrais de plus remercier tout ceux avec qui je termine mon Master pour toutes les bonnes soirées passés ensemble depuis cinq ans. Je tiens également à les féliciter : les gars, on l'a fait ! Parmis une majorité de garçons, quelques filles se dégagent du lot. Manon, Mathilde, et Lorraine merci d'avoir été là depuis le début. Et particulièrement Manon, avec qui j'ai partagé le même bureau, mais aussi bien plus que ça ! On a rigolé ensemble, on a eu nos crises de nerfs ensemble, et surtout, le plus important, on a rémitté ensemble.

Il est temps maintenant de remercier ma famille, qui a été un soutien inébranlable depuis toujours. Que ce soit pour mes études, ou pour d'autres projets, mes parents se sont toujours montrés compréhensifs et présents.

Acronyms

NLO	nonlinear optical
1PEF	one-photon excited fluorescence
2PEF	two-photon excited fluorescence
SFG	Sum Frequency Generation
SHG	Second Harmonic Generation
SHIM	Second Harmonic Imaging Microscopy
HRS	hyper-Rayleigh scattering
EFISHG	electric-field-induced SHG
ECM	extra-cellular matrix
DR	depolarization ratio
CT	charge transfer
ANEP	AminoNaphtylEthenylPyridinium
Di-4-ANEPPS	di-4-AminoNaphtenyl-Pyridinium-PropylSulfonate
Di-8-ANEPPS	di-8-AminoNaphtenyl-Pyridinium-PropylSulfonate
DPPC	dipalmitoylphosphatidylcholine
QM	Quantum Mechanics
HF	Hartree-Fock
LCAO	Linear Combination of Atomic Orbitals
STO	Slater Type Orbital
TDHF	time-dependent Hartree-Fock
DFT	density functional theory
H-K	Hohenberg and Kohn
KS	Kohn-Sham
XC	exchange-correlation
LDA	local density approximation
GGA	generalized gradient approximation
MP2	second-order Møller-Plesset
RMS	root mean square
TDDFT	time-dependent density functional theory
IEFPCM	Integral Equation Formalism of the Polarizable Continuum Model
SAS	Solvent Accessible Surface

SES	Solvent Excluding Surface
ASC	apparent surface charge
MM	Molecular Mechanics
FF	force field
MD	Molecular Dynamics
PBC	periodic boundary conditions
PME	particle mesh Ewald
ESP	electrostatic potential
SPC/Fw	simple point charge for flexible water
GAFF	Generalized Amber Force Field
C36	CHARMM36
BLA	bond length alternation
TSA	two-sate approximation
PES	potential energy scan
RDF	radial distribution function
RMSD	root mean square deviation
NMR	nuclear magnetic resonance
DMR	deuterated NMR
DMPC	dimyristoylglycerophosphocholine

Contents

Part I

Introduction

Chapter 1

Context and motivation

The ultimate goal of this project is to study and design nonlinear optical (NLO) molecular probes for imaging biological structures and for probing the electrical potential across lipid bilayer membranes. Most biomolecules possess few natural moieties with exploitable optical properties[1] -with the exception of structural proteins such as collagen[2] and cellulose[3]- so that the use of exogenous dyes can improve the contrast in tissues for being detected by commercially available nonlinear microscopes.[4–10] Dyes can also be used to monitor changes in membrane potential.[4,8,9,11–13] The electrical signalling between cells has a crucial role in the control and in the flow of information and movement of substances between cells. It is therefore of particular importance to understand these biological processes. The use of dyes can, for example, offer the opportunity to monitor neuronal electrical activity of systems not accessible to microelectrodes or when microelectrode measurements are unsuitable or inadequate.[14,15]

Chapter 2

Elements of nonlinear optics

2.1 General aspects

In linear and nonlinear microscopy, several phenomena operate in parallel, depending on the illumination wavelength(s).[16] They differ by the number of photons implicated as well as by the nature of states involved. Fluorescence is characterized by absorption of one or two photon(s) of energy $\hbar\omega$ (pulsation ω) to a real (electronically excited) state, giving rise to one-photon excited fluorescence (1PEF) and two-photon excited fluorescence (2PEF or TPEF), respectively. In these phenomena, after excitation, relaxation to the lowest vibrational level of the first electronic excited state occurs. Then, within a period determined by the excited state lifetime, a photon is emitted returning the chromophore to its electronic ground state. Fluorescence is therefore an incoherent radiative absorption and reemission process.[17] 1PEF is a linear optical phenomenon, of which the intensity is proportional to the incident light intensity. On the other hand, 2PEF is nonlinear and its intensity depends quadratically on the incident intensity.

Besides fluorescence, Second Harmonic Generation (SHG) is a coherent process where pairs of incident photons having the same energy are converted in photons of twice this energy. Like 2PEF, SHG intensity depends quadratically on the incident intensity. SHG can be viewed as a special case of Sum Frequency Generation (SFG) where a new photon is created at a pulsation being the sum of those of the two incident photons. SFG is typically used by combining infrared and UV/visible lights to probe the vibrational signatures of interfaces. As a matter of fact, this master thesis focuses on the use of SHG to perform biological imaging and membrane potential monitoring. The most common SHG phenomenon (and SFG by extension) occurs through the

interaction with a virtual excited state, a very short-lived and unobservable quantum state. Still, when the energy of the signal gets close or corresponds to an electronic absorption band, the SHG signal can be enhanced. These phenomena are known as near resonance and resonance enhanced SHG.[4] All the presented phenomena are illustrated in Figure 2.1, which offers a non-exhaustive list of linear and nonlinear optical processes.

For isotropic media like gases and solutions, the most widely employed method to measure SHG intensities is based on the Hyper-Rayleigh scattering (HRS) phenomenon, which is an incoherent second-order NLO process. Although coherent SHG in isotropic media is forbidden for reasons of symmetry, incoherent HRS is allowed because the non-centrosymmetric molecules act as individual and uncorrelated scattering centers.[18] On the other hand, in the case of electric-field-induced SHG (EFISHG), an external static electric field is applied to the gas/solution in order to induce a preferential orientation, which breaks the isotropic character and therefore allows the generation of a coherent SHG signal.[16,19,20]
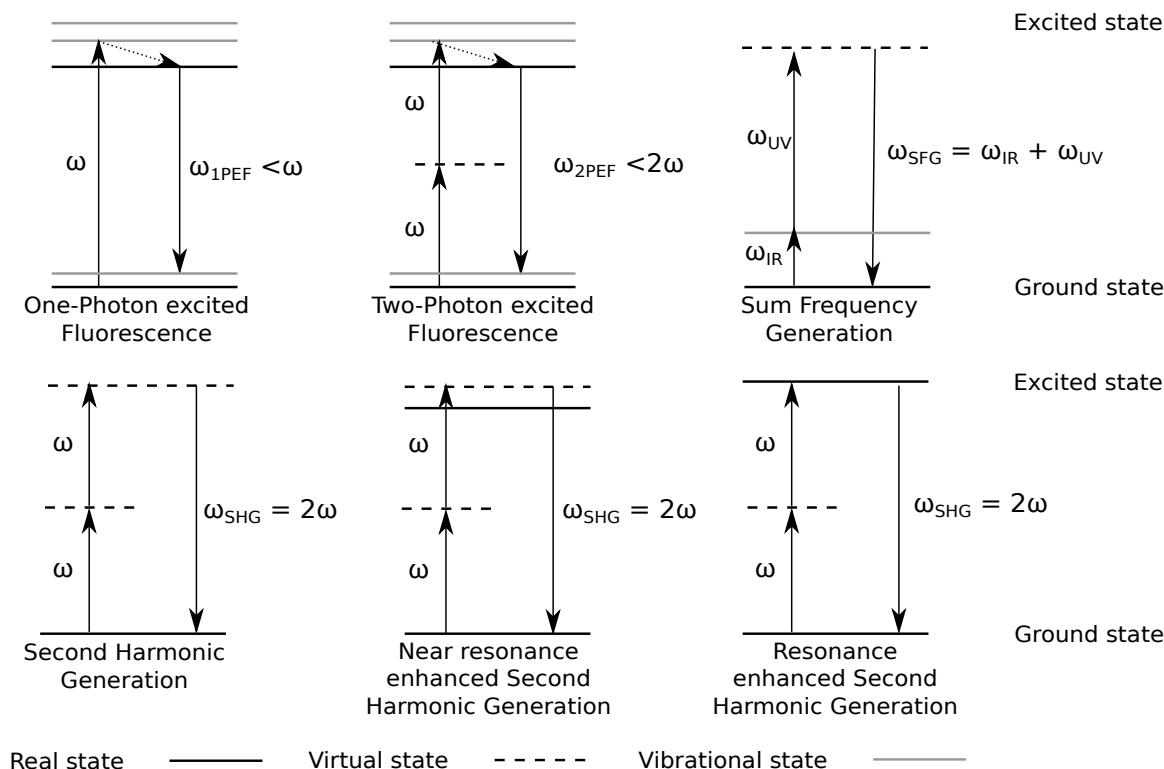
Figure 2.1 – Jablonsky diagrams of selected linear and nonlinear optical processes.

2.2 Focus on Second Harmonic Generation Imaging and comparison to fluorescence

Second Harmonic Generation is a second-order NLO process that was first demonstrated by Franken et al.[21] in crystalline quartz in 1961. It was then developed by Shen,[22] Eisenthal,[23] and others for the study of surfaces and artificial monolayers. The used of SHG in microscopy was proposed by Sheppard et al[24] in 1977. Since, there has been an expansion in the use of Second Harmonic Imaging Microscopy (SHIM), partially thanks to large advances in laser technology.[4] As said before, Second Harmonic Generation (SHG) is a nonabsorptive phenomenon that consists of the conversion of pairs of incident photons of ω frequency into single photons of 2ω frequency when an intense and focused laser beam passes through a NLO-active medium, as shown in Figure 2.2.
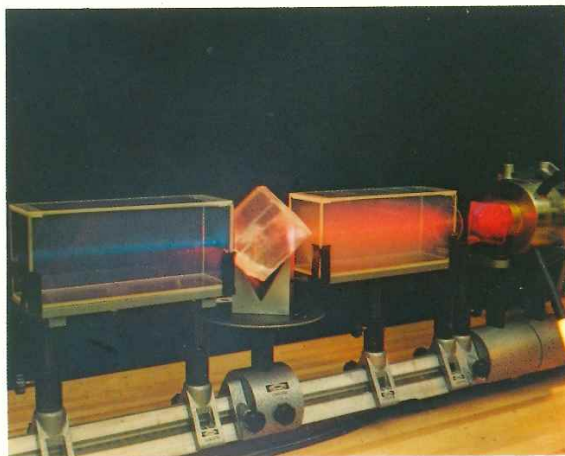
Figure 2.2 – Illustration of the SHG phenomenon: a beam of red photons are converted into one beam of purple photons after interaction with the a NLO-active crystal.

In SHG, a commonly used incident light wavelength is 1064 nm (achieved using a Nd:YAG laser[25]), which is in the infrared region and should prevent photodamage and photobleaching.[11,16] This is not the case for the fluorescence, especially 1PEF, for which a more energetic ultraviolet incident photon has to be absorbed.[16] Furthermore, fluorescence relies on the formation of excited states, meaning that the electron density reorganizes, passing to a higher energy and more reactive state. As a consequence, the bonds involved in this electronic reorganization weaken and can, for example, be more sensitive to a nucleophilic attack.

Moreover, SHG requires an environment without center of symmetry, such as an interfacial

region, to produce a signal. Because of this symmetry restriction, SHG is an ideal technique to study the biophysics of model membranes, and membrane physiology of living cells, in which one leaflet has been stained by a probe molecule.[4] The observed signal is only due to the non-centrosymmetric molecules and molecular assemblies, whereas in fluorescence, a background is usually observed arising also from isotropic regions. This ensures, generally, a better imaging contrast with SHG than with fluorescence.

Another advantage of SHG, is that it retains the phase and directional information after interaction with the sample. Furthermore, SHG signals have well-defined polarizations. Information about the molecular organization of the chromophore can therefore be extracted from SHG imaging data, by taking advantage of the SHG polarization anisotropy. In fluorescence, when absorbed and, after excited state relaxations, subsequently emitted, photons do not retain this information.[16,26]

Finally, fluorescence measurements are relatively insensitive toward membrane potential variations, showing changes of only approximately 10 % for a 100 mV potential change.[4,11,27] In contrast, when using a model membrane, it was previously demonstrated that the SHG intensity was strongly modulated by an applied electric field.[4] Some studies have shown that this technique could show changes of approximately 20 %,[13,28] being a performance twice as good as for the fluorescence. Furthermore, differences in lipid composition of cell membranes could also be monitored by SHG.[10]

Despite all these remarks, SHG and TPEF are often considered to be complementary techniques. These two types of microscopy imply the use of the same near-infrared incident laser beam, and can be used simultaneously.[16] Figure 2.3 shows an exemple of application of both techniques in human fibrotic liver.[29] On the one hand, SHG images reveal the over-production of fibrillar collagen of the extra-cellular matrix (ECM), which are associated with chronic liver diseases. These are not visible on the image, which showed the typical autofluorescence of the liver. Furthermore, as expected, SHG provides higher signal-to-background contrast and resolution because of the absence of signal from the hepatocyte. Finally, simultaneous TPEF and SHG imaging clearly revealed ECM distribution around hepatocytes. This demonstrates the complementarity between these two imaging techniques.[29]
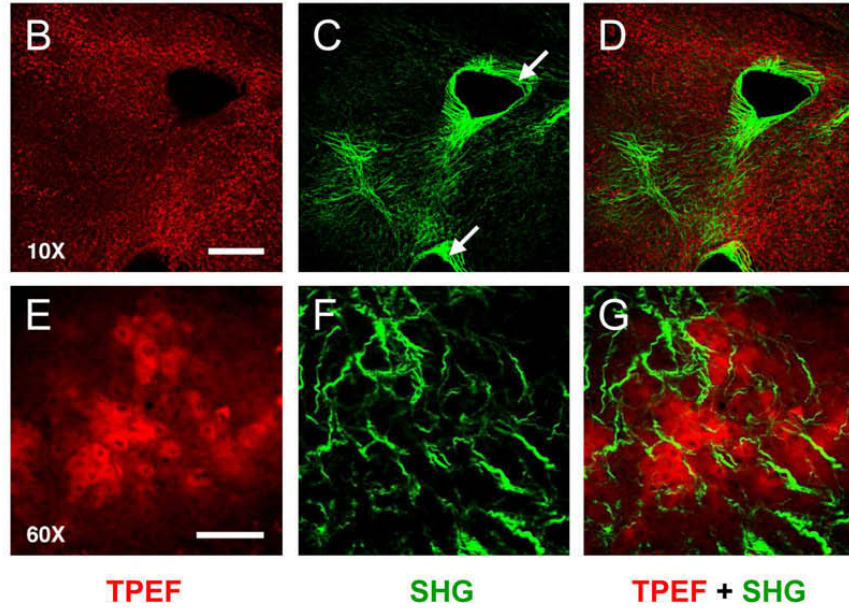
Figure 2.3 – Nonlinear microscopy in human fibrotic liver. Comparison between TPEF imaging, SHG imaging, and simultaneous TPEF and SHG imaging. Images B-D are presented with a low magnification (10x), whereas images E-G were taken with a 60x objective. Scale bars are, respectively, 250 and 60 μm.[29]

2.3   First hyperpolarizability

At the molecular level, the SHG phenomenon is caused by the first hyperpolarizability. The latter describes the second-order nonlinear response of the dipole moment to optical electric fields:

$$\mu(E) = \mu_0 + \alpha E + \frac{1}{2}\beta E^2 + \frac{1}{6}\gamma E^3 + ... \tag{2.1}$$

where μ_0 is the permanent dipole moment, E is the electric field, α is the polarizability, β is the first hyperpolarizability, and γ is the second hyperpolarizability. Here a Taylor expansion has been used. This expansion refers to T convention whereas a power series expansion might also have been used and would referred to B convention.[30] This nonlinear dependence is then schematized in Figure 2.4.
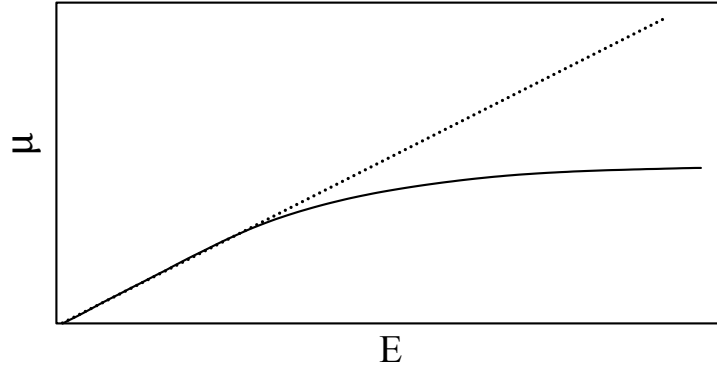
Figure 2.4 – Evolution of the dipole moment as a function of the strength of the electric field.

Owing to the vector nature of the dipole moment and electric field, β is a rank-3 tensor with 27 components:

$$\beta = \begin{pmatrix} \beta_{xxx} & \beta_{xyy} & \beta_{xzz} & \beta_{xyz} & \beta_{xzy} & \beta_{xxz} & \beta_{xzx} & \beta_{xxy} & \beta_{xyx} \\ \beta_{yxx} & \beta_{yyy} & \beta_{yzz} & \beta_{yyz} & \beta_{yzy} & \beta_{yxz} & \beta_{yzx} & \beta_{yxy} & \beta_{yyx} \\ \beta_{zxx} & \beta_{zyy} & \beta_{zzz} & \beta_{zyz} & \beta_{zzy} & \beta_{zxz} & \beta_{zzx} & \beta_{zxy} & \beta_{zyx} \end{pmatrix} \tag{2.2}$$

Noticing this, one understands that the β tensor contains a lot of information on the molecules, much more, for instance, than the dipole moment, which has only three components. The β values reported in this work correspond to the quantities that can be obtained using the experimental hyper-Rayleigh scattering (HRS) method[31]: β_{HRS} ant its depolarization ratio (DR). The expression of β_{HRS} involves tensor averages over the molecular orientations (Equation 2.3). The DR is defined as the ratio between the scattered intensities obtained when the incident light is vertically- and horizontally-polarized (Equation 2.4) for a vertically-polarized scattered light detected at 90° with respect to the direction of incidence. These DRs allow to divide up the molecules into three categories based on the shape of the NLO-phore. This can be illustrated by considering ideal cases, i.e. molecules with perfect or nearly perfect symmetry. For octupolar molecules, like CCl_4, the only non-vanishing tensor component is β_{xyz}. The corresponding DR is equal to 1.5. One-dimensional push-pull π-conjugated systems have only one component, β_{zzz}, and the DR becomes equal to 5. The depolarization ratio tends to 9 for fully dipolar molecules, like acetonitrile.[31]

$$\beta_{\mathrm{HRS}}(-2\omega;\omega,\omega) = \sqrt{\langle \beta_{\mathrm{ZZZ}}^2 \rangle + \langle \beta_{\mathrm{ZXX}}^2 \rangle} \tag{2.3}$$

$$DR = \frac{\langle \beta_{\mathrm{ZZZ}}^2 \rangle}{\langle \beta_{\mathrm{ZXX}}^2 \rangle} \tag{2.4}$$

2.4   SHG molecular probes

The design of a dye for SHG imaging requires fine tuning a number of molecular properties. Firstly, the chromophore should have a high molecular first hyperpolarizability (at the wavelength of illumination).[16] This is the case of linear push-pull π-conjugated systems. These compounds consist of an electron acceptor moiety and an electron donor moiety connected by a π-conjugated path,[32,33] which are at the origin of i) a low-energy charge transfer (CT) excited state (E_{eg}, Equation 2.5), ii) a high oscillator strength (f_{eg}, Equation 2.6), and iii) a large variation of dipole moment between the ground and excited state ($\Delta\mu_{eg}$, Equation 2.7). μ_{eg} is the transition dipole moment between the ground and excited states.

$$E_{eg} = E_e - E_g \tag{2.5}$$

$$f_{eg} = \frac{2}{3} E_{eg} \mu_{eg}^2 \tag{2.6}$$

$$\Delta\mu_{eg} = \mu_e - \mu_g \tag{2.7}$$

A push-pull molecule can be viewed as a mixture between a neutral and a charge-separated resonance form. It has been shown that the first hyperpolarizability of these systems can be analyzed, in first approximation, within the two-state approximation, as expressed in Equation 2.8.[34,35]

$$\beta = 6 \, \frac{\mu_{eg}^2 \Delta\mu_{eg}}{E_{eg}^2} \tag{2.8}$$

On the basis of this expression, several studies have shown how the molecular β values can be optimized by adding suitable acceptor and donor moieties at the ends of the π-conjugated path, as well as, by increasing the length of this path. However, there is a limit: when the bridge length increases, the dye solubility in aqueous media decreases and the stability to photodamage is re-

duced. The chromophore should also have a high affinity for the biological systems it is designed to probe and to be rapidly inserted.[16]

The AminoNaphtylEthenylPyridinium (ANEP) dyes, developped by Loew and colleagues,[14,15] correspond to that description. These push-pull compounds are often used as fluorescent probes, but in the last few years, they have also gained interest in the field of SHG imaging. They are styryl amphiphilic dyes having a hydrophobic part composed of alkyl chains acting as membrane anchors and a hydrophilic group, which can interact with the polar head of the lipid. As a consequence, the chromophore aligns approximately perpendicularly to the membrane/aqueous interface. They all possess the advantage to be stable. Moreover, toxicity and photodynamical effects are low for most imaging applications.[9] In addition, they exhibit a direct electronic response to alterations in the membrane potential[28] and they are currently among the most used fast potentiometric probes, which are capable of following submillisecond membrane-potential changes.[13] Among the ANEP-like compounds, of which a few are presented in Figure 2.5, the di-4-ANEPPS is generally the most used one, thanks to its ability to readily intercalate into the cell membrane. However, in some cells it can rapidly be internalized and distributed between the inner and outer leaflets of the membrane.[15] This induces symmetry and therefore cancels out SHG signal, as mentioned before. To solve this issue, a dye with longer hydrocarbon tails, like di-8-ANEPPS, is often used.

(a)   (b)

(c)   (d)
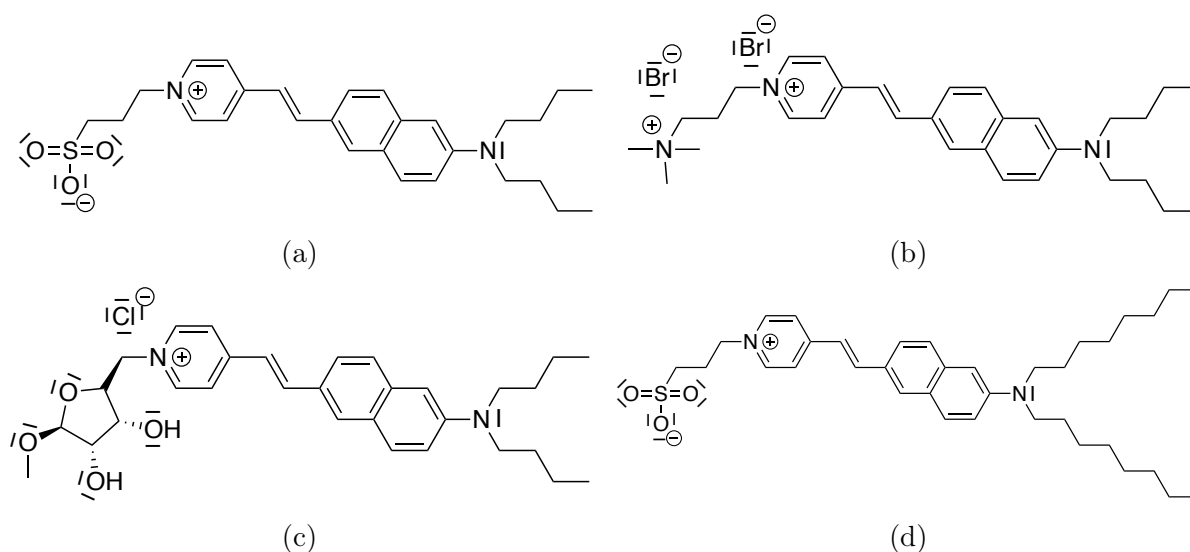
Figure 2.5 – **(a)** Di-4-ANEPPS; **(b)** Di-4-ANEPSQ ;**(c)** JPW-1259, and **d)** Di-8-ANEPPS.

Over the years, several techniques were developed to further enhance to SHG signal. For example, a chiral group can be added to the dye to weaken the symmetry of the system, allowing

SHG even in cases where the two leaflets are stained. For that purpose, the JPW-1259 (Figure 2.5c), for example, was developped.[4,11,15] In the study of Campagnola et al.,[4] the advantage of using this chiral dye was exposed against the performance of an achiral one, the di-4-ANEPPS. Figure 2.6 demonstrates that, as explained before, di-4-ANEPPS stains both leaflets of the membrane and therefore no coherent SHG images can be obtained. On the contrary, when using JPW-1259 as labelling probe, the SHG and TPEF images are essentially identical.
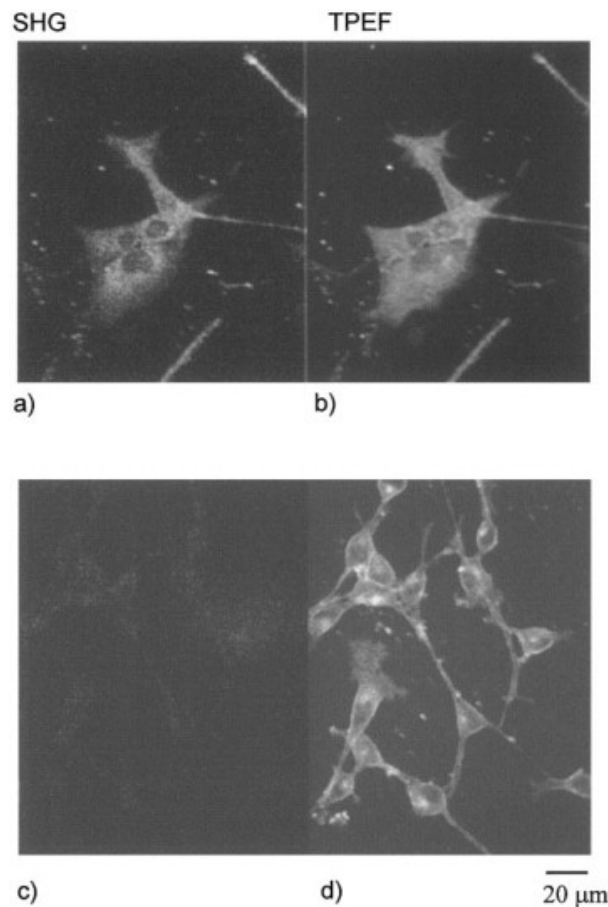
Figure 2.6 – **(a)** SHG and **(b)** TPEF images of JPW-1259-stained 3T3 fibroblast cells, and **(c)** SHG and **(d)** TPEF images of di-4-ANEPPS-stained 3T3 fibroblast cells.[4]

Furthermore, the SHG signal can be enhanced by using metallic nano-particles because they possess localized plasmon surface states. When a light source oscillates at the same pulsation as a plasmon mode, it is excited and strong electromagnetic field is generated. If the nano-particle is complexed to an anti-body, it is possible to direct it to specific sites in a cell membrane and enhance selectively the SHG signal of dye molecules in close proximity, as shown in Figure 2.7.[11,36]
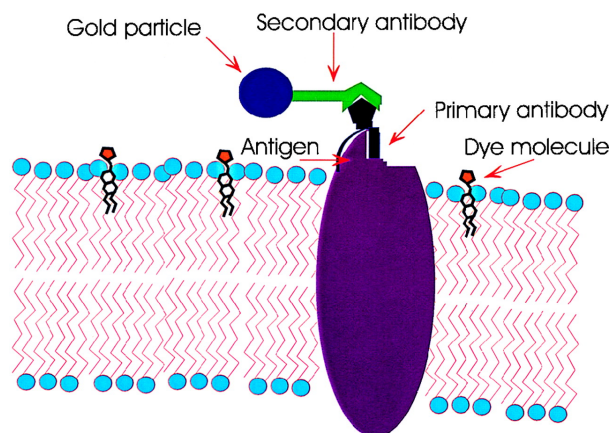
Figure 2.7 – Representation of the relationship between gold nano-particles bound to an antigenic site on the membrane and a dye intercalated within the lipids.[36]

As mentioned before, the magnitude of SHG can also be enhanced when the energy of the signal overlaps with or correspond to an electronic absorption band.[4] Obviously, this is to the detriment of the molecular stability.

Chapter 3

Lipid structures and characteristics

In this Chapter, the structure of the cellular membranes is briefly discussed, with a focus on the lipid molecules. Indeed, bilayer membranes are mostly composed of glycerophospholipids, shingolipids, and sterols (mainly cholesterol in mammals). In addition, proteins can also be embedded in the membrane.[37] Lipids are organic amphipathic compounds, meaning that they possess a hydrophilic or polar headgroup and a hydrophobic or nonpolar moeity. Because of the dominant nature of the hydrophobic portion they are characterized by low solubility in water.[38] The most abundant membrane lipids are the phospholipids. They have a polar headgroup and two hydrophobic hydrocarbon tails. The tails are usually fatty acids. They can differ in length and saturation. The presence or not of one or more double bonds is important because it can influence the ability of the phospholipid molecules to pack against one another, thereby affecting the fluidity of the membrane.[37] The phospholipid shown in Figure 3.1 is the dipalmitoylphosphatidylcholine (DPPC). The latter was chosen to pursue this study for several reasons. First of all, the DPPC is a fully saturated lipid. Each double bond creates a small kink in the tail, the choice of DPPC avoids dealing with the conformation of the double bond. The head group of DPPC is a zwitterion with a positive charge distributed over the choline group and a negative charge on the phosphate group. Overall, it is globally a neutral molecule so that no counter-ions need to be considered during the MD simulations. Finally, MD simulations using DPPC are well described throughout the literature and give a starting point for this work. We simulated the biologically relevant L-enantiomer.

Lipid molecules assemble spontaneously into micelles or bilayers depending on their shapes (Figure 3.2). In aqueous media, both organizations bury the hydrophobic parts of the lipids in
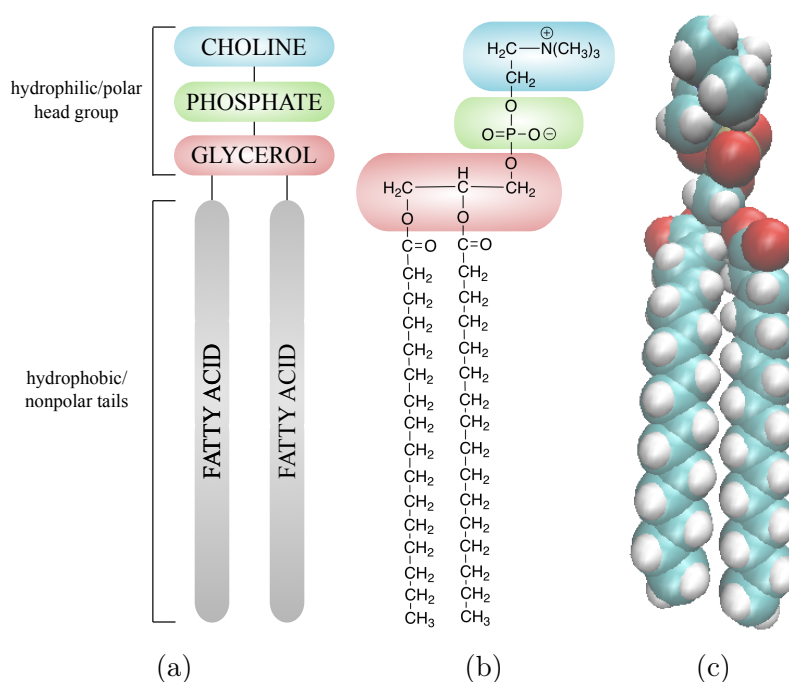
Figure 3.1 – Phosphatidylcholine example: dipalmitoylphosphatidylcholine (DPPC) represented **(a)** schematically; **(b)** by semi-developed formula, and **(c)** as a space-filling model.

the interior so that they are in intimate contact and expose their hydrophilic parts to water. In spherical micelles, the tails are inside and, in bilayers, the hydrophobic tails are sandwiched between the hydrophilic head groups. These assemblies are stabilized by non-covalent forces (driven by the hydrophobic effect) that are sufficiently strong to maintain the integrity of the structure.[38] Being cylindrical, phospholipid molecules spontaneously form bilayers in aqueous environments.[37] Furthermore, the curvature of the membrane is influenced by the relative size of the headgroup and the hydrophobic tails.[39]

The variety of fatty acids and their linkage positions as well as the diverse headgroups available lead to an enormous diversity of lipid structures. Furthermore, the membrane composition vary between species, tissues, cells, membrane leaflets, and even membrane subdomains. Interestingly, changes in lipid composition have been reported in numerous diseases.[39] If the modification are specific to the disease, these changes can serve as biomarkers. Composition also changes dynamically. Indeed, the structure of a lipid bilayer is fluid and flexible. Lipid can, for example, migrate from one leaflet to the other. This rare process is called the flip-flop. Lipid molecules can, as well, more frequently, exchange places with their neighbours within a monolayer. Moreover, studies have shown that individual lipid molecules rotate very rapidly around their long axis and that their hydrocarbon chains are flexible.[37]
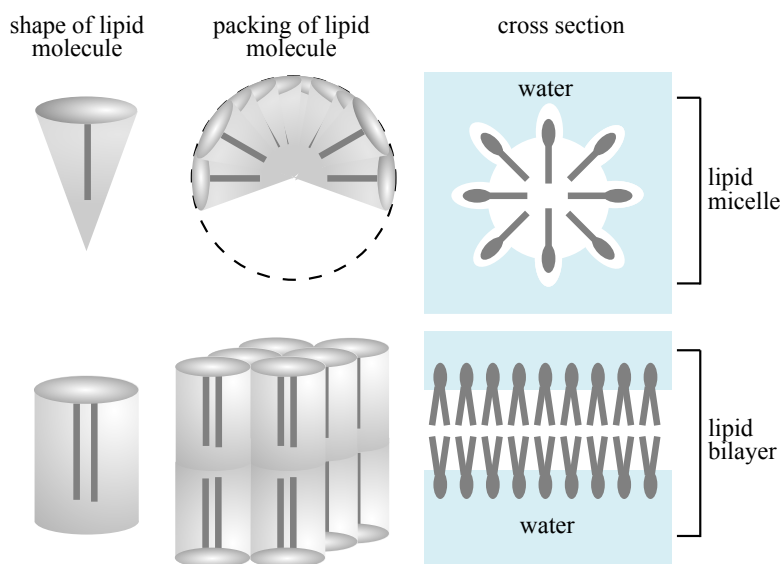
Figure 3.2 – Cone-shaped lipid molecules form micelles, whereas cylinder-shaped phospholipid molecules form bilayers. Inspiration from Ref[37]

Finally, lipid bilayers can exist in several states as a function of the temperature. In the gel state (L_β), all the hydrocarbon chains are in the all-trans conformation, the motional order is very high and the lateral diffusion is low. As the temperature increases, above a given temperature, the cellular membrane undergoes a phase transition to the liquid crystal state. In the liquid crystal state (L_α), motional order is lower than in the gel state and the lateral diffusion of lipids is much more rapid. The liquid crystal state is the predominant state of lipids in biological membranes.[40]

Chapter 4

Objectives

At the light of all the concepts presented in the previous Chapters, this Master thesis seeks a double objective: i) to assess structure-NLO property relationships in order to design SHIM dyes exhibiting large first hyperpolarizabilities and ii) to better understand the SHG responses of these compounds in biological imaging of lipid bilayers. This second objective encompasses the elaboration of a two-step simulation, to get the structure and then calculate the hyperpolarizability of chromophores in complex environments. This was done by the means of numerous theoretical methods judiciously selected and optimized. These are discussed in the second part of this manuscript. Chapter 5 focuses on Quantum Mechanics (QM) methods, whereas Chapter 6 presents elements of Molecular Mechanics (MM). Having presented and discussed all the necessary conceptual and theoretical background, the third part of this work is dedicated to the results presentation of the two research lines. The first study aims at establishing relationships between the structure of the chromophores and their NLO responses. It is presented in Chapter 7. This was done by considering a set of chromophores deriving from di-8-ANEPPS. Along the way, treatment of solvation effects was partially tackled. Chapter 8 deals with the second topic, and focuses on Molecular Dynamics modeling of di-8-ANEPPS in increasingly complex environments and analysis of its NLO responses. This was done using a two-step approach. These two axes are treated separately but have to be seen as complementary as they both focus on the same push-pull π-conjugated chromophore, di-8-ANEPPS.

Part II

Theoretical and computational methods

In this part, we introduce the major theoretical and computational methods that have been adopted in this Master thesis. The first Chapter focuses on the Quantum Mechanics methods, including the technique for geometry optimizations, the different approaches to determine the first hyperpolarizability, the computation of the excitation energies, and the description of the solvent effects. The second Chapter presents the Molecular Mechanics methods and their use in Molecular Dynamics. The choice of the parameters are discussed and the simulations set ups are described.

Chapter 5

Quantum Mechanics

5.1 Schrödinger equation

In quantum mechanics, at a given time, t, the state of a N-particle system is described by its wavefunction, $\Psi(\{\overrightarrow{r_i}\}, t)$, of which the square of the norm gives the probability density[41,42]:

$$\frac{d\mathcal{P}}{d\overrightarrow{r_i}} = |\Psi(\{\overrightarrow{r_i}\}, t)|^2 \tag{5.1}$$

with $\{\overrightarrow{r_i}\}$ the set of 3N spatial coordinates. It corresponds to probability density of finding the 1st particle in a volume $d\overrightarrow{r_1}$ around $\overrightarrow{r_1}$, the 2nd particle in a volume $d\overrightarrow{r_2}$ around $\overrightarrow{r_2}$, and so on. The time evolution of $\Psi(\{\overrightarrow{r_i}\}, t)$ is described by the time-dependent Schrödinger equation[41,42]:

$$\hat{H}(\{\overrightarrow{r_i}\}, t)\Psi(\{\overrightarrow{r_i}\}, t) = i\hbar\frac{\partial \Psi(\{\overrightarrow{r_i}\}, t)}{\partial t} \tag{5.2}$$

On the other hand, for stationary states, the time-independent Schrödinger equation is employed to determine $\Psi(\{\overrightarrow{r_i}\})$, as the eigenfunctions of the Hamiltonian, $\hat{H}$. $\hat{H}$ is the observable associated with the total energy of the system.

Now for a system of N electrons (indices i and j) and M nuclei (indice A), within the Born-Oppenheimer approximation, the electronic Hamiltonian reads[41,42]:

$$\hat{H} = \hat{T} + \hat{V} + \hat{U} \tag{5.3}$$

$$= -\frac{1}{2}\sum_{i=1}^{N}\nabla_i^2 - \sum_{i=1}^{N}\sum_{A=1}^{M}\frac{Z_A}{|\vec{r_i} - \vec{r_A}|} + \frac{1}{2}\sum_{i\neq j}^{N}\frac{1}{|\vec{r_i} - \vec{r_j}|} \tag{5.4}$$

$\hat{H}$ contains three types of terms : the kinetic energy operator, $\hat{T}$, the operator describing the electron-nucleus attraction, $\hat{V}$, and, finally, the electron-electron repulsion operator, $\hat{U}$. The Hamiltonian is therefore composed of one- and two-electron terms, the latter creating some bottleneck for solving Schrödinger equation. By considering only the one-electron terms, we can dissociate the N-electron problem into N one-electron problems. In such a case, Ψ can be written as a product of one-electron wavefunctions called orbitals $\phi_i(\vec{r_i})$, each corresponding to one electron of the system:

$$\Psi(\{\vec{r_i}\}) = \Psi(\vec{r_1}, \vec{r_2}, ..., \vec{r_N}) = \phi_1(\vec{r_1})\phi_2(\vec{r_2})...\phi_N(\vec{r_N}) = \prod_{i=1}^{N}\phi_i(\vec{r_i}) \tag{5.5}$$

and the total energy corresponds to the sum of the eigenvalues of these orbitals:

$$E = \sum_{i=1}^{N} E_i \tag{5.6}$$

These eigenvalues and eigenfunctions are solutions of the following equation:

$$\hat{H}(\vec{r_i})\Psi_n(\vec{r_i}) = E_n\Psi_n(\vec{r_i}) \tag{5.7}$$

This drastic approximation is however an important step towards finding the electronic wavefunction because it provides a first and simple expression. Then, according to Pauli's exclusion principle, the wavefunction should be anti-symmetric with respect to the permutation of the spin-space coordinates of any pair of particles. To satisfy this principle, Equation 5.5 is rewritten under the form of a Slater determinant[41,42]:

$$\Psi(\vec{x_1}, \vec{x_2}, ..., \vec{x_N}) = \frac{1}{\sqrt{N!}}\begin{vmatrix} \Theta_1(\vec{x_1}) & \Theta_2(\vec{x_1}) & \cdots & \Theta_N(\vec{x_1}) \\ \Theta_1(\vec{x_2}) & \Theta_2(\vec{x_2}) & \cdots & \Theta_N(\vec{x_2}) \\ \vdots & \vdots & \ddots & \vdots \\ \Theta_1(\vec{x_N}) & \Theta_2(\vec{x_N}) & \cdots & \Theta_N(\vec{x_N}) \end{vmatrix} \tag{5.8}$$

where, $\frac{1}{\sqrt{N!}}$ is the normalization constant. This determinant introduces the notion of spinorbital, $\Theta(\overrightarrow{x})$. Indeed, it was demonstrated that each electron possesses an intrinsic angular momentum, the spin. The electrons have either a spin α (up) or β (down). The notion of spatial orbital $\phi(\overrightarrow{r})$ (depending on spatial coordinates), is therefore completed by the spin function $\sigma(\omega)$ (depending on the variable ω), giving the spinorbital, $\Theta(\overrightarrow{x}) = \phi(\overrightarrow{r})\sigma(\omega)$. As a result of this improved representation of the wavefunction (Equation 5.8), any spatial orbital can, at most, be occupied by two electrons, of antiparallel spins. Finally, for systems with more than two electrons, Schrödinger equation must be solved approximately.

5.2 Hartree-Fock method

5.2.1 Time-independent version

The Hartree-Fock (HF) method[42] relies on the Slater determinant representation of the wavefunction and its optimization via the variational principle to solve the Schrödinger equation. It is the starting point for most quantum chemistry methods that describe many-electron systems more accurately. According to the variational principle, the best wavefunction is the one giving the lowest energy:

$$E_0 = \langle \Psi_0 | \hat{H} | \Psi_0 \rangle \tag{5.9}$$

Minimization of E_0 with respect to the spinorbitals proceeds by using the Lagrange multipliers method with the orthonormality constraint on the spinorbitals:

$$\langle \Theta_i | \Theta_j \rangle - \delta_{ij} = 0 \tag{5.10}$$

This leads to the HF equation :

$$\left\{ h(\overrightarrow{r_1}) + \sum_{j=1}^{N} [J_j(\overrightarrow{r_1}) - K_j(\overrightarrow{r_1})] \right\} \Theta_i(\overrightarrow{x_1}) = \epsilon_i \Theta_i(\overrightarrow{x_1}) \tag{5.11}$$

where the quantity between {}, $f(\overrightarrow{r_1})$, is the Fock operator. It is composed of the time-independent mono-electronic Hamiltonian, $h(\overrightarrow{r_1})$, the Coulomb, $J_j(\overrightarrow{r_1})$, and Exchange, $K_j(\overrightarrow{r_1})$, operators. The analysis of Equation 5.11 demonstrates that the Fock operator is also function of its eigenfunctions.

Indeed, the Coulomb and Exchange operators are function of the spinorbitals. Solving the HF equation must therefore be done via an iterative procedure, until self-consistency. It is therefore known as the Self-Consistent Field (SCF) method.

Within the Linear Combination of Atomic Orbitals (LCAO) approximation, the molecular orbitals are developed under the form of linear combinations of atomic orbitals, χ_q, using the following Equation:

$$\phi_i(\vec{r}) = \sum_{q=1}^{K} C_{qi}\chi_q(\vec{r}) \tag{5.12}$$

where, the C_{qi} are the LCAO coefficients and K is the size of the atomic orbital basis set. Several matrices are then defined, starting with the overlap matrix, S_{pq} :

$$S_{pq} = \int \chi_p^*(\vec{r})\chi_q(\vec{r})d\vec{r} \tag{5.13}$$

then, the Fock matrix, F_{pq}:

$$F_{pq} = \int \chi_p^*(\vec{r})f(\vec{r})\chi_q(\vec{r})d\vec{r} \tag{5.14}$$

and, finally, the density matrix, D_{sr}:

$$D_{sr} = \sum_{j}^{N/2} C_{sj}C_{rj}^* \tag{5.15}$$

The latter allows us to give a new expression for the Fock matrix elements:

$$F_{pq} = H_{pq} + \sum_{r=1}^{K}\sum_{s=1}^{K} D_{sr}[2(pq|rs) - (ps|rq)] \tag{5.16}$$

Finally, by introducing the LCAO expression into the HF equation and by using the definition of S_{pq}, F_{pq}, and D_{sr}, Equation 5.11 may be rewritten:

$$\sum_{q=1}^{K} F_{pq}C_{qi} = \epsilon_i \sum_{q=1}^{K} S_{pq}C_{qi} \tag{5.17}$$

which can be compacted under the form of a matrix equation:

$$FC = SCE \tag{5.18}$$

The solution to this equation is the C matrix (LCAO coefficients), where each column defines one molecular orbital. Since the Fock matrix depends on the density matrix, the HF equation is solved iteratively, as shown in Figure 5.1. After choosing an atomic basis set (see below), it starts with a preliminary guess of the density matrix, which is put into the Fock matrix. The generalized eigenvalues problem $FC = SCE$ is converted into a traditional eigenvalues problem $F'C' = C'E$ and the F' matrix is diagonalized to obtain C' and E. Then, the LCAO coefficient matrix is evaluated from the C' matrix. Finally, the density matrix is calculated and put back into the Fock matrix. This iterative procedure is pursued until convergence.

$$F_{pq} = H_{pq} + \sum_{r=1}^{K} \sum_{s=1}^{K} D_{sr}[2(pq|rs) - (ps|rq)]$$

$$D_{sr} = \sum_{j}^{N/2} C_{sj} C_{rj}^{*}$$

$$F' = S^{-1/2} F S^{-1/2}$$

$$C = S^{-1/2} C'$$

$$F'C' = C'E$$
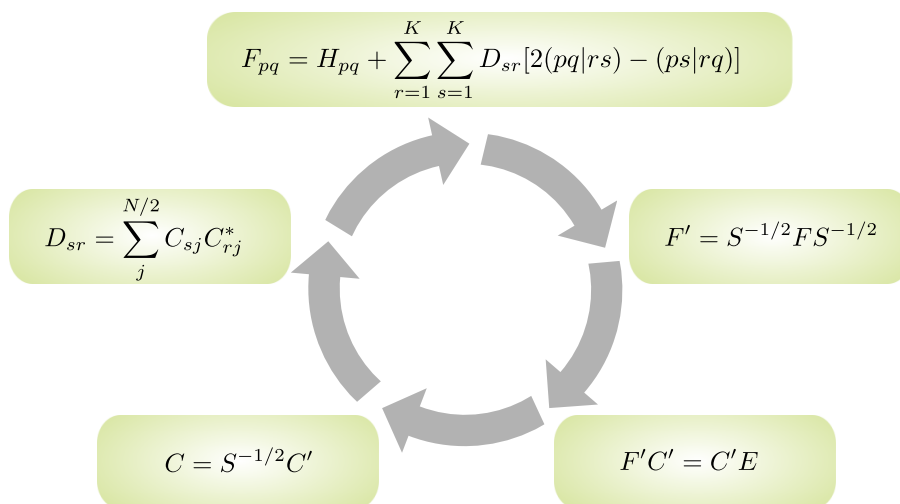
Figure 5.1 – The Self-Consistent-Field (SCF) method.

The HF method has an important limitation: the correlation default. Indeed, it neglects or approximates some of the interactions between electrons. Therefore, this method gives systematically a higher energy than the one of the exact ground state of a system. The difference between the exact energy and the HF limit is called the correlation energy.[43]

Atomic basis sets

The choice of an atomic basis set is an important element, which precedes all SCF computation. These atomic orbitals have to describe the molecular orbitals and so the wavefunction of the system and the associated density.[42] The presentation focuses on some of the basis sets used, later, in Section 7.2.

The basis functions are composed of contraction of Gaussians. For example, the minimal basis sets (or simple-ζ), developed by Pople and his group, includes one basis function for every atomic

orbital required to describe the free atom in its ground state. For example, for the Slater Type Orbital (STO-3G), each basis function is composed of a contraction of three Gaussians, for which the contraction coefficients and exponents are evaluated beforehand. Along the same lines, the double-ζ and triple-ζ basis sets include, respectively, two and three basis functions for each atomic orbital occupied.

Subsequently, Pople developed the Split-Valence basis sets. They include one function for the core orbitals and several functions for those in the valence shell. For example, the double-ζ basis set 6-31G includes one contraction of six Gaussians for the core orbitals and two functions for the valence part, one contraction of three Gaussians and the second of one Gaussian.

Polarization functions, symbolized by a "*", can be added to better describe the distortion of the atom densities when bonds are formed. They consist of a set of Gaussian functions one unit higher in angular momentum than the ones present in the ground state of the atom. For example, to the 6-31G basis set, we can add a set of d functions on all non-hydrogen atoms, giving the 6-31G* basis set. To the latter, we can further add a set of p functions on the hydrogen atoms to obtain the 6-31G** basis set. In general, adding polarization functions improves the description of molecular geometries as well as of relative energies.

In order to improve the description of the external part of the orbitals and the electronic density, basis functions with small exponents are added. These are called diffuse functions and are symbolized using "+". For example, the 6-31+G* contains one set of s diffuse functions on the hydrogen atoms and one set of s and p diffuse functions on the non-hydrogen atoms.

Dunning developed the correlation-consistent polarized valence (cc-PVXZ, where X = D, T, Q, 5,... for double, triple, quadruple) basis sets. They are particularly appropriate for the description of electron correlation. In this work, we consider the cc-pVDZ and cc-pVTZ basis sets. Furthermore, Dunning's augmented (or doubly-augmented) basis sets include additional diffuse functions, giving the aug-cc-pVDZ (or the d-aug-cc-pVDZ) basis sets. [42,44–47]

5.2.2   Time-dependent version

In this time-dependent version, the HF equation (Equation 5.18) is replaced by an analogue version, the time-dependent Hartree-Fock (TDHF) equation:

$$FC - i\left(\frac{\partial SC}{\partial t}\right) = SC\varepsilon \tag{5.19}$$

where ε represents the Lagrangian multiplier. Then, similarly as before, the variational principle is used under the orthonormality constraint between the spinorbitals:

$$C^{\dagger}SC = 1 \tag{5.20}$$

Finally, the third reference equation concerns the definition of the density matrix:

$$D = CnC^{\dagger} \tag{5.21}$$

where n is the diagonal matrix of occupation numbers (equal to 1 for occupied orbitals and to 0 for unoccupied orbitals).[48] The TDHF equation allows describing the responses of a system to external time-dependent perturbations. For instance, an external electric field applied in direction ζ and oscillating at pulsation ω:

$$X^{\zeta}(\omega) = E_{\zeta}\, e^{i\omega t} \tag{5.22}$$

We start by rewriting the elements of the 1st-order perturbed LCAO matrix, considering not one but two perturbations, at pulsations ω and $-\omega$, which are complex-conjugate of each other:

$$C^{\zeta}(\omega) = CU^{\zeta}(\omega) \tag{5.23}$$

$$C^{\zeta}(-\omega) = -CU^{\zeta}(\omega) \tag{5.24}$$

The ζ exponent states for a first-order derivative with respect to E_g. Accordingly from the first-order orthonormalization equation:

$$C^{\zeta\dagger}(-\omega)SC + C^{\dagger}SC^{\zeta}(\omega) = 0 \tag{5.25}$$

we obtain

$$U^{\zeta\dagger}(-\omega) + U^{\zeta}(\omega) = 0 \tag{5.26}$$

Because of the form of the density matrix (Equation 5.27), we need both $U^{\zeta\dagger}(-\omega)$ and $U^{\zeta}(\omega)$. This problem is simplified by the use of the orthonormalization equations. Once $U^{\zeta}(\omega)$ has been

computed, $C^\zeta(\omega)$ can computed via Equation 5.23 while $C^\zeta(-\omega)$ can be computed using Equation 5.24.[48]

$$D^\zeta(\omega) = C^\zeta(\omega)nC^\dagger + CnC^{\zeta\dagger}(-\omega) \tag{5.27}$$

Note that the first-order transformation matrices $U^\zeta(\pm\omega)$ are block off-diagonal with zero in the diagonal blocks and that $D^\zeta(\omega)$ depends only on these off-diagonal (occ-unocc and unocc-occ) elements :

$$D^\zeta_{rs}(\omega) = \sum_{i=1}^{occ}\sum_{a=1}^{unocc} C_{ra}U^\zeta_{ai}(\omega)C^\dagger_{is} + C_{ri}U^{\zeta\dagger}_{ia}(-\omega)C^\dagger_{as} \tag{5.28}$$

Once again, the D^ζ matrix elements are evaluated using an iterative procedure, as shown in Figure 5.2. This requires calculating the elements of U^ζ:

$$U^\zeta_{ia}(\omega) = \frac{G^\zeta_{ia}(\omega)}{\epsilon_a - \epsilon_i - \omega} \tag{5.29}$$

Beforehand, the G^ζ elements should be calculated:

$$G^\zeta = C^\dagger F^\zeta C \tag{5.30}$$

$$F^\zeta_{pq}(\omega) = M^\zeta_{pq} + \sum_{r,s}^{K} D^\zeta_{sr}(\omega)[2(pq|rs) - (ps|rq)]$$

$$D^\zeta_{rs}(\omega) = \sum_{i=1}^{occ}\sum_{a=1}^{unocc} C_{ra}U^\zeta_{ai}(\omega)C^\dagger_{is} + C_{ri}U^{\zeta\dagger}_{ia}(-\omega)C^\dagger_{as}$$

$$G^\zeta(\pm\omega) = C^\dagger F^\zeta(\pm\omega)C$$

$$C^\zeta(\omega) = CU^\zeta(\omega)$$
$$C^\zeta(-\omega) = -CU^{\zeta\dagger}(\omega)$$

$$U^\zeta_{ia}(\pm\omega) = \frac{G^\zeta_{ia}(\pm\omega)}{\epsilon_a - \epsilon_i \mp \omega}$$
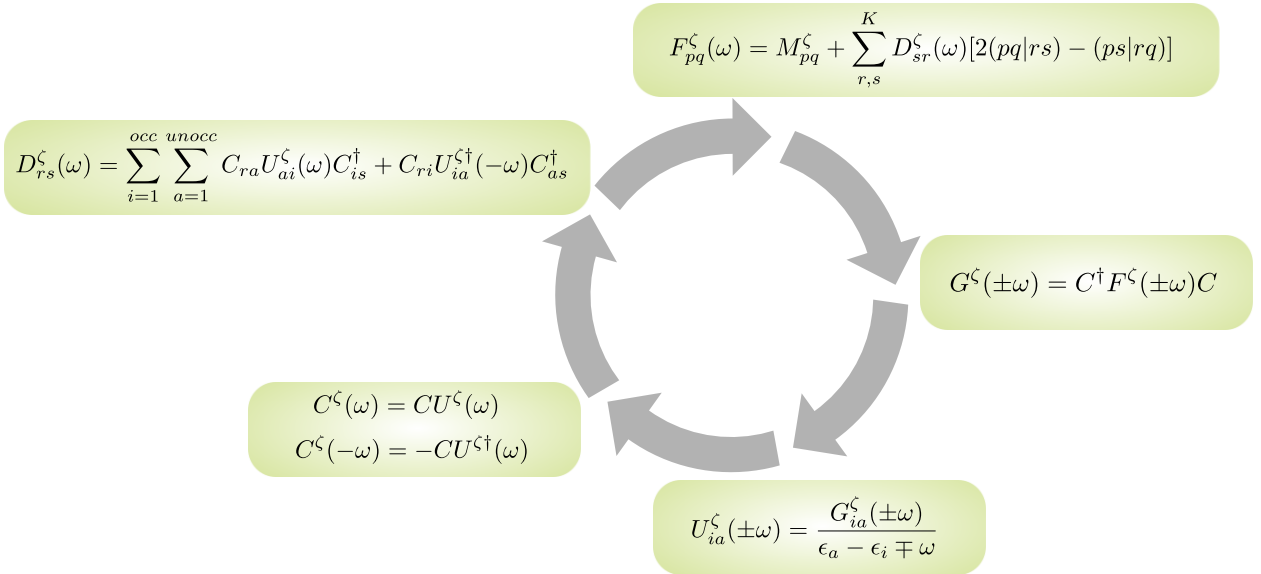
Figure 5.2 – THDF cycle for dynamic electric field perturbation

5.2.3   First hyperpolarizability

The TDHF formalism can be used to treat the interaction of a molecule with light. Within this approach, the evaluation of the first hyperpolarizability, β, involves the determination of the second-order derivatives of the density matrix, D, with respect to the dynamic external electric field, as mentionned in Equation 5.31. However, it is possible to get the first hyperpolarizability directly from the first-order derivative of the LCAO coefficients (Equation 5.23 and 5.24) by taking advantage of the "$2n + 1$" rule. The latter states that the knowledge of the wavefunction through order n allows the knowledge of the energy through order $(2n + 1)$.

$$\beta_{\zeta\eta\chi}(-2\omega; \omega, \omega) = 2 \sum_{pq}^{K} M_{p,q}^{\zeta} D_{qp}^{\eta\chi}(\omega, \omega) \tag{5.31}$$

5.3   Density functional theory

5.3.1   Time-independent version

The density functional theory (DFT)[49,50] is a method that provides the ground state properties of large systems within reasonable computational costs (i.e. similar computational cost as the Hartree-Fock method but it introduces electron correlation, whereas the cost of other correlated methods increases considerably with the size of the system).

The principle of DFT is based on the Hohenberg and Kohn (H-K) theorems which state that the ground state electronic energy is determined completely by the electron density, $\rho(\overrightarrow{r})$.[51] So, the complete wavefunction, $\Psi(\overrightarrow{x_1}, \overrightarrow{x_2}, ..., \overrightarrow{x_N})$, and the associated Schrödinger equation are replaced by the much simpler electron density, $\rho(\overrightarrow{r})$, and its associated calculation schemes.

The first H-K theorem affirms that the external potential $v_{ext}(\overrightarrow{r})$ is determined, within a trivial additive constant, by $\rho(\overrightarrow{r})$. Since $\rho(\overrightarrow{r})$ gives the number of electrons, N, by integration, it therefore determines the kinetic energy operator, $\hat{T}$, as well as the electron-electron repulsion operator, $\hat{U}$. Finally, the full Hamiltonian (Equation 5.4) is, according to this theorem, completely defined, as well as all properties determined by $\hat{H}$.

Owing to this first H-K theorem, the energy is a functional of the electron density and is written:

$$E_v[\rho(\overrightarrow{r})] = T[\rho(\overrightarrow{r})] + V[\rho(\overrightarrow{r})] + U[\rho(\overrightarrow{r})] \tag{5.32}$$

where T is the kinetic energy functional, V is the nuclei-electron (external) potential energy, and U is the electron-electron repulsion energy. These can be regrouped into two terms depending on the external potential and a new quantity, the Hohenberg-Kohn functional, F_{HK}:

$$E_v[\rho(\overrightarrow{r})] = \int \rho(\overrightarrow{r})v(\overrightarrow{r})d\overrightarrow{r} + F_{HK}[\rho(\overrightarrow{r})] \tag{5.33}$$

where F_{HK} is expressed as:

$$F_{HK}[\rho(\overrightarrow{r})] = T[\rho(\overrightarrow{r})] + J[\rho(\overrightarrow{r})] + \text{non-classical term} \tag{5.34}$$

where U has been decomposed into a Coulombian "classical" term, J, and the remaining non-classical terms. The 2nd H-K theorem states that $E_v[\rho(\overrightarrow{r})]$ delivers the lowest energy, if the input density is the true ground state density $\rho_0(\overrightarrow{r})$, by using the variational principle.[51] If F_{HK} was known exactly, the Schrödinger equation could be solved exactly. However, the non-classical term, called the exchange-correlation, is not known.

Within the Kohn-Sham (KS) approach, one considers a set of fictitious non-interacting "particles", defined to reproduce the exact density, $\rho(\overrightarrow{r})$, of the interacting electrons. Then, following equation 5.35 one-electron wavefunctions are reintroduced under the form of Kohn-Sham (spin)orbitals, Θ_i.[49] They satisfy the relation:

$$\rho(\overrightarrow{r}) = \sum_{i=1}^{N} \int d\omega |\Theta_i(\overrightarrow{r}, \omega)|^2 \tag{5.35}$$

The full Hamiltonian for this non-interacting electron system (Equation 5.36) does not include explicit electron-electron repulsion and it can be written as the sum of one-electron terms. The first being the kinetic energy term and the second, the effective potential $v_{eff}(\overrightarrow{r})$ (i.e. the Kohn-Sham effective potential in which the non-interacting electrons move).

$$\hat{H} = -\frac{1}{2} \sum_{i=1}^{N} \nabla_i^2 + \sum_{i=1}^{N} v_{eff}(\vec{r_i}) \tag{5.36}$$

Within the KS approach, $F_{HK}[\rho]$ or $F[\rho]$ becomes:

$$F[\rho] = T_s[\rho] + J[\rho] + E_{xc}[\rho] \tag{5.37}$$

Finally, similarly to HF, the canonical form of the Kohn-Sham equation (Equation 5.38) is obtained using the variational principle under the same orthogonality constraint:

$$\left[-\frac{1}{2}\nabla^2 + v_{eff}(\vec{r}) \right] \Theta_n(\vec{x}) = \epsilon_n \Theta_n(\vec{x}) \tag{5.38}$$

Since $v_{eff}(\vec{r})$ depends on $\rho(\vec{r})$, this equation must be solved self-consistently, as shown in Figure 5.3.
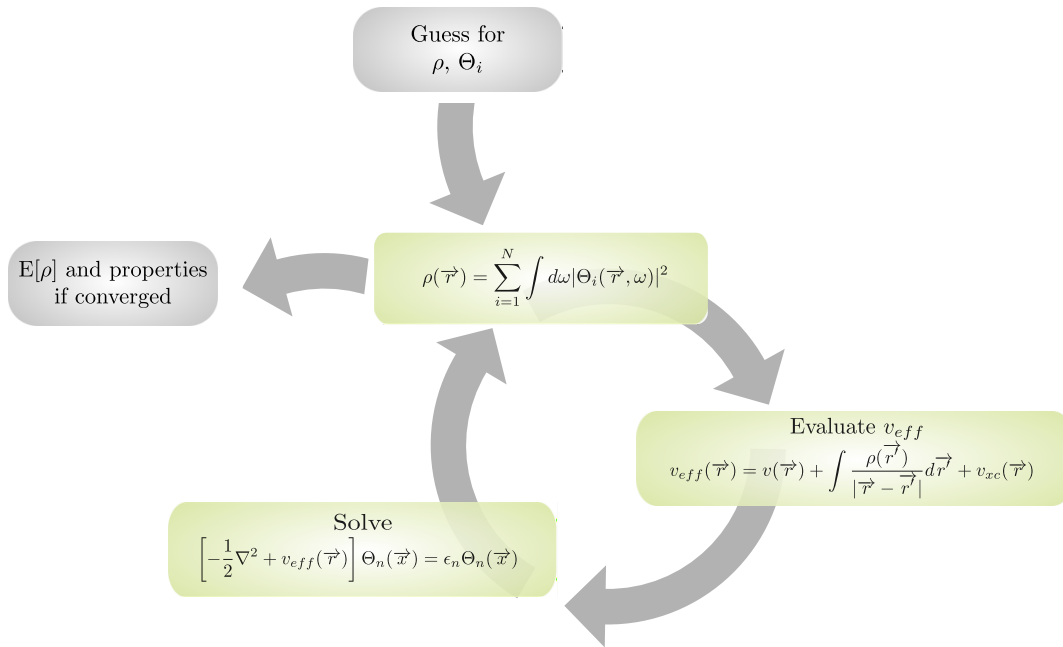
Figure 5.3 – Kohn Sham SCF cycle.

KS theory is exact in principle, via the introduction of the exact exchange-correlation (XC) functional.[52] However, since the latter is not known, it has to be approximated. Different types of XC functionals were developped over the years, increasing more and more the accuracy of the exchange correlation energy. Indeed, the accuracy of the Kohn-Sham method depends on the validity of this approximated functional.[53] However, there is no straightforward way in which the

XC functional can be systematically improved.[54,55] Moreover, the higher levels are typically more computationally demanding than the lower ones.[56] As shown Figure 5.4, the hierarchy of XC approximations form a ladder, called Jacob's ladder.[56] Each rung incorporates the key elements of the lower rungs, and more.

The local density approximation (LDA) functionals were the first functionals created. They assume that the XC energy of a non-uniform system can be obtained by applying an uniform gas of electron for infenitesimal portions of the non-uniform electron distribution. However, it has been proven that LDA is no better than HF and so there is no point in doing it on its own.[53]

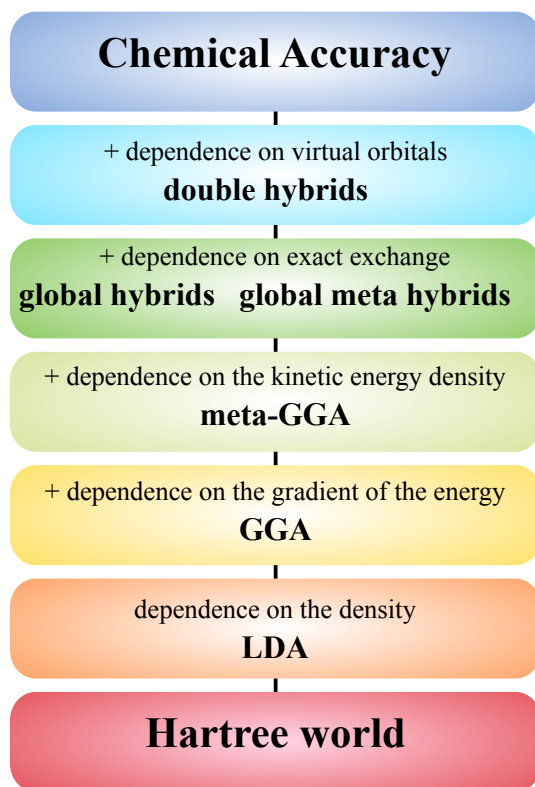With the generalized gradient approximation (GGA), a dependence on the gradient of the density is added. Then, for the meta-GGAs, an explicit dependence on the kinetic energy density is introduced. The hybrid functionals include a percentage of exact Hartree-Fock exchange (EXX). This exact exchange is needed to describe situations in which the exact XC hole has a long-range component that cannot be replicated by local or semi local approximation such as LDA, GGA, or even meta-GGA.[53,57]

More rungs were added to the ladder with the double hybrids, which include a perturbative second-order Møller-Plesset correlation part (MP2) in addition to a percentage of HF exchange[58] as well as with dispersion-including functionals that replace part of the non-local, long- and medium-range electron correlation effects in conventional GGA (and higher) by empirical dispersion corrections.[59]

The challenge is to find the appropriate XC functionals to yield accurate results. Still, this depends on the type of molecular system as well as on the property of interest.[60]

5.3.2   Geometry optimization

In this work, DFT was applied to perform the geometry optimization of all the molecular structures considered. Indeed, it is well established that the density functional formalism is a powerful tool in predicting ground-state properties of many-electron systems. The M06-2X XC functional was used in this study considering that it exhibits an excellent all around performance.[52] Futhermore, previous works demonstrated its efficiency for obtaining the geometry of ANEP-like structure, in particular, its dihedral angles. M06-2X is a global meta-hybrid functional that contains 54% of HF exchange.[61] A structure optimization proceeds self-consistently. At each iteration, the algorithm computes four quantities that are used as criteria to monitor the optimisation: i)

Chemical Accuracy

+ dependence on virtual orbitals
double hybrids

+ dependence on exact exchange
global hybrids   global meta hybrids

+ dependence on the kinetic energy density
meta-GGA

+ dependence on the gradient of the energy
GGA

dependence on the density
LDA

Hartree world

Figure 5.4 – Jacob's ladder of XC functionals.[56]

the maximum remaining forces acting on the atoms, ii) the root mean square (RMS) forces on all atoms, iii) the maximum, and iv) RMS displacements (i.e. the maximum structural changes between the last two steps). The algorithm then modifies the molecular structure towards the next local minimum on the potential energy surface. Once these four values fall under the convergence thresholds, fixed beforehand, the optimization is complete.

5.3.3   Time-dependent version

At the DFT level, the responses to a dynamic external electric field are evaluated using the time-dependent density functional theory (TDDFT) method.[62,63] Similarly to the time-independent case, it has been demonstrated that there is a one-to-one correspondence between the time-dependent density, $\rho(\overrightarrow{r}, t)$, and the time-dependent external potential, $v(\overrightarrow{r}, t)$. As a consequence, the time-dependent wavefunction is completely defined by the density. Again, within the KS approach, we consider a set of non-interacting electrons, having the exact density of the real system :

$$\rho(\vec{r}, t) = \sum_{i=1}^{N} \int d\omega |\Theta_i(\vec{r}, \omega, t)|^2 \tag{5.39}$$

Similarly, we obtain the time-dependent Kohn-Sham equation (Equation 5.40), which is solved self-consistently, within the adiabatic approximation. Equation 5.40 is the equivalent to the canonical form of the TDHF equation (Equation 5.11).

$$\left[-\frac{1}{2}\nabla^2 + v_{eff}(\vec{r}, t)\right]\Theta_n(\vec{x}, t) = i\frac{\partial}{\partial t}\Theta_n(\vec{x}, t) \tag{5.40}$$

with

$$v_{eff}(\vec{r}, t) = v(\vec{r}, t) + \int \frac{\rho(\vec{r}', t)}{|\vec{r} - \vec{r}'|}d\vec{r}' + v_{xc}(\vec{r}, t) \tag{5.41}$$

For a system in the ground state, corresponding to $v^0(\vec{r})$, at t_0, the potential is perturbed by a time-dependent perturbation, so that it becomes itself time-dependent:

$$v(\vec{r}, t) = v^0(\vec{r}) + \lambda v^1(\vec{r}, t) \tag{5.42}$$

The system responds to this perturbation so that the electron density becomes in turn time-dependent:

$$\rho(\vec{r}, t) = \rho^0(\vec{r}) + \lambda\rho^1(\vec{r}, t) + \lambda^2\rho^2(\vec{r}, t) + ... \tag{5.43}$$

The first-order density matrix in the frequency domain is given by:

$$\rho^1(\vec{r}, \omega) = \int \chi_{eff}(\vec{r}, \vec{r}', \omega)v^1_{eff}(\vec{r}', \omega)d\vec{r}' \tag{5.44}$$

where $\chi_{eff}(\vec{r}, \vec{r}', \omega)$ is the linear response kernel and $v^1_{eff}(\vec{r}', \omega)$ is the first-order perturbed effective potential:

$$v^1_{eff}(\vec{r}', \omega) = v^1(\vec{r}', \omega) + \int \left[\frac{1}{|\vec{r} - \vec{r}'|} + f^{adia}_{xc}(\vec{r}, \vec{r}', \omega = 0)\right]\rho^1(\vec{r}', t)d\vec{r}' \tag{5.45}$$

where f^{adia}_{xc} is the adiabatic XC kernel. As can be seen from the form of Equations 5.44 and 5.45, these equations are interdependent and must be solved iterativelly. This leads for instance to a

SCF cycle analogous to the one presented in Figure 5.2 when the target consists in calculating the response to external electric fields (see also Subsection 5.3.4).

5.3.4 First hyperpolarizability

Similarly to the TDHF case, the first hyperpolarizability are obtained by taking advantage of the "$2n + 1$" theorem. In the present case, it means that β, corresponding to the third-order derivative of the energy, $\mathbf{E}$ with respect to the electric field, can be obtained from the knowledge of first-order quantities.

$$\beta(E) = -\left(\frac{\partial^3 \mathbf{E}(E)}{\partial E^3}\right)_{E=0} \tag{5.46}$$

There are many analogies to the calculation of frequency-dependent hyperpolarizabilities between the TDHF and TDDFT approaches. The major difference is that, within the TDDFT approach, the correlation effects are taken into account via the f_{xc}^{adia} term of Equation 5.45. The latter being usually very important to evaluate the first hyperpolarizability.

5.3.5 Excitation energy

One of the most popular application of the TDDFT is the extraction of the electronic excited-state properties, after the ground state of a molecule has been found.[63] It exploits the fact that the linear response, $\rho^1(\overrightarrow{r}, t)$, to the external perturbation, ω, presents poles at the exact vertical excitation energies of the system.[64] By combining the two-interdependent Equations 5.44 and 5.45, we obtain this generalized eigenvalue problem[65]:

$$\begin{pmatrix} A & B \\ B^* & A^* \end{pmatrix} \begin{pmatrix} X \\ Y \end{pmatrix} = \omega \begin{pmatrix} 1 & 0 \\ 0 & -1 \end{pmatrix} \begin{pmatrix} X \\ Y \end{pmatrix} \tag{5.47}$$

where the form of the matrices A and B are given in Refs[66,67] and the matrices X and Y are associated with excitations and de-excitations. Within the Tamm-Dancoff Approximation (TDA), B is set to zero, and Equation 5.47 simplifies as:

$$AX = \omega X \tag{5.48}$$

Equations 5.47 and 5.48 allow us to obtain the excitation energies as well and the oscillator

strengths.[63] In this work, the excitations energy were calculated not only to characterize the low-energy absorption spectra of the chromophore but also to analyze their first hyperpolarizabilities within the two-state approximation, of which the principles and results are presented in Section 7.5. Once again, the M06-2X XC functional was used, as the performance of the M06 family to obtain excitation energies was demonstrated.[68] Furthermore, it was previously employed to get the wavefunction.

5.4   Polarizable Continuum Model and implicit solvation

Most systems are not in gas phase, but in solution (or in more complex environments) and the challenge is to describe accurately the solute-solvent interactions. Indeed, the latter modify the equilibrium structures and change the response of the molecule to external perturbations. When simulating solvated systems, the choice of solvent approximation is therefore an important issue. There are two main approaches to simulating solvents: explicitly or implicitly. With an explicit solvation model, the solvent molecules (i.e. the coordinates) are included in the input file. In implicit models, the solute-solvent interactions are replaced by a reaction electric field representing the statistical average over all solvent degrees of freedom. This reduces the computational cost but they pay a penalty in accuracy. The solute-solvent hydrogen bonds are not reproduced, for example.

In this study, solvent effects were partially described by using the Integral Equation Formalism of the Polarizable Continuum Model (IEFPCM).[69–71] This implicit solvation scheme approximates the solvent as a structureless polarizable continuum whose interactions with the solute are mediated by its dielectric permittivity, ϵ. The solute is in a cavity built by interlocking van der Waals spheres centered at the atomic positions, as shown at Figure 5.5. There might be inaccessible zones to the solvent, so that the Solvent Excluding Surface (SES) or Solvent Accessible Surface (SAS) can be defined. The SES is delimited by rotating a spherical probe around the cavity to smooth its contour. Within the SAS approach, the radius of the solvent is added around the cavity.

After proper definition of the cavity, the solute-solvent interactions are modeled by introducing a surface charge distribution on the cavity surface, giving rise to an apparent surface charge (ASC), $\sigma(\vec{r})$. The charge distribution of the solute inside the cavity, $\rho(\vec{r})$, polarizes the dieletric continuum, which in return polarizes the solute charge distribution. This electrostatic problem can
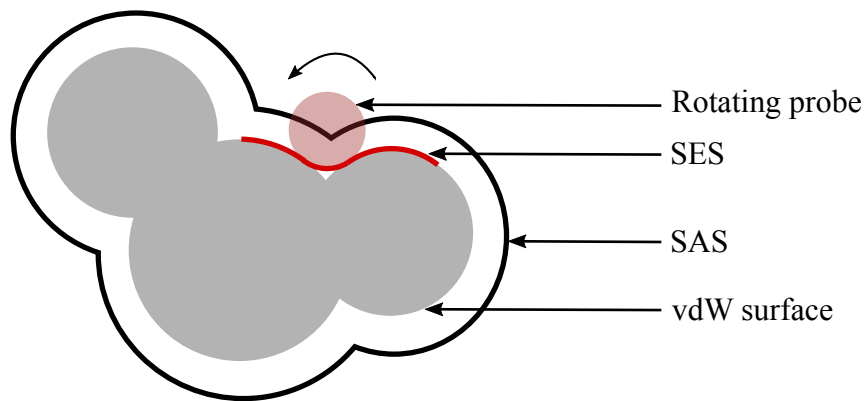
Figure 5.5 – Definitions of the PCM cavity.

be solved in terms of a potential, $V(\overrightarrow{r})$ (Equation 5.49), that contains two terms, one depending on the charge distribution of the solute, $\rho(\overrightarrow{r})$, and the other relative to the apparent surface charge $\sigma(\overrightarrow{r})$ associated to the solvent.[70,71]

$$V(\overrightarrow{r}) = V_\rho(\overrightarrow{r}) + V_\sigma(\overrightarrow{r}) \tag{5.49}$$

Finally, the solute-solvent interactions are taken into account by including this potential contribution to the Hamiltonian of the isolated molecule to form an effective solute Hamiltonian :

$$\hat{H}_{eff} = \hat{H}_{solute} + V_{SCRF} \tag{5.50}$$

with:

$$V_{SCRF} = \int V(\overrightarrow{r})\rho(\overrightarrow{r})d\overrightarrow{r} \tag{5.51}$$

Evaluating the solute-solvent interactions is therefore done self-consistently via an iterative procedure. In each SCF cycle, there is a second iterative procedure dedicated to evaluate $V_\sigma(\overrightarrow{r})$ and $\sigma(\overrightarrow{r})$.

Chapter 6

Molecular Mechanics

6.1 Theoretical background

Molecular Mechanics[72] (MM) is a computational method that allows us to compute the potential energy surface of a system, and find its minimum. It is a "ball-and-spring" model, meaning that each spring represents a classical interaction (i.e. no electrons present) between two or more atoms. The potential energy is described by a set of energy functions gathered in the so-called force field (FF). All common FFs subdivide potential energy functions into two classes, bonded [bond-stretching (Equation 6.1), angle-bending (Equation 6.2), torsional angle motions (Equation 6.3), and out-of-plane "improper torsion" potentials (Equation 6.4)], and nonbonded interactions [Lennard-Jones repulsions and dispersions (Equation 6.5), hydrogen-bonding as well as Coulomb forces (Equation 6.6)].[73]

$$V(r) = \sum_{bonds} K_r (r - r_{eq})^2 \qquad (6.1)$$

$$V(\psi) = \sum_{impropers} K_\psi (\psi - \psi_{eq})^2 \qquad (6.4)$$

$$V(\theta) = \sum_{angles} K_\theta (\theta - \theta_{eq})^2 \qquad (6.2)$$

$$V = \sum_{i<j} 4\epsilon_{ij} \left[\left(\frac{\sigma_{ij}}{r_{ij}} \right)^{12} - \left(\frac{\sigma_{ij}}{r_{ij}} \right)^6 \right] \qquad (6.5)$$

$$V(\phi) = \sum_{dihedrals} K_\phi (1 - cos(n\phi)) \qquad (6.3)$$

$$V = \sum_{i<j} \frac{q_i q_j}{4\pi\epsilon_0 r_{ij}} \qquad (6.6)$$

6.2   Molecular Dynamics

Molecular Dynamics (MD)[74,75] is a very powerful toolbox in modern molecular modelling that was first developed in the late 70s. It generally uses MM potential energy functions to generate configurations of a system and enables to follow and understand its structure and dynamics with extreme details. It gives access to the kinetic properties of the system. Actually, this method consists of the numerical, step-by-step, solution of the classical Newton's equations of motion,[73] which may be written :

$$m_i \overrightarrow{\ddot{r_i}} = \overrightarrow{F_i} = -\overrightarrow{\nabla} V_i \tag{6.7}$$

with m_i the mass of the ith atom, $\overrightarrow{\ddot{r_i}}$ the acceleration, and $\overrightarrow{F_i}$ the force. V is the potential energy of the system that is calculated using FF. The latter calculates the forces acting on the atoms and subsequently the coordinates and the velocities are updated at each step of the MD simulation (Figure 6.1). The results consist in a series of snapshots taken at close time intervals.
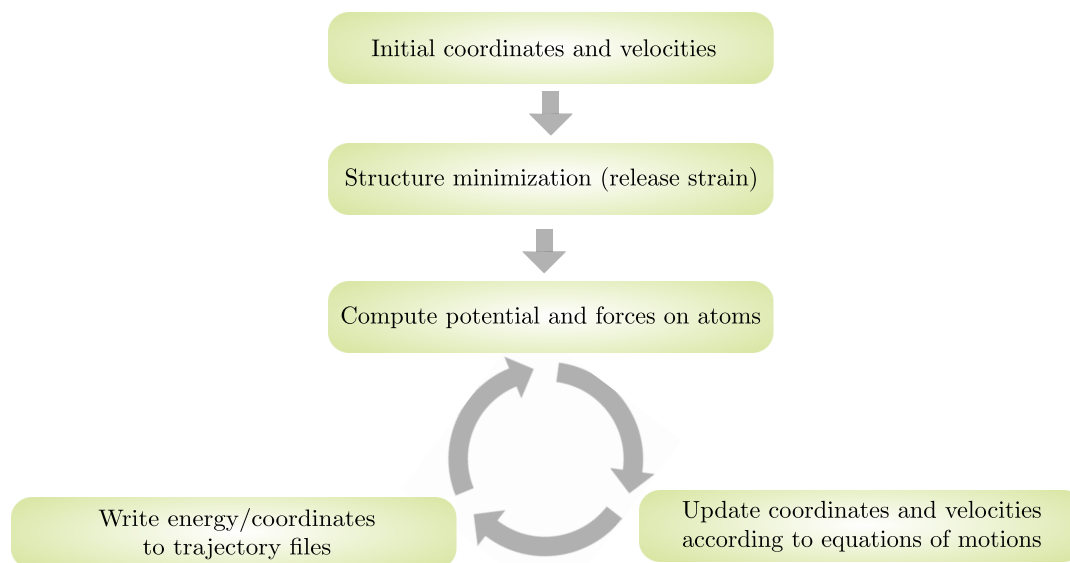
Figure 6.1 – MD flowchart.

A MD simulation is divided into several parts: minimization, equilibration, and production. After the simulation has been set up, usually a brief minimization is performed for two reasons. First, when a starting configuration is very far from equilibrium, large forces can cause the simulation to crash or distort the system. Secondly, clashes between atoms are removed. The goal of this minimization step is not to reach any global equilibrium. Then, an equilibration run is conducted

during which the system is left to equilibrate. The simulation switches to the production run when the energy (or another property) of the system has converged. During this last step, data are collected and properties can be calculated and analyzed.

6.2.1 Discussion of the parameters

In order to set up a simulation, several parameters have to be fixed. Information about the initial size of the periodic cell, the time of the simulation, the statistical ensemble, the time step, the number of molecules included in the simulation, and so on, are needed. All these choices can impact considerably the feasibility and validity of the computations. The force fields chosen for the studied molecules are also crucial. The choice and validation of the force fields used in this study are discussed later, in Chapter 8.

Periodic boundary conditions (PBC)

A periodic cell is often used to avoid surface effects at the boundary of the simulated system. The cell is thus surrounded with copies of itself to infinity by translation in all three Cartesian directions. When a particle leaves or enters the simulation box on one side, an image particle enters or leaves the box on the opposite side. The number of particles is always constant and each particle is subject to the potential from all other particles in the system including in the surrounding cells. Because every cell is an identical copy of all the others, all image particles move solidary together and only one of them is actually simulated.[75]

Statistical ensemble

A choice has also to be made concerning the statistical ensemble in which will occur the MD simulation. Different statistical ensembles can be used depending on the purpose of the work. Among the microcanonical ensemble (NVE), the canonical ensemble (NVT), the grand-canonical ensemble (μVT, with μ the chemical potential), and the isothermic-isobaric ensemble (NPT), most molecular dynamics studies on biological systems use either the NPT or the NVT ensemble. The NPT ensemble fixes the number particles (N), the pressure (P), and the temperature (T). Not fixing V, allows the system to adjust the box size so that the internal virial matches the externally applied pressure.[76–78] The advantage of this method is that only an approximation of the initial size is needed.[79]

Time step

The time step or the interval over which the forces are considered constant, and which determines how often configurations change, is an important consideration. The choice of the time step to accurately describe the dynamics of a system is governed by the fastest degree of freedom, which in most cases, are the intramolecular bond vibrations. If the time steps are unecessary too small, computer time and disk space are wasted. If the time steps are too large, the simulation is no longer energy conserving and accuracy will suffer. Difficulties arise when very fast and very slow motions are present simultaneously, since a time step small enough to describe the fast motions will require unreasonably long computations to describe the slow motions.[80]

Nonbonded interactions

Computing exactly the nonbonded interactions (which occur between every pairs of atoms) is unfeasible because too long and expensive. To reduce the cost of this computation, a common approach is to ignore any interaction between atom separated by more than a cutoff distance. This approximation is accurate for van der Waals forces, which tend rapidly to zero as the distance increases. Additionally, a number of approximations (switching or shifting) have been proposed where the potential is modified so that the forces approach zero or are exactly zero at the cutoff distance.[81] However, this truncation is not longer valid when treating electrostatic forces, which decay much more slowly with the distance. An alternative approach, for a simulation using periodic boundary conditions, is to fully account for the long-range component of the electrostatic interactions, using the particle-mesh Ewald method (PME).[81] The Ewald summation is an infinite sum of charge-charge interactions for an electrostatic neutral system.[73] Within the PME, the electrostatic interactions are divided into two parts: a near component calculated for all atom pairs up to the cutoff distance, and a long-range component.[81]

6.2.2 Simulations set up

Our ultimate goal is to perform MD simulations of chromophore **1a** inside a lipid bilayer. Since it is surrounded by water, the chromophore was first simulated in this environment. The partial charges needed to start the MD simulations were calculated ab initio using the electrostatic potential (ESP) model with the Gaussian16[82] program at the DFT/M06-2X level with the cc-pVDZ
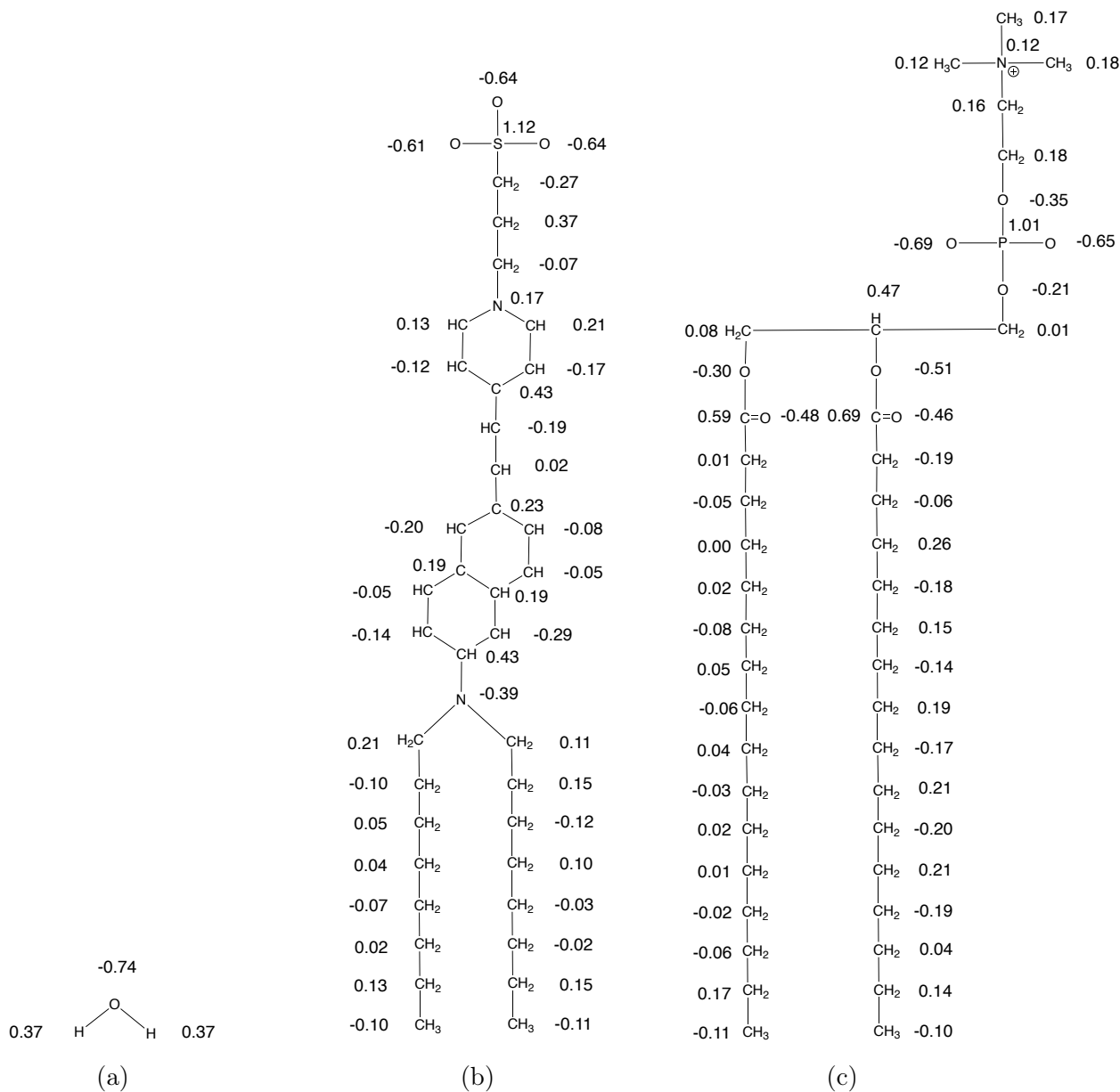
Figure 6.2 – Charge distribution used in the simulations. The numbers next to each charged atom are the partial charges (in a.u.). **(a)** Water molecule; **(b)** Chromophore **1a**, and **(c)** DPPC molecule.

basis set. Figure 6.2 shows the partial atomic charges as computed and as used in the simulation. The initial structure of each system was constructed on the basis of minimized structure of water and/or chromophore **1a** and/or DPPC obtained at the M06-2X/cc-pVTZ level and assembled using Packmol[83] by replicating the individual molecules. A great care was given to this step because previous simulations, especially involving membrane systems, have been showed to be extremely susceptible to the starting conditions.[84,85] The MD simulations were carried out using NAMD2.12[73] (unless specified, the default parameters were used) and visualized and analyzed with VMD1.9.4.[86]

Simulation of the solvent

First, to make sure that the bulk properties of water are reproduced, the solvent alone was simulated using the Simple Point Charge for Flexible water (SPC/Fw)[87] FF. The MD simulation was conducted on a cubic box with sides 30 Å and containing 1000 molecules of water (Figure 6.3). The system was first briefly minimized and then equilibrated for 5 ns using the NPT ensemble via a Berendsen thermostat and barostat,[77] respectively. Lennard-Jones interactions were truncated at 12 Å using a switching function starting at 10 Å while long-range Coulombic interactions are treated by the PME.[81] The time step was 1 fs. Finally, the production step was run over 5 ns using the same conditions.
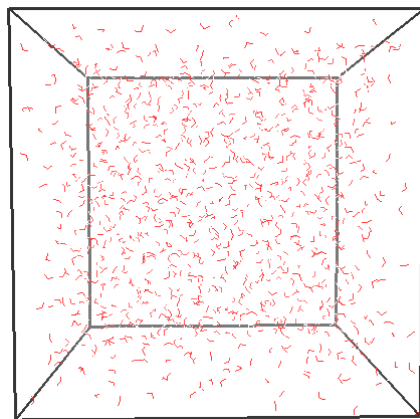

Figure 6.3 – Simulation box containing 1000 water molecules.

Simulation of chromophore 1a in water

In a second step, the MD simulation was conducted for a cubic box of side 44 Å containing one molecule of **1a** (chromophore of 94 atoms) and 4500 molecules of water (Figure 6.4), for a total of 13594 atoms. We used the modified Generalized Amber Force Field (GAFF)[88] (see below)

for the chromophore and the SPC/Fw[87] FF for the water molecules. Again, the system was first minimized and then equilibrated for 3 ns using the NPT ensemble (P = 1 atm and T = 300.0 K) by the means of Berendsen barostat and thermostat,[77] a switching cutoff function starting at 11 Å to 14 Å, PME,[81] and a time step of 1 fs. Finally, the production was run over 10 ns using the same conditions.
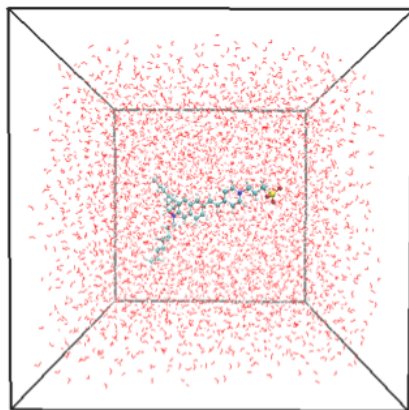

Figure 6.4 – Simulation box containing chromophore **1a** and 4500 water molecules.

Simulation of chromophore 1a inside a lipid bilayer

Finally, the lipid bilayer was modelized following most reccurent MD simulations set ups.[16,28,32,79,89–104] The system consist of 125 DPPC molecules (61 and 64 in the leaflet with and without the chromophore, respectively), one dye molecule and 3840 water molecules, providing a total of 27864 atoms in the simulation (Figure 6.5) and a $3840/125 = 30.72$ water/lipid ratio. We can also define the water content by weight as c $= m_{H_2O}/(m_{H_2O} + m_{DPPC})$. Experimental results suggest that DPPC bilayers in the L_α phase are fully hydrated at c $= 0.36$[105,106] or c $= 0.40$,[107] both values are slightly below our water concentration (c $= 0.42$). Generally, a bilayer with a large amount of water is also expected to mimic a biological membrane better than a system with little water.[?] The MD simulation of chromophore **1a** embedded in the DPPC bilayer was conducted using the CHARMM 36 (C36)[98,108] FF for the lipid molecules, modified GAFF[88] for chromophore **1a**, and the SPC/Fw[87] FF for the water molecules. The initial simulation started from a box with sides of 80 Å and was first minimized. The box was equilibrated for 140 ns using the NPT ensemble (P = 1 atm and T = 315.15 K, the transition temperature of DPPC for the shift between the L_β and L_α phase being 315K[107]). The pressure and temperature were maintained using the Langevin piston[109] and Langevin temperature bath, respectively. Lennard-Jones interactions were truncated

at 12 Å using a switching function starting at 10 Å while long-range Coulombic interactions are treated by the PME[81] technique. The time step used was 1 fs. Periodic boundary conditions were applied in all three dimensions, so that the simulation is actually that of a multilamellar system. The production was run over 240 ns using the same conditions.
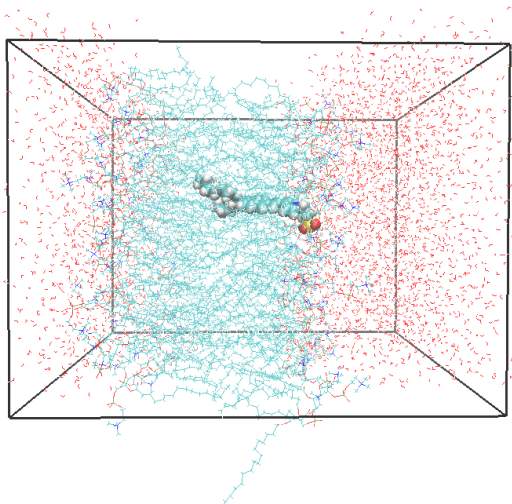

Figure 6.5 – Simulation box containing 125 DPPC, chromophore **1a**, and 3840 water molecules.
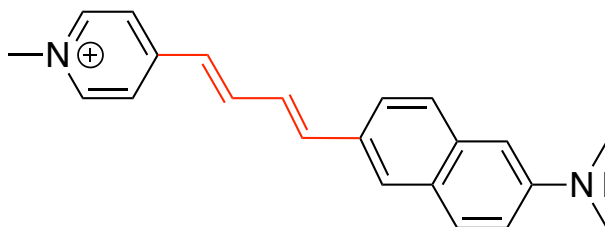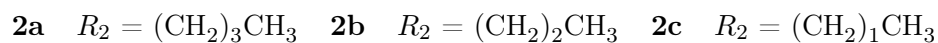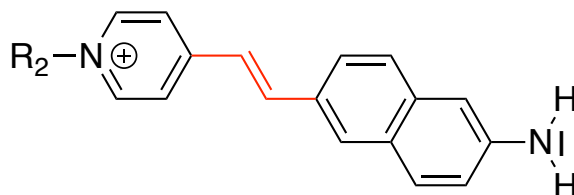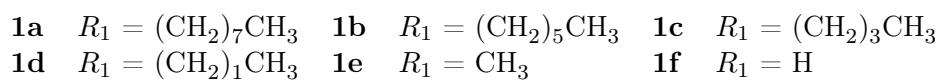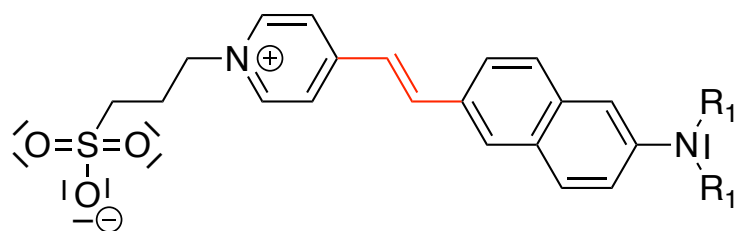
Part III

Results and discussion

Chapter 7

Study of structure-β relationships

7.1 Motivation and definition of the chromophores set

The goal of this Chapter is to uncover relationships between the structure of chromophores and their β_{HRS} responses. In order to do that, a set of chromophores was defined starting from the di-8-ANEPPS (Figure 7.1, compound **1a**), which is a commercially available molecule commonly used in SHG experiments. Various structural parameters of interest were modified, as the size of substituents on either side of the molecule, the length of the π-conjugated path joining the two aromatic moeities, and the position of substituents. Each series is dedicated to the study of one parameter.

For this study, the geometries were optimized at the M06-2X/cc-pVTZ level of approximation in gas phase and in water using the IEFPCM[69–71] implicit solvation scheme. All calculations were carried out using the Gaussian16[82] package.

Starting with chromophore **1a**, series **1** is defined by varying the length of R_1, the alkyl substituents. Going from di-8-ANEPPS, for which R_1 is a chain of eight carbon atoms, the size is progressively reduced to obtain chromophore **1f**, bearing only an amino group. Along the way, chromophores **1b**, **1c**, **1d**, and **1e** were also defined. They possess respectively six, four, two and one carbon atom(s). All chromophores considered are completely planar, meaning that the sulfur of the sulfonate, the aromatic rings, and the backbone of one of the alkyl chains are in the same plane. Furthermore, the alkyl chains are in all-trans conformation. Chromophore **1c*** is

1a $R_1 = (CH_2)_7CH_3$ **1b** $R_1 = (CH_2)_5CH_3$ **1c** $R_1 = (CH_2)_3CH_3$
1d $R_1 = (CH_2)_1CH_3$ **1e** $R_1 = CH_3$ **1f** $R_1 = H$

2a $R_2 = (CH_2)_3CH_3$ **2b** $R_2 = (CH_2)_2CH_3$ **2c** $R_2 = (CH_2)_1CH_3$

3

4a   NCH$_3$ in 1   **4b**   NCH$_3$ in 2   **4c**   NCH$_3$ in 3

4a   N(CH$_3$)$_2$ in 2   **5a**   N(CH$_3$)$_2$ in 1   **5b**   N(CH$_3$)$_2$ in 3   **5c**   N(CH$_3$)$_2$ in 4
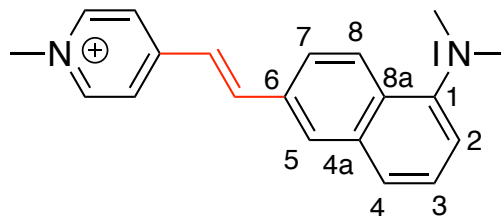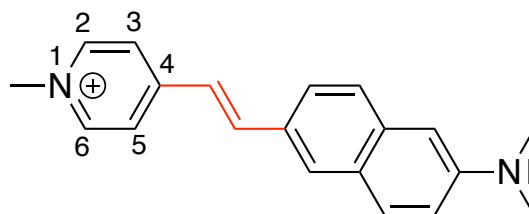
Figure 7.1 – Structures of the chromophores derived from di-8-ANEPPS (**1a**). The segments used to evaluate the bond length alternation (BLA) are highlighted in red. The BLA is defined as the average of the differences between the single and double C-C bond lengths.

the exception. In the latter case, to assess the effect of the position of the sulfonate group, we have also considered another conformer of chromophore **1c** where the sulfonate is bent towards the pyridinium ring, as shown in Figure 7.2.
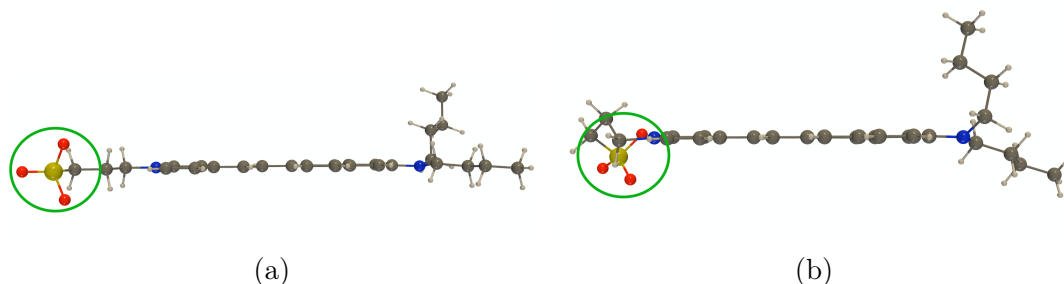

(a)   (b)

Figure 7.2 – **(a)** Planar geometry of chromophore **1c**, and **(b)** geometry of chromophore **1c*** where the sulfonate is bent towards the pyridinium ring.

The second series is also defined by the variation of the length of an alkyl substituent, R_2. The substantial difference between the series **1** and **2** is that series **2** does not include the sulfonate group. As a consequence, compounds of this series (and the following ones) are no longer globally neutral molecules but they display a net positive charge mostly localized on the pyridinium ring. Chromophore **2a** is analogous to chromophore **1f**, where the sulfonate group is replaced by a methyl group, forming therefore a n-butyl R_2 group. Once again, the size of the substituent is progressively reduced with chromophore **2b** (R_2 = n-propyl) and chromophore **2c** (R_2 = ethyl).

Series **3** only includes one compound, for which the π-conjugated path has been lengthened by one carbon-carbon double bond with respect to series **1** and **2**.

The fourth series is build by varying the position of the methyl-nitrogen group of the pyridinium ring. Chromophore **4a** is the analogous to chromophore **2c** where the R_2 substituent has been shortened by one CH_2 unit and the NH_2 substituent has been replaced by a NMe_2 one. For chromophore **4b**, the nitrogen atom goes from the 1-4 position to the 2-4 position with respect to the π-conjugated linker. Following, in chromophore **4c**, the nitrogen atom is in 3-4 position.

In the last series, the influence of the position of the amine group on the aromatic ring is probed. Chromophores **5a**, **4a**, **5b**, and **5c** are defined with the amine substituent successively in 1-6, 2-6, 3-6, and 4-6 positions with respect to the π-conjugated linker.

7.2 Choice of the basis set

To begin with, the first hyperpolarizability of chromophore **4a** was calculated using a collection of atomic basis sets in order to determine the most efficient one. These calculations were performed for the isolated molecule (diluted gas phase) at 1064 nm using the TDHF method. All calculations were carried out using the Gaussian16[82] package.

Basis set	β_{HRS}	$\frac{\beta_{\text{HRS}}}{\beta_{\text{HRS aug-cc-pVTZ}}}$	DR	cpu time
STO-3G	24.0	0.60	4.92	44
6-31G	36.1	0.90	4.90	319
6-31G*	36.2	0.90	4.90	1289
6-31+G*	40.5	1.00	4.91	6461
6-311+G*	40.5	1.00	4.91	12982
cc-pVDZ	37.5	0.93	4.90	2939
cc-pVTZ	38.8	0.96	4.91	51867
aug-cc-pVDZ	40.7	1.01	4.92	54063
aug-cc-pVTZ	40.3	1.00	4.92	1144353
d-aug-cc-pVDZ	40.6	1.01	4.92	129292

Table 7.1 – TDHF β_{HRS} (in 10^3 a.u.) and DR of chromophore **4a** in gas phase ($\lambda = 1064$ nm) as computed for a collection of basis sets in comparison to the cpu time (s). The ratios with respect to the reference aug-cc-pVTZ basis set are given in the third colunm.

Results in Table 7.1 highlight first that the choice of the basis set is crucial. Indeed, the β values change by about a factor 2 from the minimal STO-3G basis set to aug-cc-pVDZ while β is underestimated in absence of diffuse functions. Owing to its size (valence triple-ζ) as well as to the negligible impact of adding a second set of diffuse functions (d-aug-cc-pVDZ versus aug-cc-pVDZ), the aug-cc-pVTZ basis set was chosen as the reference and all the basis sets were compared to it. Both the 6-31+G* and the 6-311+G* basis sets stood out from the other ones because they yielded the closest β values in regards to the aug-cc-pVTZ result in the least cpu time possible. Later, the 6-311+G* basis set was preferred because in addition to present a good balance between diffuse and polarization functions, it is a valence triple-ζ, which is important for predicting molecular structures and relative energies. Moreover, results show that the DR is almost independent of the basis set. As a matter of fact, in this Chapter, for the computation of β, the 6-311+G* basis set is employed, in conjunction with the TDHF approach, for a 1064 nm wavelength.

7.3 Calculation of the first hyperpolarizability in gas phase using QM approaches

The first hyperpolarizability values for the entire set of chromophores calculated in gas phase are presented in Table 7.2. All values are of the same order of magnitude, i.e. of the order of 10^4 a.u.. On the one hand, chromophore **3** exhibits the largest β_{HRS} value (93.8×10^3 a.u.), owing to its longer π-conjugated path. On the other hand, (besides **1c***, see below) chromophore **5b** (12.0×10^3 a.u.) yields the lowest β_{HRS} value.

As shown in Table 7.2, the longer the R_1 substituent (i.e. the stronger the donor) is, the larger the β_{HRS} value of the compounds of series **1**, except for compound **1c***. β_{HRS} values range from 20.5×10^3 a.u. for chromophore **1a** bearing the longest R_1 chains (R_1 = octyl) to 12.1×10^3 a.u. for chromophore **1f** for which R_1 = one hydrogen atom. This is the result of a progressive diminution of approximately 14 % when going from **1a** to **1d** and of 30 % when going from chromophore **1e** to **1f**. For chromophore **1c***, as said before, to assess the effect of the position of the sulfonate group, we have considered another conformer where the sulfonate is bent towards the pyridinium ring. The presence of this nearby anion "electrostatically" reduces the acceptor character of the pyridinium ring, and therefore leads to a decrease of β_{HRS}. In gas phase, a value of 20.1×10^3 a.u. is found for chromophore **1c**, whereas a value of 10.3×10^3 a.u. is found for chromophore **1c***, corresponding to a decrease by approximately 50 %.

In series **2**, the β_{HRS} values are larger than those of compound **1f** (the corresponding compound from the **1a-1f** series, which also bears an amino donor group). β_{HRS} goes from 12.1×10^3 a.u. for chromophore **1f** to 26.6×10^3 a.u. for chromophore **2a**. This effect is attributed to the cationic nature of the compounds in series **2** whereas, in the first series, the terminal SO_3^- damps the acceptor character of the pyridinium moiety. Note that, in parallel, the bond length alternation (BLA), which is a measure of the π-delocalization between the donor and acceptor moieties, decreases from **1f** ($0.10\,\text{Å}$) to **2a-2c** (0.07 - $0.08\,\text{Å}$). Table 7.2 also shows that the length of the alkyl chain R_2 does not really matter. Indeed, β_{HRS} values vary by less than 5% while chromophore **2c**, bearing the smallest R_2 chain, exhibits the largest β_{HRS} of its series (27.8×10^3 a.u.).

Chromophore	$\beta_{\text{HRS gas}}$	$\beta_{\text{HRS TSA gas}}$	BLA_{gas}	DR	$\beta_{\text{HRS H}_2\text{O}}$	$\beta_{\text{HRS TSA H}_2\text{O}}$	$BLA_{\text{H}_2\text{O}}$	DR	$\frac{\beta_{\text{HRS H}_2\text{O}}}{\beta_{\text{HRS gas}}}$	$\frac{\beta_{\text{HRS TSA H}_2\text{O}}}{\beta_{\text{HRS TSA gas}}}$
1a	20.5	28.9	0.10	4.87	18.0	36.7	0.12	4.82	0.88	1.27
1b	20.2	28.4	0.11	4.86	17.8	36.4	0.12	4.81	0.88	1.28
1c	20.1	27.7	0.10	4.86	19.5	36.0	0.11	4.82	0.95	1.30
1c*	10.3	17.9	0.11	4.79	15.8	34.7	0.11	4.81	1.53	1.93
1d	17.6	24.9	0.10	4.84	16.5	34.1	0.11	4.79	0.94	1.37
1e	17.3	23.4	0.10	4.83	17.5	35.0	0.11	4.79	1.01	1.49
1f	12.1	12.9	0.10	4.80	12.2	23.9	0.11	4.75	1.01	1.85
2a	26.6	13.3	0.08	4.88	18.0	16.1	0.11	4.78	0.68	1.21
2b	26.5	19.5	0.08	4.88	11.5	21.0	0.11	4.73	0.43	1.08
2c	27.8	19.6	0.07	4.89	11.8	22.8	0.11	4.74	0.42	1.16
3	93.8	51.3	0.05	4.94	27.0	58.1	0.09	4.83	0.29	1.13
4a	40.5	26.4	0.07	4.91	16.8	33.8	0.10	4.78	0.41	1.28
4b	18.9	24.1	0.09	4.96	7.0	21.6	0.12	4.82	0.37	0.90
4c	25.5	17.9	0.07	4.91	12.0	19.8	0.10	4.82	0.47	1.11
5a	12.1	3.4	0.09	4.97	5.3	15.9	0.12	4.85	0.44	4.66
5b	12.0	13.0	0.09	5.20	5.7	12.4	0.11	5.23	0.47	0.95
5c	14.6	17.8	0.08	4.93	6.2	15.8	0.11	4.71	0.43	0.89

Table 7.2 – TDHF $\beta_{\text{HRS gas}}$ and $\beta_{\text{HRS H}_2\text{O}}$ (in 10^3 a.u.) ($\lambda = 1064\,\text{nm}$) computed for the entire set of chromophores, β_{HRS} calculated using the two state approximation ($\beta_{\text{HRS TSA gas}}$ and $\beta_{\text{HRS TSA H}_2\text{O}}$), BLA (in Å) as well as DR values. The last two columns report the H$_2$O/gas β ratios

As said before, chromophore **3** possesses an additional double bond in the π-conjugated path joining the two aromatic moieties, resulting in the highest β_{HRS} value of the entire set of chromophores. This goes hand in hand with the lowest BLA value (i.e. 0.05 Å). This is also consistent with the study of Reeve and coworkers,[16] who demonstrates that the first hyperpolarizability tends to increase with the bridge length. However, as mentioned in Chapter 2, there is a balance to find between the large NLO response induced by long π-conjugated path and the solubility of the molecule.

In series **4**, the effect of the position of the methyl-nitrogen group around the pyridinium ring is probed. The largest β_{HRS} value is achieved for **4a** (40.5×10^3 a.u.) where the nitrogen atom is in 1-4 position with respect to the π-conjugated path. Then, comes the β_{HRS} of **4c** (where the nitrogen atom is in 3-4 position), which is smaller because the donor-acceptor length gets smaller. Finally, β_{HRS} further decreases in **4b** (18.9×10^3 a.u.) because the π-electron delocalization with the nitrogen atom in 2-4 position is not possible, as shown in Figure 7.3. This diminution is nicely corroborated by an increase of the BLA value going from chromophores **4a** and **4c** (0.07 Å) to chromophore **4b** (0.09 Å).

Similar trends but smaller variations are observed in series **5** when moving the amino donor group on the terminal ring. The push-pull effect is not possible for chromophores **5a** and **5b** (β_{HRS} = 12.1×10^3 a.u. and 12.0×10^3 a.u., respectively) (Figure 7.3). On the contrary, chromophore **5c** manifests a larger β_{HRS} (14.6×10^3 a.u.) than the other compounds of its series. It is also important to note that in Series **5**, when the nitrogen atom is in position 2-6, the molecule is identical to chromophore **4a**. The latter has the largest β_{HRS} response among series **4** and **5**.

The DR values were also calculated and are all close to 5, the typical value for push-pull compounds, with a unique dominant, diagonal, β tensor component. Globally, molecules exhibiting longer π-delocalization paths, also display DR values closer to 5. Chromophore **3** is the best example of that. It possesses the largest π-conjugated path, exhibits the largest β_{HRS} ($93.8\ 10^3$ a.u.) and the fourth largest DR (4.94).
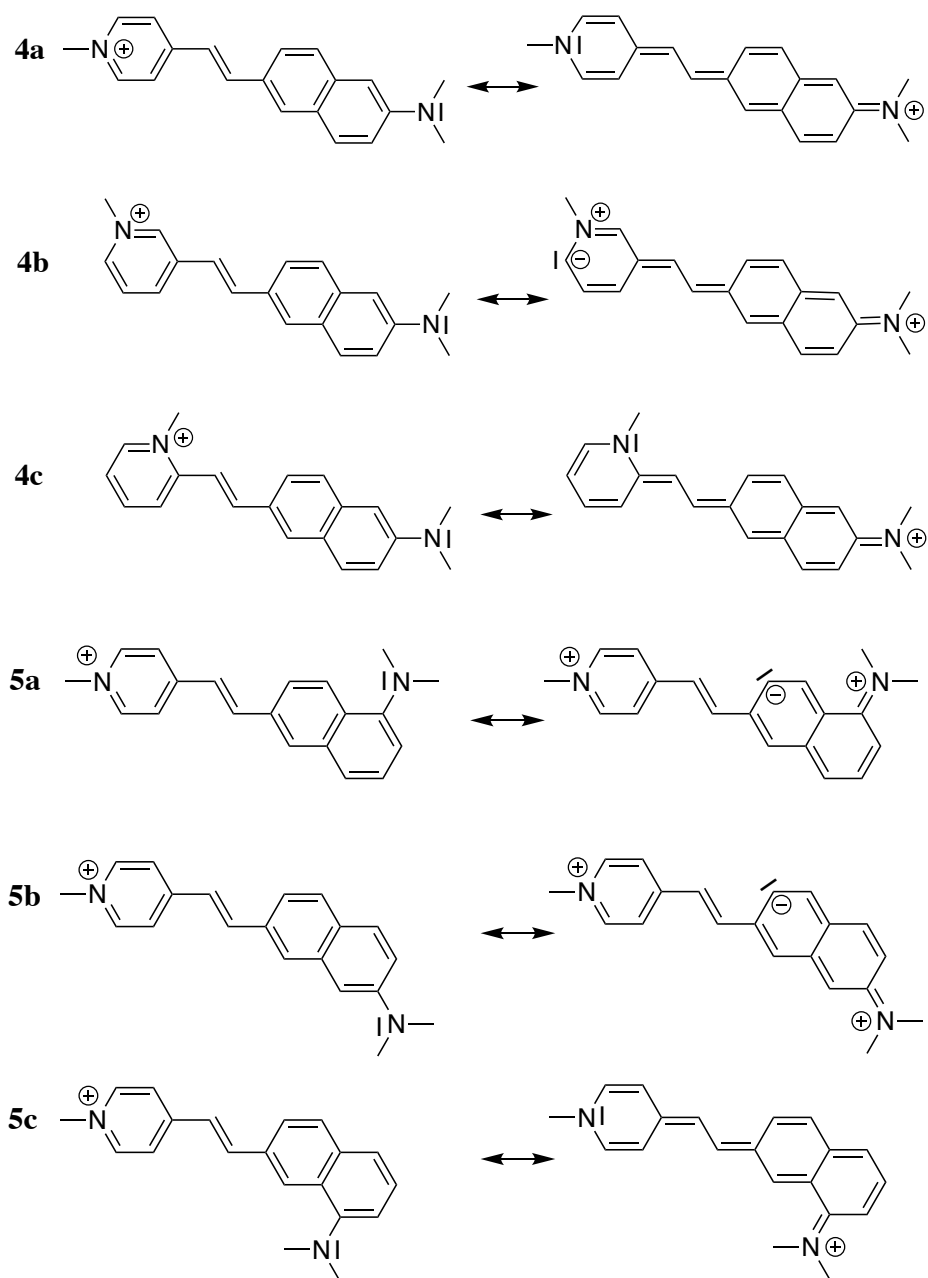
Figure 7.3 – Selected resonance structures for compounds of series **4** and **5**.

7.4 Calculation of the first hyperpolarizability in water using QM approaches

Table 7.2 also lists the calculated β_{HRS} in water and the $\beta_{\text{HRS H}_2\text{O}}/\beta_{\text{HRS gas}}$ ratios. The analysis made in the previous section concerning the β-structure relationships is still relevant in aqueous phase. Indeed, similar trends are found in water. The overall effect of the solvent is to reduce the acceptor character of the positively charged acceptor group. For example, chromophore **1a** displays a β_{HRS} of 20.5×10^3 a.u. in gas phase but of 18.0×10^3 a.u. in water. Indeed, during the solvation process, the solvent molecules orient their dipole moments to form a stabilizing solvation shell around the solute. The shielding of the nitrogen charge induces a decrease of the β_{HRS} and a slight increase of the BLA. Note that these effects are stronger for the species without a sulfonate group, which already provides a damping effect on the pyridinium acceptor character. For example, the NLO response of chromophore **4a** drops from 40.5×10^3 a.u. to 16.8×10^3 a.u. when going from gas phase to water. As a consequence, for chromophores of group **1**, the $\beta_{\text{HRS H}_2\text{O}}/\beta_{\text{HRS gas}}$ ratio is close to one (with the exception of **1c***, which adopts another conformation), but this is not the case for the remaining molecules where this ratio is substantially smaller than one and ranges from 0.3 to 0.7. The β_{HRS} results are particularly different for chomophore **3** when going from the gas phase (93.8×10^3 a.u.) to the aqueous phase (27.0×10^3 a.u.), resulting in the smallest $\beta_{\text{HRS H}_2\text{O}}/\beta_{\text{HRS gas}}$ ratio (i.e. 0.29). Despite this diminution, in water, chromophore **3** still displays the highest NLO response among the set of chromophores.

To a large extent, the results presented in Sections 7.3 and 7.4 can be analyzed using Figure 7.4 where the evolution of β is described as a function of the strength of the donor and acceptor groups, in relation with the BLA of the π-conjugated segment. In that model, weak donor and acceptor groups present a small β response and quite large and positive BLA. It means that the canonical covalent form is dominant in the electronic ground state (Figure 7.4, zone A). In this zone, an increase of the CT goes hand in hand with a decrease of the BLA and an increase of β. If the donor/acceptor strength further increases, the weight of charge-transfer resonance structure gets larger, resulting in a smaller BLA and a decreasing β (Figure 7.4, zone B). When both forms have equal contributions, BLA and β are more or less equal to zero. Finally, negative BLA values appear when the charge-transfer form dominates (Figure 7.4, zones C and D). Results presented

in Table 7.2 show that the compounds belong to zones A and B since the BLA is always positive. Note that for our chromophore, the acceptor is positively charged.
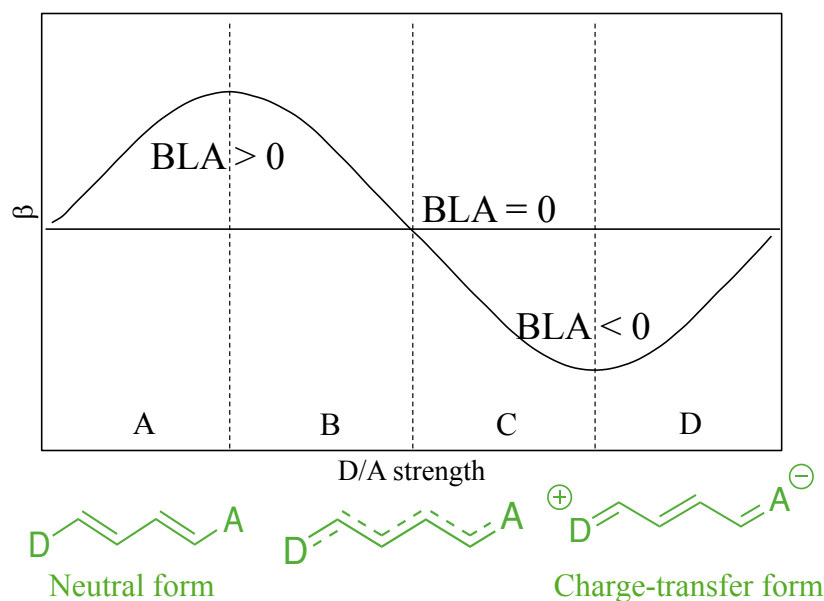

Figure 7.4 – Evolution of β as a function of the strength of the donor and acceptor moieties.[110] The corresponding resonance structures and BLA values are superimposed to the curve.

7.5 Analysis of the first hyperpolarizability using the two-state approximation

One way to rationalize the β_{HRS} results is to use the two-state model,[34,35] involving the transition dipole between the ground and excited states (μ_{eg}), the difference between the ground and excited states dipole moments ($\Delta\mu_{eg}$), and the corresponding excitation energy (E_{eg}), as written in Equation 7.1. Of course, the goal consists in searching for qualitative relationships between the β_{HRS} responses and simple spectroscopic quantities. More is indeed not possible because only one excited state has been considered. All three spectroscopic quantities, computed at the TDDFT/M06-2X/6-311+G* level in gas phase or in water (IEFPCM),[69–71] allow us to obtain the dominant diagonal tensor component (β_{zzz}). Then, Equation 7.2 is needed to convert β_{zzz} into β_{HRS}, assuming the other components are negligible.

$$\beta_{\text{zzz TSA}} = 6\,\frac{\mu_{eg}^2 \Delta\mu_{eg}}{E_{eg}^2} \tag{7.1}$$

$$\beta_{\text{HRS TSA}} = \sqrt{\frac{6}{35}}\beta_{zzz} \tag{7.2}$$

β_{HRS} calculated using the TSA ($\beta_{\text{HRS TSA}}$) are presented in Table 7.2 for both the gas and the aqueous phases. The $\beta_{\text{HRS TSA}}$ results are of the same order of magnitude as the TDHF ones, which allows us to use the former for rationalizing the latter. On the other hand, they do not follow every variations observed with TDHF. The most striking example originates from series **5**. Indeed, in gas phase, chromophores **5a** and **5b** display extremely similar NLO responses (12.1×10^3 a.u. and 12.0×10^3 a.u., respectively) but different TSA values (3.4×10^3 a.u. and 13.0×10^3 a.u., respectively). The same observation can be made for chromophores **2a** and **2b**. Moreover, for chromophores **4b-4c** in gas phase and **2a-2b-2c**, **4b-4c** and **5a-5b-5c** in water, the relative amplitudes of the $\beta_{\text{HRS TSA}}$ are inverted in comparison to the $\beta_{\text{HRS TDHF}}$. For example, in water, chromophore **4c** displays a larger $\beta_{\text{HRS TDHF}}$ than chromophore **4b** (12.0×10^3 a.u. and 7.0×10^3 a.u., respectively). The reverse order is found for the TSA results (19.8×10^3 a.u. and 21.6×10^3 a.u., respectively). On the contrary, chromophore **3** diplays the highest $\beta_{\text{HRS TSA}}$ in both gas and aqueous phases. As the bridge length increases, the oscillator strength increases as well, resulting in a decrease of E_{eg} and an increase of the β_{HRS} (see later, Table 7.3). However, $\beta_{\text{HRS TSA}}$ is larger in solution than in gas phase (51.3×10^3 a.u. and 58.1×10^3 a.u., respectively). The opposite was found for the TDHF results. In fact, for the remaining series, the $\beta_{\text{HRS TSA H}_2\text{O}}$ values are practically always larger than the $\beta_{\text{HRS TSA gas}}$. This inversion can be further illustrated when looking at the $\beta_{\text{HRS TSA H}_2\text{O}}/\beta_{\text{HRS TSA gas}}$ ratios, which are almost systematically all larger than one (with the exception of chromophores **4b**, **5b** and **5c**). This is particularly true for chromophore **5a** where this ratio amounts to 4.66.

Besides the specific comparisons, it is important to have a global look at the relationships between the $\beta_{\text{HRS TDHF}}$ and $\beta_{\text{HRS TSA}}$ values and perform a linear regression between the two sets. As a matter of fact, the correlation is slightly better in aqueous phase than in gas phase, as shown in Figure 7.5. Coefficients of correlation (R^2) amount to 0.62 and 0.76 in gas and aqueous phases, respectively. This Figure also highlights the fact that the different series do not behave likewise
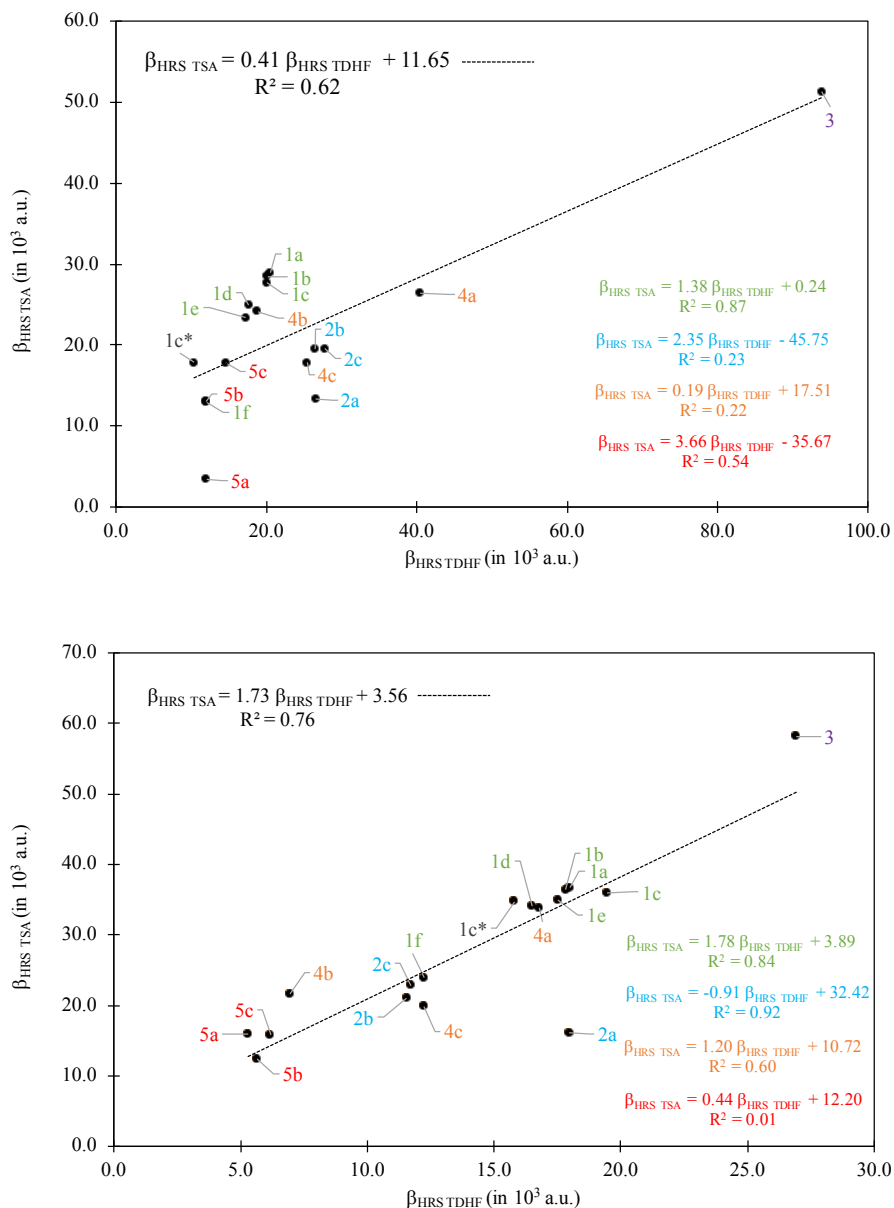
Figure 7.5 – $\beta_{\text{HRS TSA}}$ values as a function of the $\beta_{\text{HRS TDHF}}$ ones, both in 10^3 a.u. **(top)** in gas phase, and **(bottom)** in water.

Chromophore	μ_{eg}^2	$\Delta\mu_{eg}$	$\frac{1}{E_{eg}^2}$	$\beta_{zzz\ \text{TSA}}$	$\beta_{\text{HRS TSA}}$
1a	22.4	7.7	83.3	88.7	36.7
1b	22.3	7.7	83.3	88.0	36.4
1c	22.1	7.7	83.3	86.8	35.9
1c*	21.5	7.8	83.3	83.8	34.7
1d	21.5	7.6	83.3	82.3	34.1
1e	21.3	7.6	90.9	84.4	34.9
1f	19.2	6.6	76.9	57.8	23.9
2a	18.8	4.6	76.9	38.9	16.1
2b	18.5	6.1	76.9	50.8	21.0
2c	18.2	6.6	76.9	55.0	22.8
3	27.4	8.8	100.0	140.4	58.1
4a	20.3	7.6	90.9	81.7	33.8
4b	13.4	7.4	71.4	43.3	21.6
4c	18.9	5.1	83.3	47.9	19.8
5a	8.0	7.5	66.7	23.5	15.9
5b	17.0	4.9	58.8	30.0	12.4
5c	10.4	6.4	71.4	28.8	15.8

Table 7.3 – Spectroscopic quantities involved in the TSA expansion of β_{zzz} for the whole list of chromophores [(μ_{eg}^2 (in 10^3 a.u.^{2}), $\Delta\mu_{eg}$ (in 10^3 a.u.), and $\frac{1}{E_{eg}^2}$ (in 10^3 a.u.$^{-2}$)] as well as the corresponding $\beta_{zzz\ \text{TSA}}$ and $\beta_{\text{HRS TSA}}$ values (both in 10^3 a.u.). All values were computed in aqueous phase.

in gas and in water. Indeed, the series displaying the best correlation in gas phase (series **1**) does not perform as well in aqueous phase (series **2**).

To further analyze the $\beta_{\text{HRS TSA}}$ results, Table 7.3 lists the three quantities taking part in the approximation for the whole set of chromophores while Figure 7.6 presents the evolution of $\beta_{\text{HRS TDHF}}$ as a function of each of these three spectroscopic quantities. The best correlation is found for μ_{eg}^2 ($R^2 = 0.81$), while $\frac{1}{E_{eg}^2}$ also displays an excellent coefficient of correlation of 0.78. On the contrary, $\Delta\mu_{eg}$ only presents a R^2 of 0.23.

To a given extend, variations in $\beta_{\text{HRS TDHF}}$ can be explained by the variations of one, two or the three components of the TSA equation. For example, the diminution of $\beta_{\text{HRS TDHF}}$ when going from chromophore **1e** to **1f** is illustrated by a simultaneous decrease of μ_{eg}^2, $\Delta\mu_{eg}$ and $\frac{1}{E_{eg}^2}$. Similarly, the highest values for the spectroscopic quantities are found for chromophore **3**, displaying the largest NLO response. Moreover, if we focus on μ_{eg}^2, most of the variations of $\beta_{\text{HRS TDHF}}$ are reproduced. Indeed, in each series, we can order the chromophores based on their $\beta_{\text{HRS TDHF}}$ or on
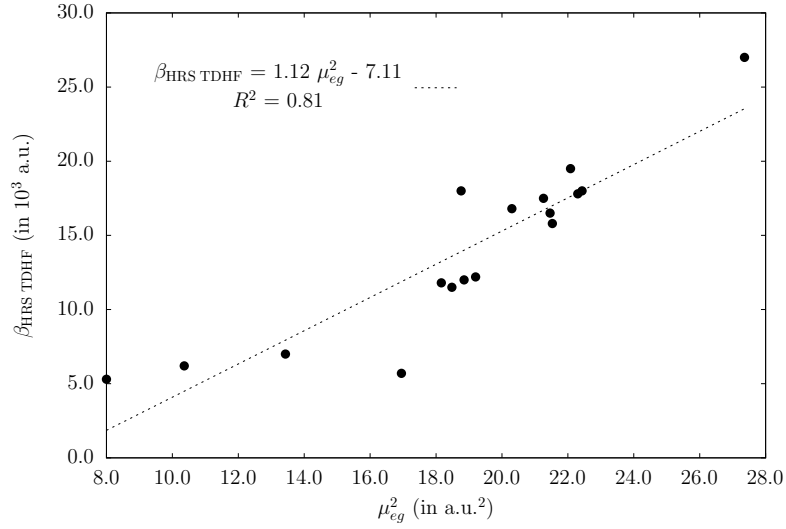
(a)
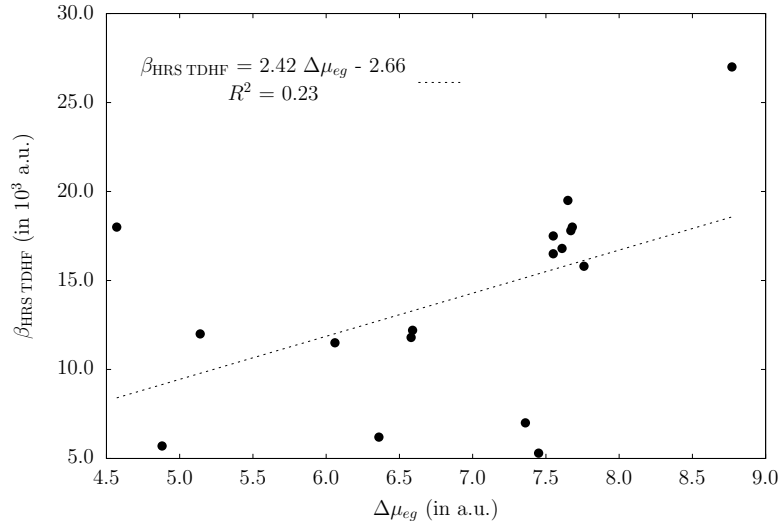
(b)
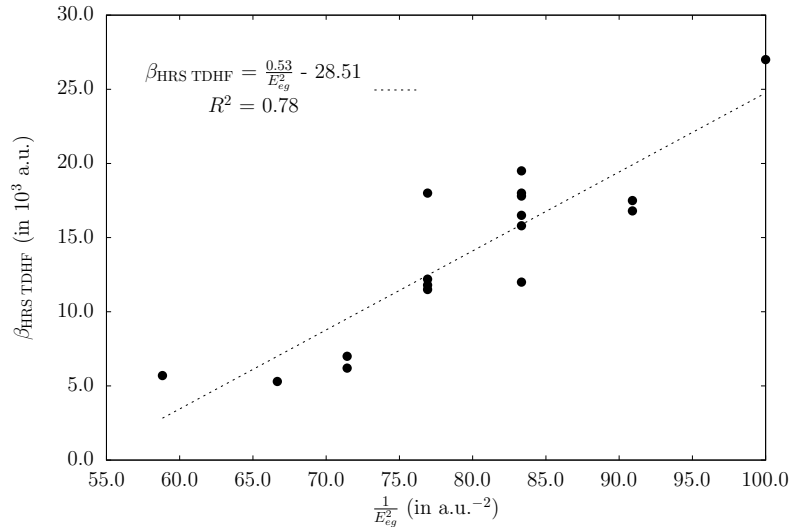
(c)

Figure 7.6 – $\beta_{\text{HRS TDHF}}$ (in 10^3 a.u.) as a function of **(a)** μ_{eg}^2; **(b)** $\Delta\mu_{eg}$, and **(c)** $\frac{1}{E_{eg}^2}$. All values were computed in aqueous phase.

their μ_{eg}^2, resulting in essentially the same ordering. Chromophores **2b-2c** and **5a-5b-5c** being the exceptions. Similar trends but with small variations are found for $\frac{1}{E_{eg}^2}$. In this case, chromophores **5a-5b** contradict the rule.

Lastly, it is important to note that discrepancies can originate from the fact that the $\beta_{\text{HRS THDF}}$ values are compared to $\beta_{\text{HRS TSA}}$ evaluated using spectroscopic quantities calculated with the TDDFT/M06-2X method.

7.6 Conclusions

In this Chapter, the β-structure relationships were investigated. In order to do that, a set a chromophores was designed by modifying the structure of the commercially available molecule di-8-ANEPPS. Firstly, the method used to compute the first hyperpolarizability was examined and the combination of TDHF method and 6-311+G* basis set was chosen.

The first hyperpolarizability results obtained using the TDHF approach have, on the one hand, emphasized the complexity of the β-structure relationships in these ANEP-like compounds. The size of the π-conjugated bridge joining the two aromatic moieties as well as length of the π-delocalization path (i.e. dictated by the position of the substituent) have been identified as crucial geometrical parameters. The longer the bridge or the path is, the larger the NLO response. The presence or absence of the sulfonate group, which reduces the acceptor character of the pyridinium ring, has also been shown to have great impact on the amplitude of β_{HRS}. On the contrary, the length of the alkyl substituents on either sides of the molecules does not really matter. On the other hand, the importance of including solvent effects in the calculations has also been highlighted. Even if similar trends are found in gas and in aqueous phases, the first hyperpolarizabilities computed in water are lower than in gas phase. Indeed, the solvent reduces the acceptor character of the positively charged methyl-pyridinium, and therefore induces a decrease of β_{HRS}.

Concerning the TSA analysis, it offers a qualitative frame to interpret the β_{HRS} values. In particular, a global relationship has been found between β_{HRS} and $\frac{1}{E_{eg}^2}$ as well as between β_{HRS} and μ_{eg}^2 but not with $\Delta\mu_{eg}$, showing the limit of the TSA model.

Chapter 8

Modeling of the chromophore in increasingly complex environments

The goal of this Chapter is to study and analyze the NLO responses of one chromophore molecule embedded in different environments. This is performed by combining MD simulations and TDDFT hyperpolarizability calculations. First of all, chromophore **1a** was modeled in an aqueous environment, using explicit water molecules. Explicit solvent is able to recover most of the solvation effects of real solvent. This offers additional information to that provided in the previous Chapter, focusing on the implicit solvation model and considering a static description of the geometry. Indeed, MD simulations provide information on molecular mobility at the atomic level. Then, the same chromophore was introduced into a lipid bilayer. This complex environment gives insight into the behavior of the dye when it is surrounded by amphiphilic and bulky molecules.

8.1   Chromophore in water

8.1.1   Validity of the Force Fields for predicting th geometry of the chromophore in view of calculating β responses

Generalized Amber Force Field (GAFF)

Preliminary results   In a first step, the performance of GAFF[88] to predict the geometries of push-pull π-conjugated systems has been addressed by considering chromophore **1a** and calculating its β responses. Indeed, as shown in the previous chapter, β is very sensitive to the geometry. So,

using the geometry of **1a** optimized with GAFF (called the MM geometry), β was calculated and compared to the value obtained using the geometry that was optimized at the DFT/M06-2X level (called the QM geometry) (Table 8.1). Though at the TDHF level both geometries give similar β results, the difference is large when using TDDFT/M06-2X. This originates from differences in the geometries (Figure 8.1) (and the fact that both methods do not behave in the same way with respect to the geometry). At the MM level, the standard GAFF predicts a quasi equalization of the carbon-carbon bond lengths within the aromatic rings (1.395 ± 0.005 Å) whereas DFT results show that adjacent carbon-carbon bond lengths can sometimes differ by as much as 0.05 Å. Moreover, DFT calculations predict a BLA of 0.10 Å, whereas GAFF produces a geometry with a BLA of 0.15 Å. Finally, the GAFF geometry is not completely planar and presents an out-of-plane distortion of approximately 15° in comparison to the DFT planar structure. This demonstrates that the force field has to be re-parameterized for our purpose.

	QM geometry		MM geometry	
Method for calculating the β responses	β_{HRS}	DR	β_{HRS}	DR
TDHF	20.5	4.87	19.0	4.88
TDDFT/M06-2X	86.4	4.98	194.0	4.98

Table 8.1 – TDHF and TDDFT/M06-2X β_{HRS} (in 10^3 a.u.) ($\lambda = 1064$ nm) and DR values for chromophore **1a** in gas phase computed using geometries optimized at the DFT/M06-2X and MM/GAFF levels.
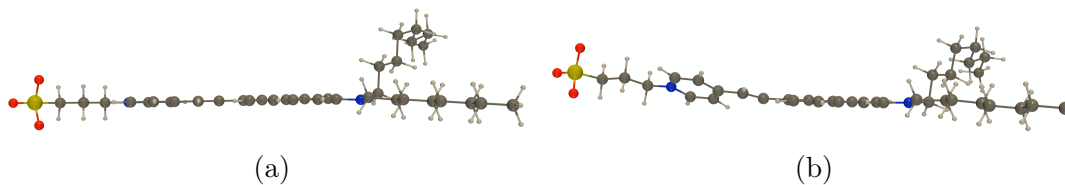

(a)   (b)

Figure 8.1 – Chromophore **1a** geometries obtained using the **(a)** DFT/M06-2X level (QM geometry), and **(b)** MM/GAFF level (MM geometry).

GAFF re-parametrization   In order to re-parameterize the force field, relaxed potential energy scans (PESs) were computed and used as input for the Adaptive Biasing Force Method.[111] This was done in collaboration with Dr. Claire Tonnelé from the University of Bordeaux. Chromophore **4a** was chosen as a model compound because it presents the basic skeleton of the entire set of chromophores. Furthermore, given its small substituents R_1 and R_2, the computational cost is reduced in comparison to chromophore **1a**. The main difference between chromphores **1a** and
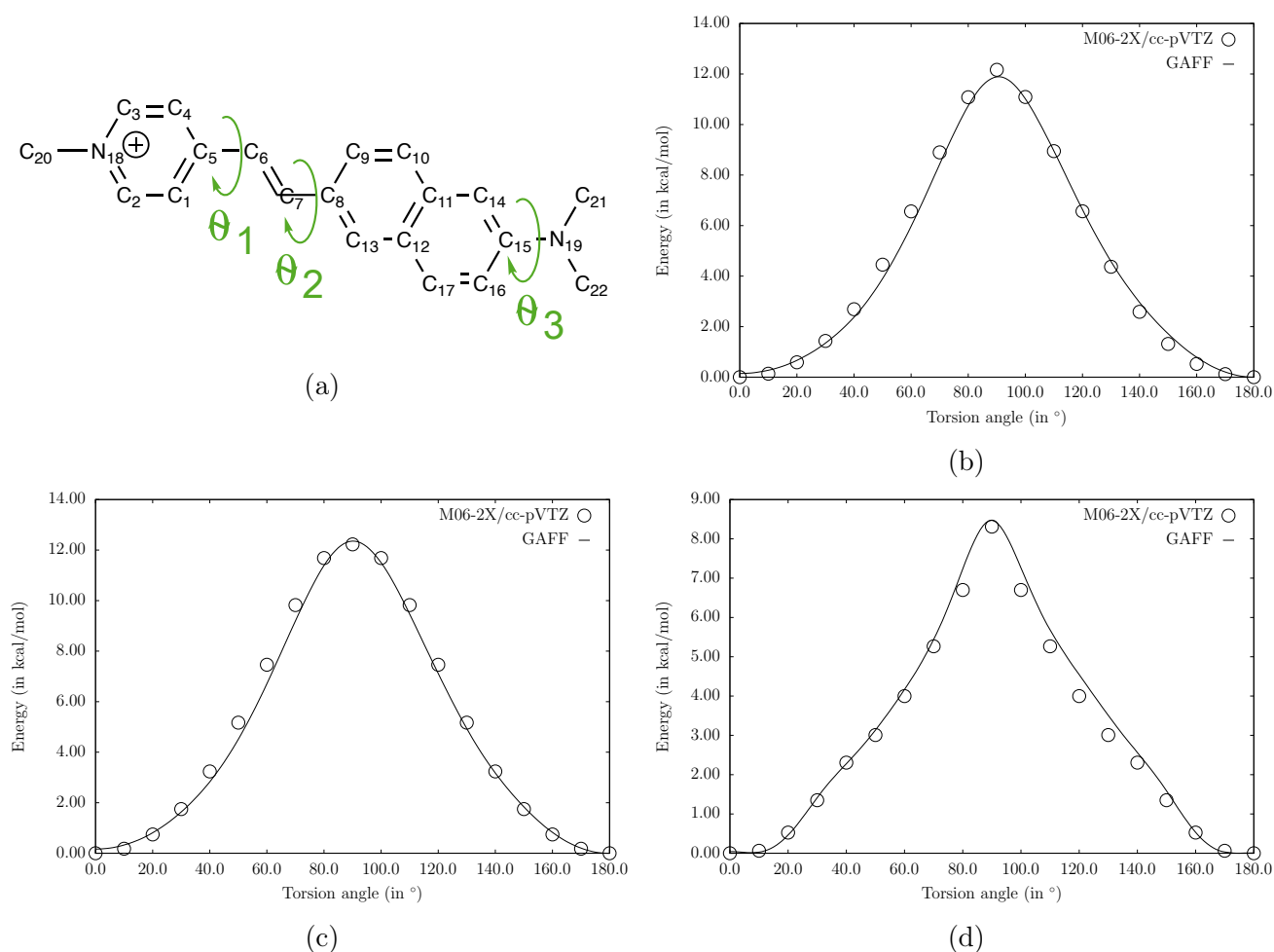
Figure 8.2 – **(a)** Chromophore **4a**, atomic labels, and definition of the $\theta_1 = \theta(C_4 - C_5 - C_6 - C_7)$, $\theta_2 = \theta(C_6 - C_7 - C_8 - C_{13})$, and $\theta_3 = \theta(C_{16} - C_{15} - N_{19} - C_{21})$ torsion angles; **(b)** θ_1 relaxed PES ($\theta_2 = 180°$, $\theta_3 = 180°$); **(c)** θ_2 relaxed PES ($\theta_1 = 180°$, $\theta_3 = 180°$), and **(d)** θ_3 relaxed PES ($\theta_1 = 180°$, $\theta_2 = 180°$). All three relaxed PESs are computed for chromophore **4a** in gas phase at the DFT/M06-2X/cc-pVTZ level [circles], and fit of the GAFF parameters to produce the re-parameterized GAFF [line].

4a is the charge: **1a** is neutral whereas **4a** bears one positive charge. Still, this has no impact on the key elements of the re-parametrization. Three dihedral angles were defined, as shown in Figure 8.2a. These PESs were computed in gas phase at the DFT/M06-2X/cc-pVTZ level by rotating successively around each dihedral angle by steps of 10°. The choice of M06-2X relies on a complementary investigation where this functional was found to closely reproduce reference MP2 data whereas the latter method is computationally much more expensive and can therefore not be applied to obtain the PESs of **4a** in a reasonable amount of time. Here, relaxed PESs were computed. This means that only the dihedral angle studied is fixed and the rest of the molecule is fully optimized.

As shown in Figure 8.2, the PESs are both qualitatively (shape) and quantitatively (amplitude) reproduced by the re-parameterized FF. For instance, using DFT/M06-2X as the method for geometry optimization, chromophore **4a** is completely planar. The least stable conformations occur at $\theta=90°$ and are characterized by an energy barrier of 12.16 kcal/mol, 12.22 kcal/mol and 8.31 kcal/mol for θ_1, θ_2 and θ_3, respectively.

Besides the re-parameterization of the dihedral angles, atom types were also added to the FF to reproduce the BLA throughout the molecule, which was shown to be crucial for β calculations. Indeed, originally, the GAFF contained only one atom type to describe aromatic carbons, 'ca'.[88] To better reproduce the bond lengths in the aromatic rings, this 'ca' type was differentiated and the 'cx', 'cn', 'cz', and 'cm' types were added, as shown in Table 8.2. This Table presents also all the GAFF atom types needed later for MD simulations on the selected chromophore, chromophore **1a**. They are then illustrated in Figure 8.3. As you can see, the newly introduced atom types were displayed by group of two around the aromatic rings of the molecule. This allowed us to meticulously set the bond lengths to be close to the QM ones. To finish the re-parametrization, some force constants and equilibrium bond lengths were also adjusted throughout the molecule.

Atom types	
c2	sp^2 carbon
c3	sp^3 carbon
ca → cx, cn, cz, cm	sp2 carbon in pure aromatic systems
na	sp2 nitrogen with three connected atoms
nh	Amine nitrogen connected to one or more aromatic rings
s6	Sulfur with four connected atoms
o	Oxygen with one connected atom
ha	H bonded to aromatic carbon
hc	H bonded to aliphatic carbon without electronwithdrawing group

Table 8.2 – GAFF atom types used for chromophore **1a**[88] as well as the parameters added for the aromatic carbons.

The new FF was then applied to the selected compound, chromophore **1a** for geometrical and properties validation. When comparing the bond lengths obtained via DFT calculations (M06-2X) and those using the re-parameterized FF, the differences are of the order of 0.002-0.005 Å, with very few exceptions. Indeed, the average error on the bond lengths (in comparison to the QM geometry) using the standard FF was of 0.013 Å and the average error for the aromatic bond lengths was 0.023 Å. In this case, the re-parameterized GAFF predicts a BLA of 0.10 Å for the equilibrium
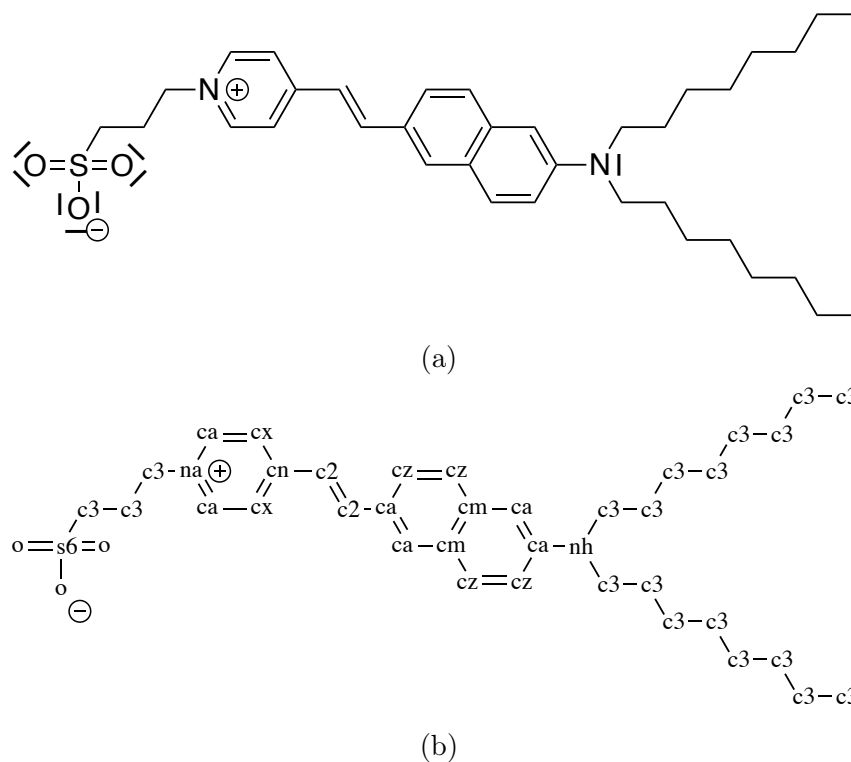
(a)

(b)

Figure 8.3 – **(a)** Chromophore **1a** structure, and **(b)** its atom types as used in the GAFF re-parameterization.

geometry, which is the same value as that obtained at the DFT level (Table 7.2). Whether the new FF is able to reproduce accurately the β responses of the chromophore is another and more stringent test. The β and DR values for chromophore **1a** are presented in Table 8.3 and show almost no difference when going from the DFT-optimized geometry to the geometry obtained with the re-parameterized GAFF. The DRs are identical using both methods and geometries and β_{HRS} varies by less than 0.3 % when using the TDDFT/M06-2X method. This confirms the validity of the re-parameterized GAFF for our purpose.

	QM geometry		MM geometry	
Method for calculating the β responses	β_{HRS}	DR	β_{HRS}	DR
TDHF	20.5	4.87	20.5	4.87
TDDFT/M06-2X	86.4	4.98	86.6	4.98

Table 8.3 – TDHF and TDDFT/M06-2X β_{HRS} (in 10^3 a.u.) ($\lambda = 1064$ nm) and DR values for chromophore **1a** in gas phase computed using geometries optimized at the DFT/M06-2X and MM/re-parameterized GAFF levels.

8.1.2   Simple Point Charge for Flexible Water (SPC/Fw)

To test the validity of the FF to be used for the water molecules, a MD simulation was performed with the SPC/Fw[87] FF for a box containing only 1000 water molecules (T = 300 K and P = 1 atm). At the end of the simulation, two parameters were checked, the radial distribution function (RDF) and the density. The RDF (or pair correlation function), g(r), describes how the density varies as a function of distance from a reference particle. Considering a homogeneous distribution of the atoms/molecules in space, the RDF represents the probability to find an atom in a shell of thickness dr at the distance r of another atom chosen as a reference point (Figure 8.4a).
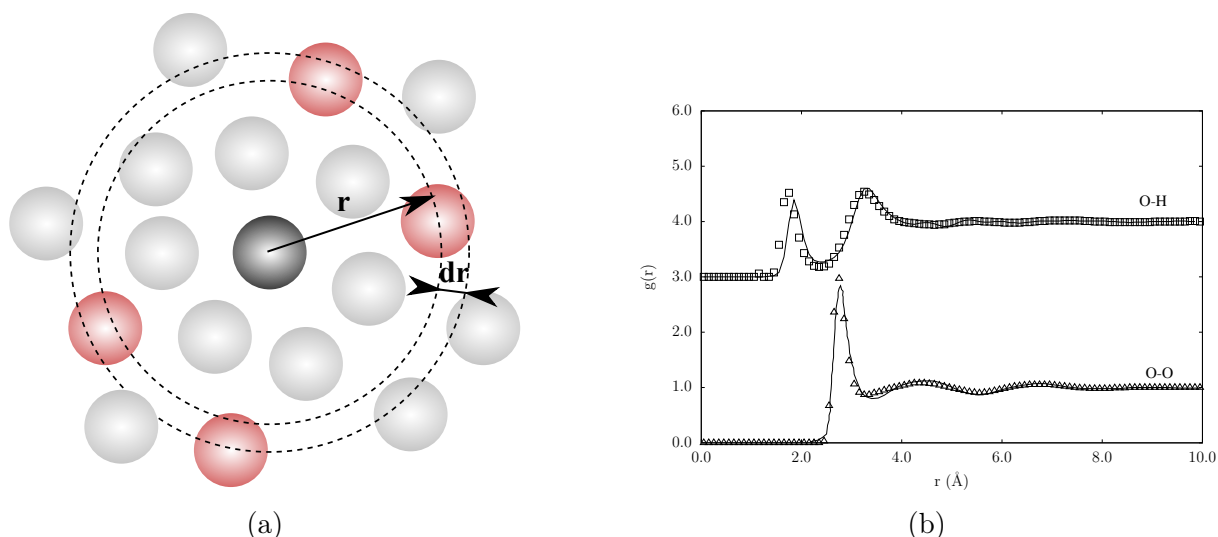

<center>(a)   (b)</center>

Figure 8.4 – **(a)** Space discretization for the evaluation of the radial distribution function; **(b)** experimental [line][112][113] and calculated O-O [triangles], and O-H [squares] radial distribution functions of water. For visibility, the O-H RDF is shifted by 3 units along the y axis.

As shown in Figure 8.4b, the calculated RDFs using the SPC/Fw FF compare well to experimental X-ray scattering data.[112,113] The RDF between oxygen atoms is equal to zero until 2.33 Å according to X-ray scattering experiments and until 2.4 Å according to the SPC/Fw results. Then, the peak at 2.75 Å (X-ray scattering) and 2.8 Å (SPC/Fw) represents the first shell of solvation. The integration of the area under the peak gives the coordination number, which is between 4 and 5 experimentally.[114] At larger distances, the RDF tends to one because the distribution is normalized. The calculated O-H RDF is also in good agreement with the experimental data. However, the calculated RDF is slightly shifted toward smaller distances. Meaning that the oxygen and hydrogen atoms are closer together using our model. This is confirmed when looking at the density value of $1.06\,\mathrm{g\,cm^{-3}}$ obtained at the end of the simulation, which is slightly larger than the

<center>65</center>

experimental density of liquid water in the same P and T conditions $(1.00\,\text{g}\,\text{cm}^{-3})$.[115] This larger density has been attributed to this flexible FF, which apparently induces a slightly denser packing of the molecules, as it can be seen in the first hydration shell, which is slightly more densely packed in the SPC/Fw case than experimentally. Although it produces a larger density compared to the other FF in the SPC or TIP3P series, SPC/Fw allows for a better description of the dielectric and self-diffusion constant, without sacrificing the well-reproduced properties of existing water models. Furthermore, these improvements were achieved without adding extra sites.[78,87] The SPC/Fw FF is therefore validated for the next step.

8.1.3   Calculation of the first hyperpolarizability using QM and MM approaches

At this stage, we are ready to perform the calculation of β of chromophore **1a** by accounting for explicit solvation as well as for its dynamical behavior. First, the MD simulation was carried out for chromophore **1a** surrounded by 4500 molecules of water, combining the SPC/Fw[87] FF for water with the re-parameterized GAFF[88] for the chromophore. These provide the snapshots for the β calculations at the QM level. Eventually, these β values were calculated for the structures extracted from 50 uncorrelated snapshots (every 0.2 ns). These contain the chromophore **1a** and a subset of water molecules located within a 10 Å distance of the nitrogen atom of the pyridinium. These calculations were performed at the TDDFT/M06-2X/6-311+G* level for a 1064 nm wavelength. Besides the explicit solvent effects described by the water molecules surrounding the pyridinium, the remaining solvent effects were included by using IEFPCM.[69–71]

The time evolution of the β_{HRS} values is shown in Figure 8.5 [blue], together with its cumulative average. Though this average is rapidly converging, the individual values change with time, showing the effects of structural fluctuations on β_{HRS}. The average β_{HRS} with its standard deviation calculated over the 50 snapshots amounts to 124.4 10^3 ± 39.4 10^3 a.u.. This corresponds to 65 % more than the β response obtained without explicit water molecules and without structural/geometrical fluctuations (75.6 10^3 a.u.). Of course, this value computed from the 50 snapshots includes the β_{HRS} contribution from the water molecules, but the latter is negligible.[116] Though measuring the first hyperpolarizability of water is not an easy thing to do, to give an idea, the first hyperpolarizability of one molecule of water evaluated at the TDDFT/M06-2X/cc-pVTZ

is around 15 a.u., i.e. several orders of magnitude smaller than for chromophore **1a**. As shown in Figure 8.5, the first hyperpolarizability calculations performed on the same 50 snapshots but using only the implicit solvation [black] give nearly exactly the same average as the previous one [blue]. Indeed, the average β_{HRS} with its standard deviation is 125.2 10^3 ± 39.7 10^3 a.u.. This demonstrates the fact that, in this case, the explicit water molecules included in the TDDFT calculations are not the determinant factor responsible for the difference of NLO responses between the static picture (with QM-optimized geometries) and the dynamic one (with geometries obtained from MD after re-parameterizing the FF).
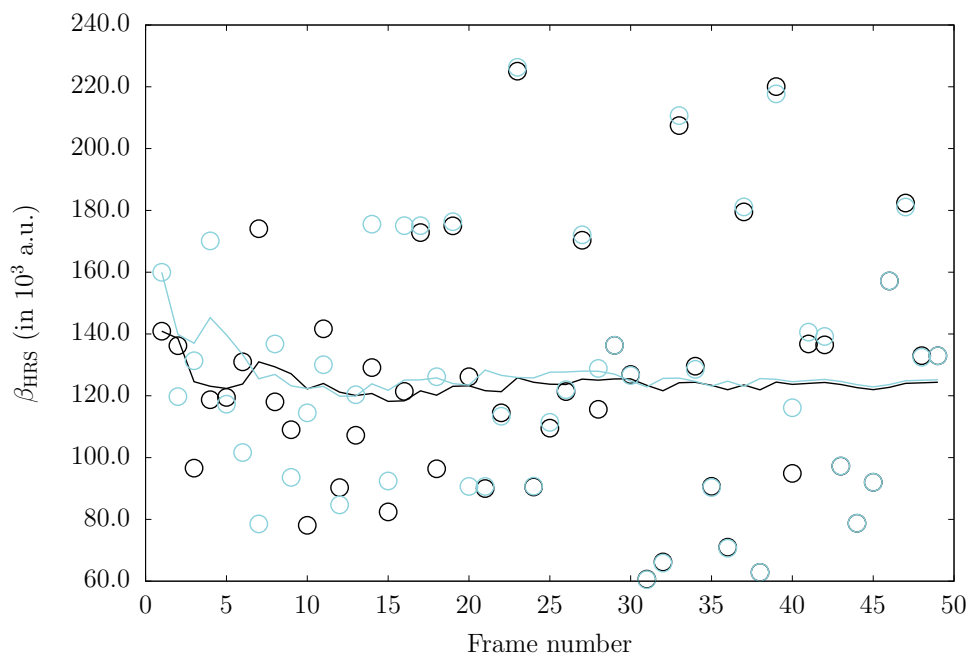

Figure 8.5 – Time evolution of TDDFT/M06-2X/IEFPCM ($\lambda = 1064\,\text{nm}$) β_{HRS} (in 10^3 a.u.) [circles] and its cumulative average [line] for **i)** chromophore **1a** surrounded by selected explicit water molecules and implicit solvation [blue] **ii)** the same chromophore with only implicit solvation [black].

Statistical analysis performed on the 50 snapshot geometries highlights the variations of geometry among the snapshots. The average BLA and standard deviation value amounts to 0.10 ± 0.03 Å. This is not in contradiction with the DFT value of 0.12 Å. The BLA values are spread across a wide range (Figure 8.6a) and, since β was demonstrated to be sensitive to the geometry, this has a natural impact on β. Indeed, when looking closely at the individual variations of BLA from one frame to another, the extreme values of β_{HRS} can be explained. For example, frames 7, 19, and 33 display a NLO response above average and an extremely low BLA (0.06 Å, 0.05 Å and

0.04 Å, respectively). On the contrary, frames 36 and 38 exhibit a β_{HRS} below average and larger BLA values (0.16 Å and 0.14 Å, respectively). This is consistent with the analysis made in Chapter 7, where compounds with large NLO responses were characterized with small BLA values. The frames number displaying a value outside the standard deviation range are specified on each graph in Figure 8.7a.

The conformation of the snapshots was also investigated by the means of three dihedral angles (previously defined during the re-parameterization of the GAFF). The dihedral angles are less spread and are mainly in the 170°- 180° range (Figure 8.6b). Still, θ_1, θ_2 and θ_3 averages calculated over the 50 snapshots amount approximately to 170 ± 6.00°, in comparison to the 180° obtained for all three dihedral angles for the DFT calculations (Table 8.4). The correlation between the β_{HRS} and the dihedral angles is less straightforward than for the BLA values. Nevertheless, an analysis is still possible. For instance, frames 23 and 39 demonstrate large NLO responses and small θ_1 of 157.32° and 152.65°, respectively. The trend is inverted for θ_3 as frames 17 and 39 with large β_{HRS} possess larger value of θ_3 (178.36° and 176.92° respectively). Continuing along the same lines, frames 31, 38, and 44 display below average β_{HRS} and below average value of θ_3. For the second dihedral angle, both trends are observed. Once again, the frames number displaying a value outside the "one standard deviation" range, for θ_1, θ_2, and θ_3, are specified on each graph in Figures 8.7b, 8.7c and 8.7d, respectively.
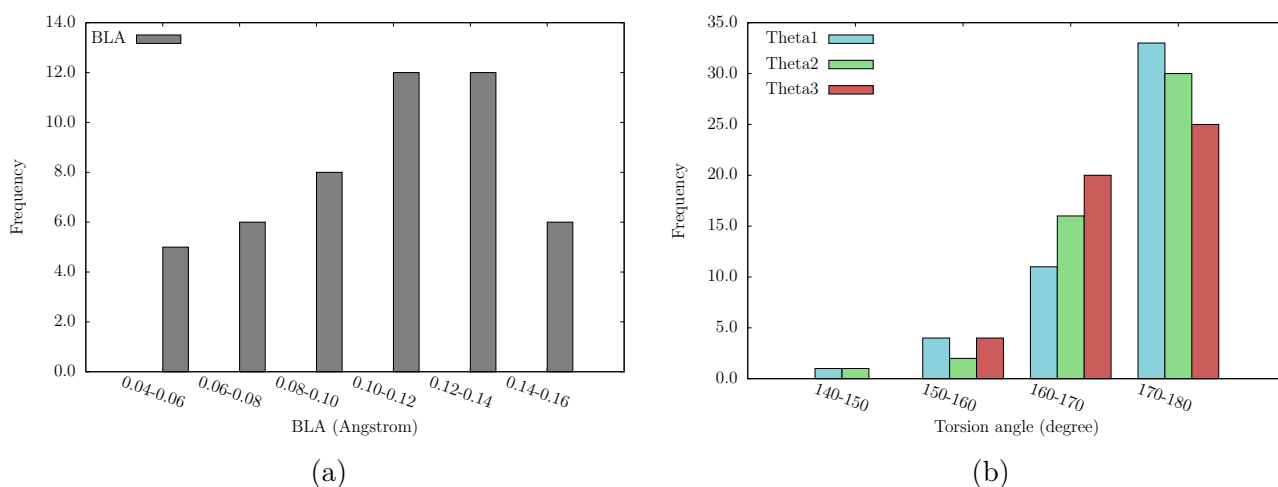

(a)   (b)

Figure 8.6 – Statistical analysis performed on the 50 snapshots geometries **(a)** dispersion of the BLA values, and **(b)** dispersion of the three dihedral angles values.

	BLA	θ_1	θ_2	θ_3
QM	0.12	180	180	180
Average MM	0.10 ± 0.03	170.93 ± 7.56	170.97 ± 6.57	169.25 ± 6.24

Table 8.4 – Comparison of BLA (in Å) and dihedral angles (in °) values between the QM/M06-2X and the 50 MM/re-parameterized GAFF snapshots geometries.

Globally, we can mostly say that some extreme β_{HRS} values are consistent with extreme BLA and/or dihedral angle value(s). Nevertheless, as shown in Figure 8.8, a one-to-one correlation was not found between β_{HRS} and any of the structural parameters studied. Both geometrical parameters can obviously reinforce or weaken the effect of the other, leading to such variations of β_{HRS}. There results have highlighted the impact of the flexibility of the chromophore structure on its first hyperpolarizability, exhibiting an increase by about 65% with respect to the DFT ground state geometry. Analysis of the results at the light of the geometrical parameters shows that there is no dominant factor but rather collective effects associated with the BLA and dihedral angles.
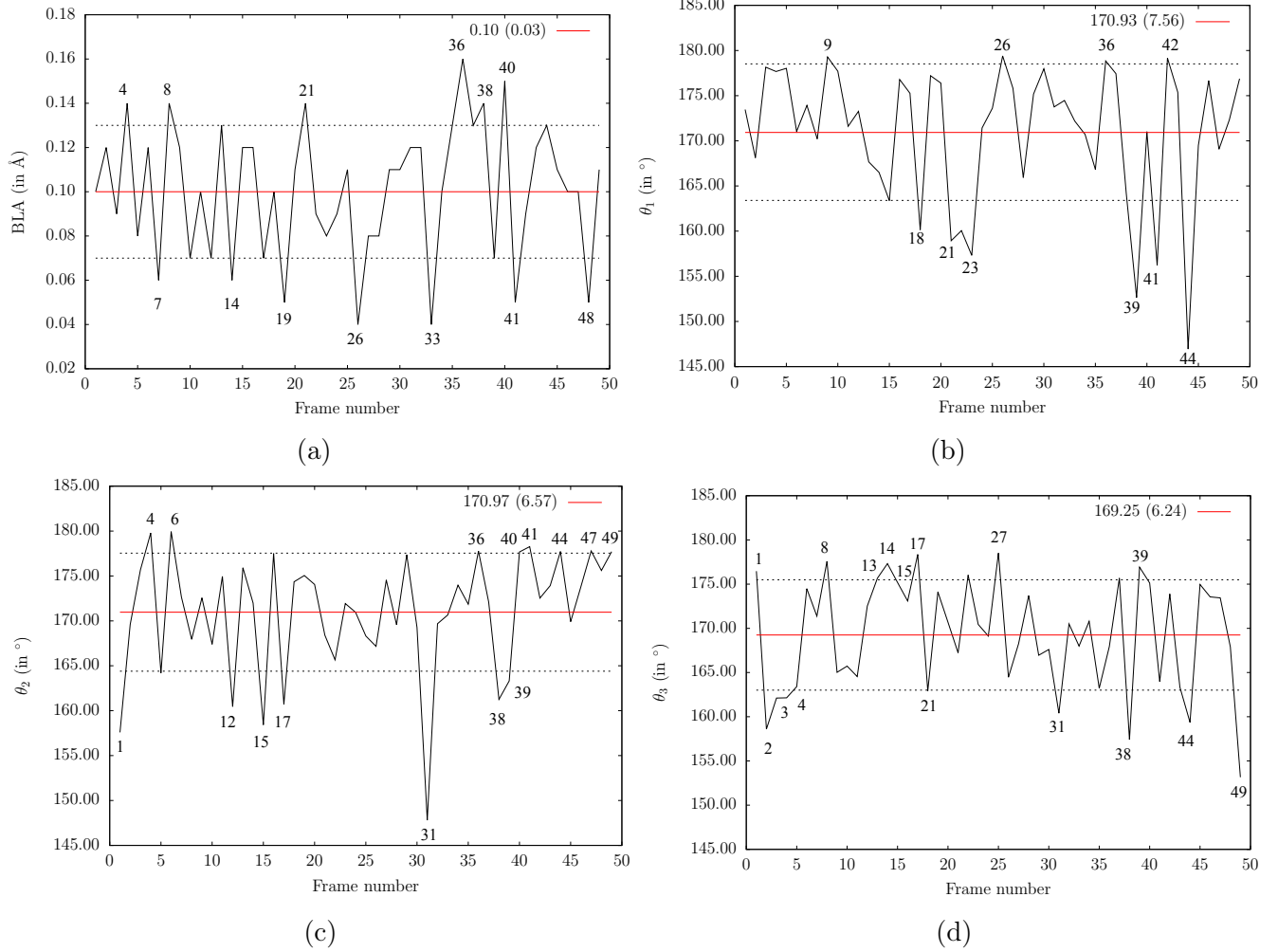
Figure 8.7 – Evolution of **(a)** the BLA; **(b)** θ_1; **(c)** θ_2, and **(d)** θ_3 over the 50 snapshots, as well as their average values [red line] and standard deviations [dashed lines]. The frames number displaying a value outside the "one standard deviation" range are specified on each graph.
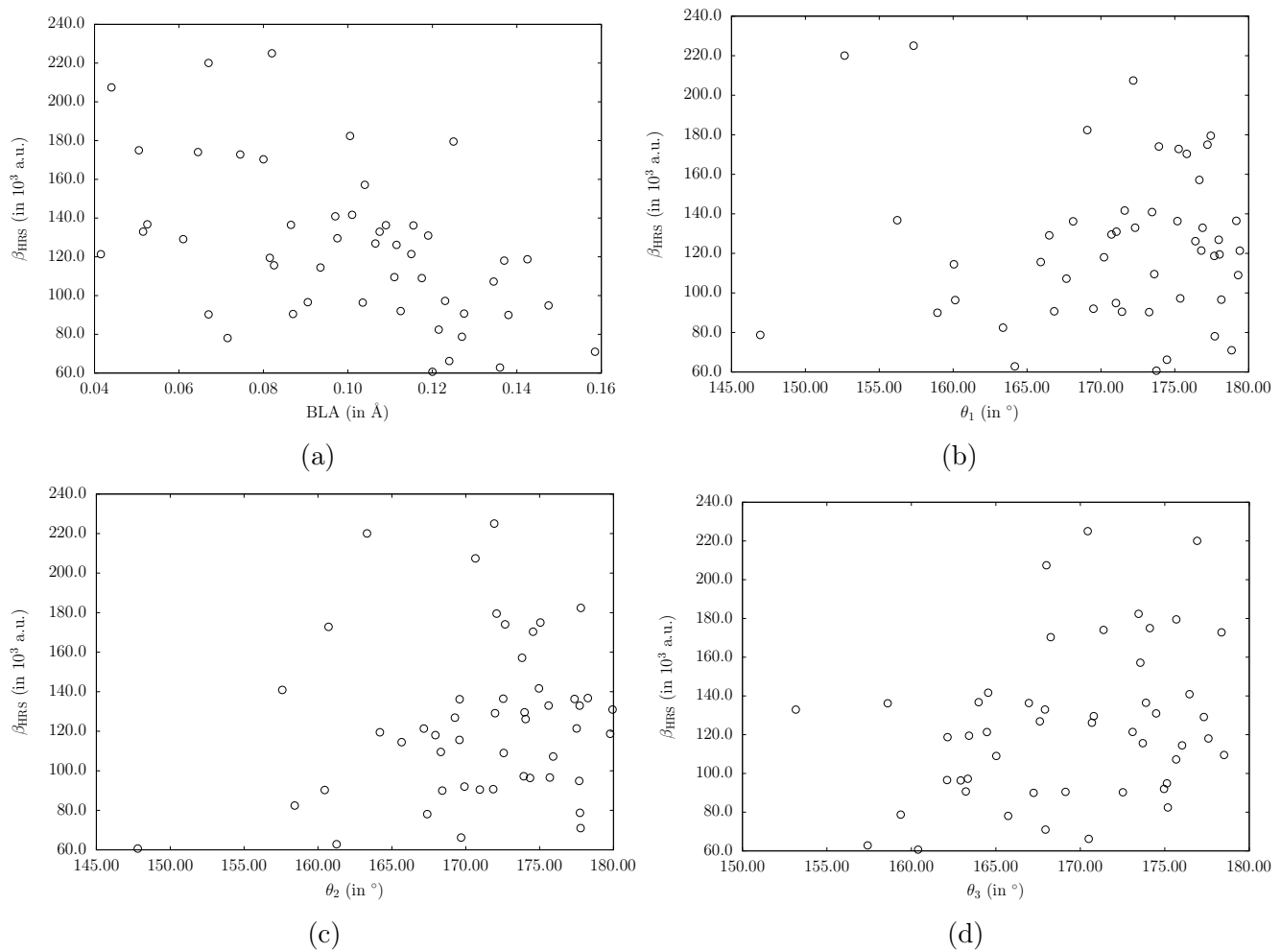
(a)

(b)

(c)

(d)

Figure 8.8 – Correlation between the β_{HRS} values and **(a)** the BLA values; **(b)** θ_1; **(c)** θ_2, and **(d)** θ_3.

8.2   Chromophore embedded in a lipid bilayer

As discussed in Subsection 8.1.1, the validity of SPC/Fw for water molecules and of GAFF for the dye has already been addressed and confirmed. Now, this Subsection focuses on the reliability of the series of the CHARMM FFs (successively CHARMM22, CHARMM27 and CHARMM36), and particularly CHARMM36 lipid[98,108] FF for lipid molecules. This verification was less thorough, because the lipid bilayer only provides the structure of the environment. Indeed, we are not interested here in computing the NLO response of the surroundings -it is negligible with respect to the dye response-, but rather in the influence of the milieu on the NLO response of the embedded chromophore. Nevertheless, the variations in bond lengths between the DFT/M06-2X/cc-pVTZ-optimized geometry (QM geometry) and the FF/CHARMM36-optimized geometry (MM geometry) were compared. On average, bond lengths differ by $0.007\,\text{Å}$ with maximum values of $0.03\,\text{Å}$ for carbon-carbon bonds of the long and flexible alkyl chains, which is acceptable for our purpose. These good results were expected since the FFs of this series were developped and optimized to reproduce experimental data for non-, mono- and polyunsaturated lipids.[117] This validates the structure of one isolated DPPC. The next Subsection focuses on analyzing the global structure of the bilayer composed of 125 DPPCs and chromophore **1a**.

### 8.2.1   Validity of the bilayer simulation against experimental data

In this Subsection, we are interested in validating the structure of the simulated DPPC bilayer. In order to do that, different structural parameters are confronted with experimental data. As a reminder, Figure 8.9 presents the structure of the DPPC phospholipid and chromophore **1a**. In addition, it also defines the atom labels of the skeleton. These will be used in some of the following analyses.

Analysis of the MD trajectories

The MD trajectories were analyzed by calculating, successively, the root-mean-square deviation (RMSD) of the positions of **1a** extracted from the membrane, and of the 125 lipids (Figure 8.10). The RMSD gives the measure of the average motion of the molecule from one frame to the next. The averaging is performed over the n pairs of equivalent atoms, and d_i is the distance between the two atoms of the ith pair, as mentioned in Equation 8.1.
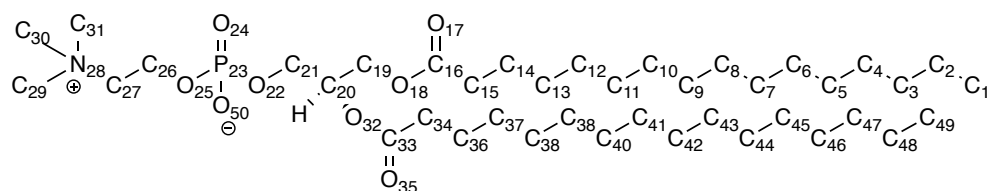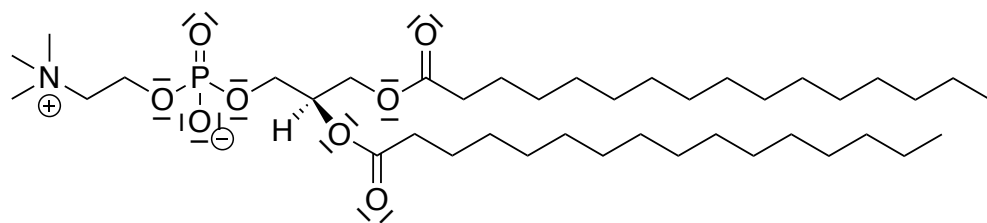
(a)
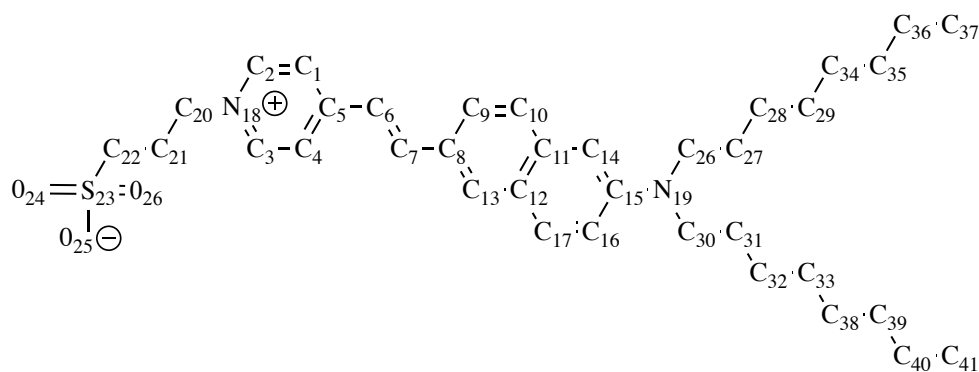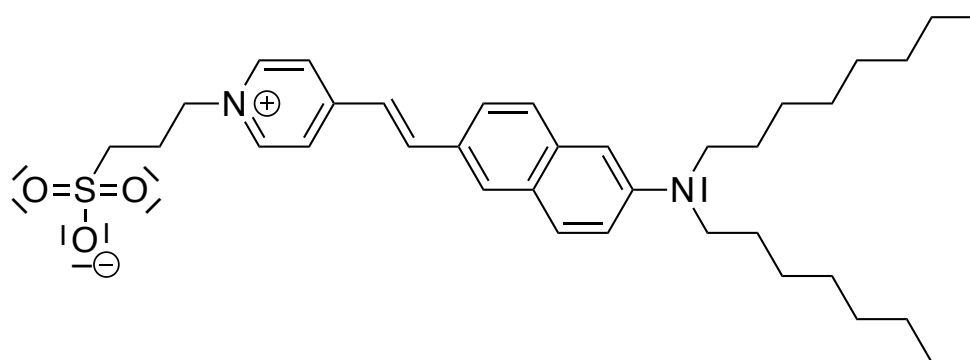
(b)

Figure 8.9 – Topologic structures and atom labels of **(a)** DPPC, and **(b)** chromophore **1a**.

$$RSMD = \sqrt{\frac{1}{n}\sum_{i=1}^{n} d_i^2} \tag{8.1}$$

The more the RMSD is constant, the more the molecule/system is equilibrated. This is a valuable information, because no method exists to prove that a simulation has converged. Unless RMSD has reached a stationary shape, the simulation has not yet converged. The slight fluctuations in the chromophore RMSD ($1.4 \pm 0.3\,\text{Å}$) demonstrate that the chromophore is mostly stable in the membrane. Indeed the displacement is small compared to the bilayer dimensions (i.e. approximately 50 Å x 50 Å x 80 Å). For the lipid molecules, the RMSD is less constant and presents some peak values around 20 ns, 56 ns, 86 ns and 210 ns.
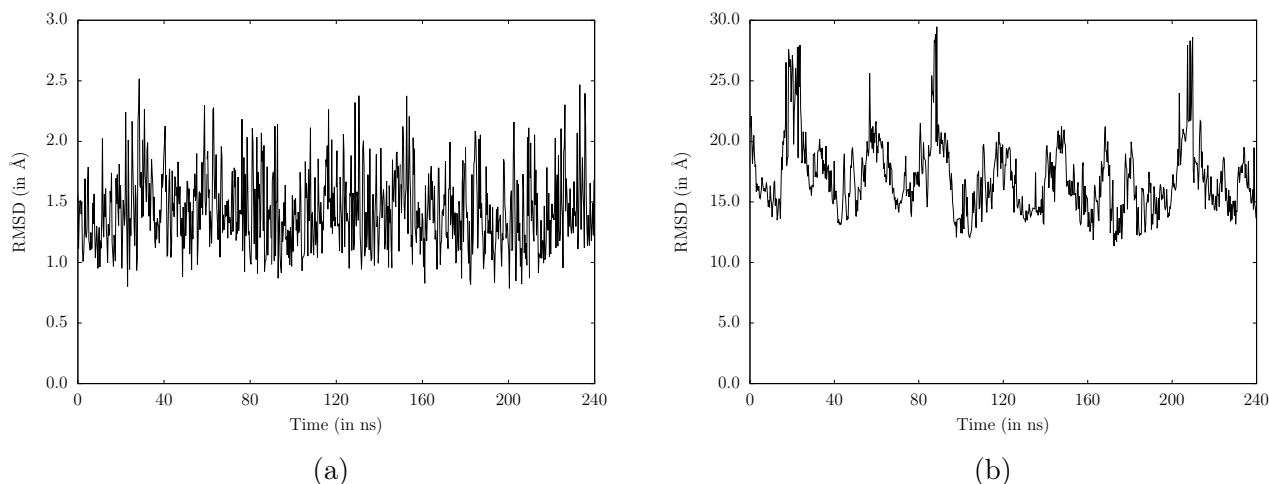

Figure 8.10 – RSMD computed over the production phase for **(a)** chromophore **1a** extracted from the membrane, and **(b)** the entire lipid part of the bilayer.

Average area per lipid

The average area per lipid ($\langle A \rangle$) is a fundamental parameter to describe the membrane structure. It contains information regarding the phase, the fluidity, and the degree of condensation. $\langle A \rangle$ can also be used as criteria to identify the equilibration state and it can be compared to experimental data from X-ray diffraction and nuclear magnetic resonance (NMR) experiments. Because of the uncertainty in determining the relevant water/lipid ratio as well as of different data interpretation, experimenters have found a wide range of $\langle A \rangle$ values going from $\sim 57\,\text{Å}^2$ to $\sim 71\,\text{Å}^2$. From diffraction experiments, value for $\langle A \rangle$ of $66.3\,\text{Å}^2$,[106] $57.6\,\text{Å}^2$,[105] $70.9\,\text{Å}^2$,[118] and $66.5\,\text{Å}^2$ [119] have been reported for fully hydrated DPPC in the L_α phase. From NMR experiments,

values of $58.6\,\text{Å}^2$,[120] $56.0\,\text{Å}^2$,[121] $69.0\,\text{Å}^2$,[122] and $71.7\,\text{Å}^2$[123] have been found. The area per lipid of our simulated bilayer, as computed in the production phase, gives values of $56.3 \pm 0.1\,\text{Å}^2$ for the leaflet with the 125 DPPCs and chromophore **1a**, and of $59.0 \pm 0.1\,\text{Å}^2$ for the leaflet without the chromophore. Indeed, in our simulation, only one leaflet in stained. Globally, a value of $57.6 \pm 0.0\,\text{Å}^2$ is found for $\langle A \rangle$ for the entire system, which is in the range predicted experimentally. Considering the various factors that may influence the value (i.e. the FF, simulation length, bilayer size, and water/lipid ratio),[28] and the fact that typically larger $\langle A \rangle$ are found in experiments than in simulations, our bilayer reproduces well experimental data.

Membrane thickness

The membrane thickness is a property that depends on the alkyl chain length of its lipid components, the tilt angle (see below) and the degree of unsaturation of the lipids within the membrane. The membrane thickness is often measured by the so-called "phosphate-to-phosphate" distance.
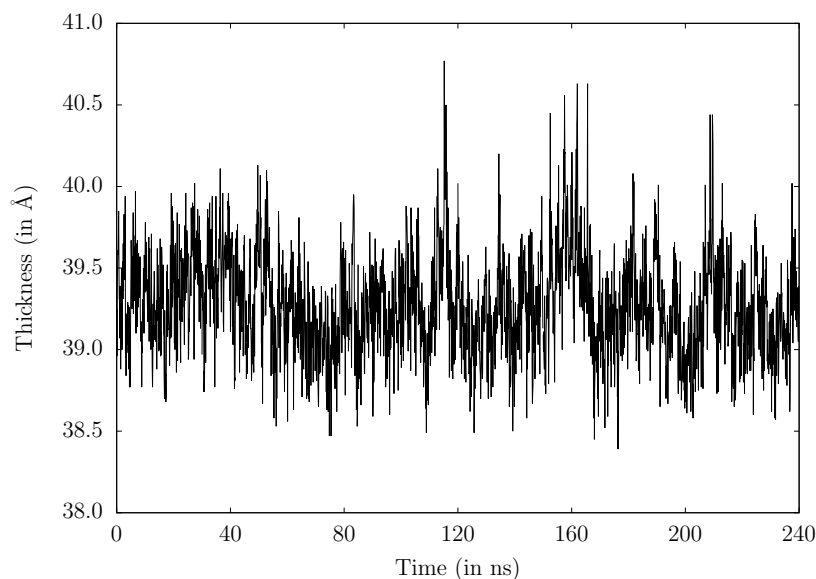
Figure 8.11 – Membrane thickness calculated from the P-P distance as a function of the simulated time.

The bilayer thickness is plotted in Figure 8.11 as a function of the simulation time. The averaged P-P distance between the phosphorous atoms in the two bilayer leaflets gives a value of $39.3 \pm 0.3\,\text{Å}$. This value is in very good agreement with the experiemental value of $37.5\,\text{Å}$[119] found by X-ray experiments. This is also comparable to values obtained from MD simulations

of DPPC bilayers under similar conditions: $36.0\,\text{Å}$[78] and $40.0\,\text{Å}$.[124] Small variations can indeed occur owing to differences in the treatment of the electrostatics, the charge definition, and the water/lipid ratio.[28]

Tilt angle

A tilt angle is defined as the angle between a selected vector, often defined by a pair of atoms within the molecule, and the lipid bilayer normal (Z-axis). For membranes, several lipid vectors have proven to be very informative because they reflect its physical properties and because they can often be estimated by experimental techniques. The tilt angle of chromophore **1a** was also analyzed.

(a)   (b)   (c)
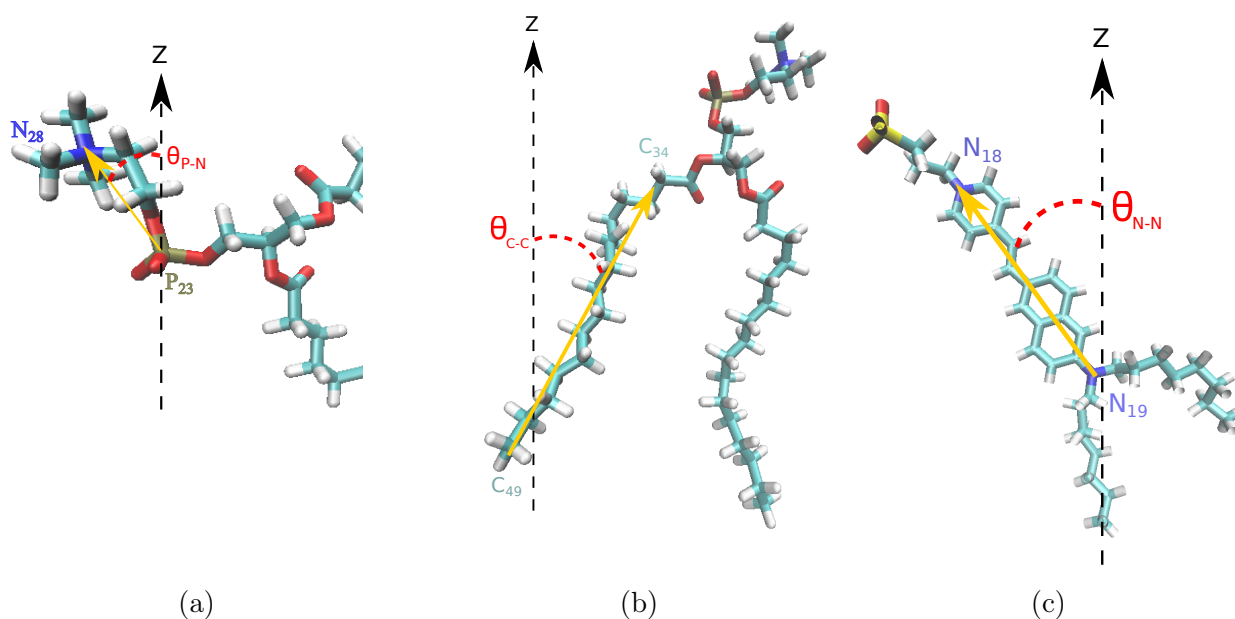
Figure 8.12 – Definition of the **(a)** P-N lipid tilt angle; **(b)** C-C lipid tilt angle, and **(c)** N-N **1a** tilt angle.

The first vector was defined between the phosphate group (P_{23}) and the nitrogen atom (N_{28}) of the choline group in the head region of the DPPC. This P-N angle, θ_{P-N}, is shown in Figure 8.12a and its evolution, calculated over the production step for the 125 DPPCs, is plotted in Figure 8.13a. An average value of $106.6 \pm 1.4°$ is obtained. This large angle allows for favorable interactions between the glycerol moieties and the water layer. The magnitude of the tilt angle is indeed controlled by the balance between the need for efficient hydrocarbon chain packing and the

hydrophilic character of the polar head group.[125]

Figure 8.13 – Time evolution of the **(a)** averaged P-N lipid angle; **(b)** averaged C-C lipid angle, and **(c)** N-N **1a** angle.

We can also calculate the tilt angle of the lipid alkyl chains. In order to do that, a vector extending over the entire alkyl chain was defined (atoms $C_{34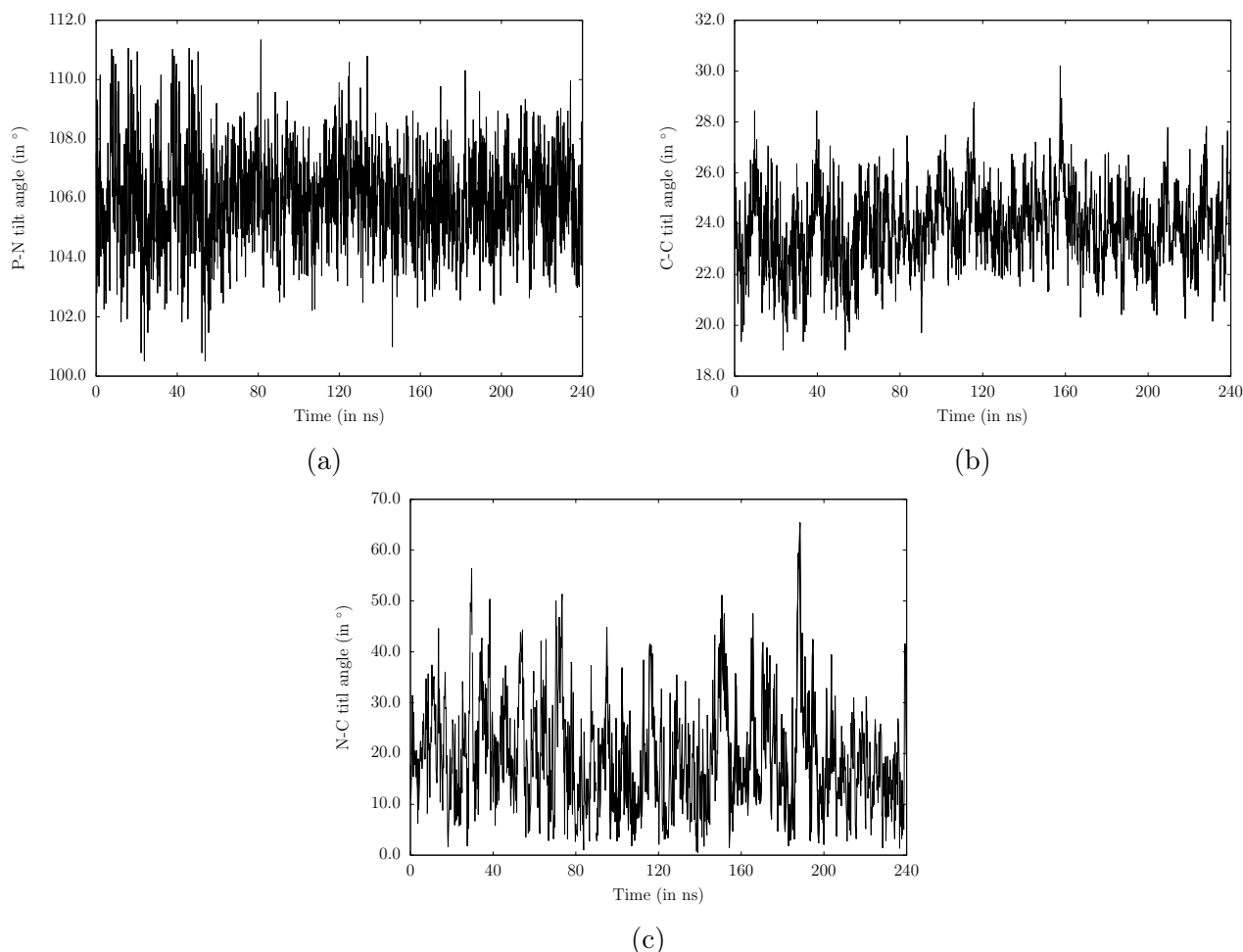}$ to C_{49}, as specified in Figure 8.9a) and sketched in Figure 8.12b. In the case of the C-C tilt angle, θ_{C-C}, various values have been reported: using X-ray diffraction, Chapman et al[125] found a value of 32°. Using the same technique, θ_{C-C} values of 17° at $c = m_{H_2O}/(m_{H_2O}+m_{DPPC}) = 0.94$ and 33° at $c = 0.75$[126] have been reported. Also depending on the degree of hydration of the bilayer, Levine[127,128] obtained values of 0° and 28° for a bilayer for which $c = 0.02$ and $c = 0.48$, respectively. Electron diffraction experiments by Hui[129] provided values of 0° and 16° for a non- and a fully-hydrated bilayer, respectively. It has also been demonstrated that the tilt angle depends on the temperature. DPPC bilayers have been described with lipid tilt angles of 35° at 5 °C and 30° at 40 °C.[130] In this study, on average, a value of $24.1 \pm 1.4°$ is found. The evolution the tilt of the chains (C-C angle) computed over

the production step is plotted in Figure 8.13b. As a reminder, our bilayer was simulated with a water concentration of c = 0.42 and at a temperature of 315.15 K. Considering all the parameters influencing this angle, the alkyl tilt angle value obtained is acceptable. For both angles, the standard deviations are small. This indicates that the DPPCs have globally the same shape and orientation throughout the bilayer and the simulated time. This can also be seen when looking at the shape of the plots presented in Figure 8.13: the angles oscillate around the average value, without extreme peaks.

Finally, a vector was defined within the chromophore (i.e. between the nitrogen atoms N_{18} and N_{19}, as defined in Figure 8.9b) as sketched in Figure 8.12c. Its evolution with time is plotted in Figure 8.13c. The average value of this N-N angle, or θ_{N-N}, with its standard deviation amounts to 19.3 $\pm$ 10.6°. This demonstrates that **1a** is not perfectly aligned with the bilayer normal. Furthermore, the large standard deviation indicates the chromophore tilt vary over time.

Density profiles and distribution of atom types

The time-averaged distributions of water molecules, nitrogen, phosphorous and selected carbon atoms are plotted in Figure 8.14. These highlight an inner region of about 25 Å containing the bulk water. Of course, this value depends on the number of water molecules included in the simulation. As mentioned in Subsecton 6.2.2, periodic boundary conditions are applied in all three dimensions, so that the simulation is actually that of a multilamellar system. As expected, water is not present in the zone of the hydrophobic fatty acids. Then, the water density rises at the water/lipid interface, where it reaches its maximum value of 0.99 g cm^{-3}. The water/lipid interface is usually defined as the region where the water concentration ranges between 10% and 90% of its maximum value. In such case, the interface is found to be 15 Å wide. Considering both interfaces, this value means that approximately 40% of the bilayer belongs to the interfacial region.

Figure 8.14 also presents the distribution of several atoms within the lipid (as defined in Figure 8.9a): N_{18} and P_{23} indicate the position of the polar headgroup, C_{20} is the central glycerol carbon, and C_{16} is the carbon of one of the carbonyl groups. Analysis of this Figure shows that the water molecules penetrate into the bilayer, to a depth that corresponds approximately to the position of the carbonyl group on C_{16}. This is consistent with neutron diffraction experiments.[131] By comparison, the distribution shown in Figure 8.14 resemble more the one obtained for the liquid-crystalline (L_α) phase than the gel (L_β) phase. Indeed, in the latter, the interface is remarkably
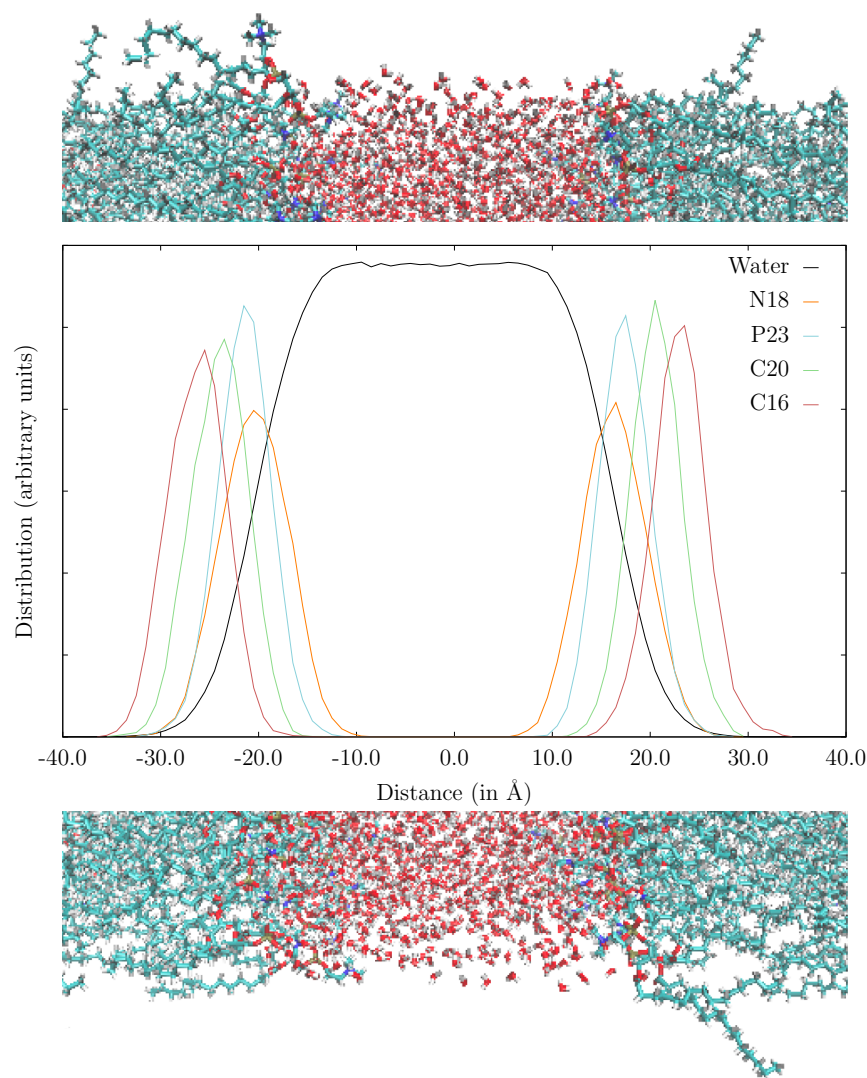
Figure 8.14 – Distribution along the bilayer normal of water molecules, nitrogen and phosphorous atoms. The middle of the bilayer corresponds to Z = ± 40, the middle of the water layer to Z = 0. Atom numbering refers to Figure 8.9a.

more diffuse and a more pronounced penetration of water occurs.[124]

At the interface, water molecules form hydrogen-bonds with the oxygen atoms of the lipids. One water molecule can either form H-bond with different oxygen atoms of one DPPC or with oxygens atoms of two DPPCs. These H-bonds result in water bridges and a huge H-Bond network at the interface.[132] Hydrogen bonds are defined according to geometric criteria: i) the distance between the donor, D, and the acceptor, A, is smaller than $3.0\,\text{Å}$ and ii) the D-H-A angle is larger than 150°. In these conditions, between 3 and 4 water molecules are hydrogen-bonded to one phospholipid. This is consistent with the study of Arnold et al.,[133] who found 5 water molecules per phospholipid. The water molecules hydrogen-bonded to the bilayer belong to the interfacial[134]

or bound[135] type. The latter includes water molecules in direct interaction with the lipids. On the contrary, the free water possess bulk-like properties. Between the two limiting cases, perturbed water corresponds to the water in the transition region whose properties are still influenced by the presence of the lipid membrane.[134] Even though several studies have focused on determining the number of water molecules in these different classes, it is difficult to define exact criteria to distinguish them. Still, to give an idea, Finer et al.[135] reported that about 12 water molecules per DPPC are influenced by the phospholipid surface. Furthermore, logically, the more the water molecules are buried, the longer the lifetime of the H-bonds. Along the same lines, MD simulations have shown that hydrogen bonds formed between water and the double bonded lipid oxygen (C=O) atoms last longer than those to single bonded lipid oxygen atoms (C-O).[136] Still, there is little experimental data on the hydrogen-bonding structure at the lipid/water interface.

Hydrocarbon chain order parameter

The hydrocarbon chain structure of the lipids is intimately linked to some structural properties of biological interest such as the bilayer condensation, the membrane fluidity, and the membrane thickness. One way to evaluate the hydrophobic tails arrangement consists in calculating the order parameter, which tensor, S, is defined as follows[78,124]:

$$S_{ij} = \frac{1}{2} \left\langle 3 \, cos\theta_i \, cos\theta_j - \delta_{ij} \right\rangle \tag{8.2}$$

where θ_i is the angle between the ith molecular axis and the bilayer normal. For the nth CH$_2$ unit, the molecular axes are defined as follows:

- z: vector from C_{n-1} to C_{n+1};
- y: vector perpendicular to z and in the plane defined by C_{n-1}, C_n, and C_{n+1};
- x vector perpendicular to z and y

To give an idea, a S_{zz} values of one indicates a full order along the z-axis, where S_{zz} = -1/2 the alkyl chains are fully ordered perpendicularly to the bilayer normal, and 0 corresponds to an isotropic distribution.[124]

Interestingly, chain conformations found by MD can be compared with NMR experiments on deuterated (DMR) DPPC. This method yields an order parameter S_{CD} (direction along the C-D bond) that can be directly related to the MD order parameter through the expression[78,124]:

$$- S_{CD} = \frac{2}{3} S_{xx} + \frac{1}{3} S_{yy} \tag{8.3}$$

Figure 8.15 presents the MD order parameter as well as DMR experiments[137,138] for the L_α phase. Globally, both curves have the same shapes: a plateau extending from the 4th to the 8th CH$_2$ groups and then a decrease towards the end of the tails, indicating no preferential orientation. Experimental values for $-S_{CD}$ over this plateau amounts to 0.20 ± 0.02.[138,139] They are in perfect agreement with the hydrocarbon chain order parameter value found in this simulation, which amounts to 0.22 ± 0.00. This value is also consistent with many simulation studies, which reported values for $-S_{CD}$ close to 0.2.[124,140,141]

Finally, our simulation results resemble more those found for the L_α than for the L_β phase. Indeed, spin label data,[142] as well as DMR data[143] on dimyristoylglycerophosphocholine (DMPC) suggest that the order parameter almost doubles when going from liquid-crystalline to the gel phase. The DMPC is a phospholipid, analogue to DPPC, for which the fatty acids are composed of 14 carbon atoms, as opposed to 16 for DPPC. Furthermore, a study of Egberts et al, on DPPC, found a plateau at approximately 0.35 for the L_β phase.[124] This substantiates the fact that our simulation deals with the L_α phase.
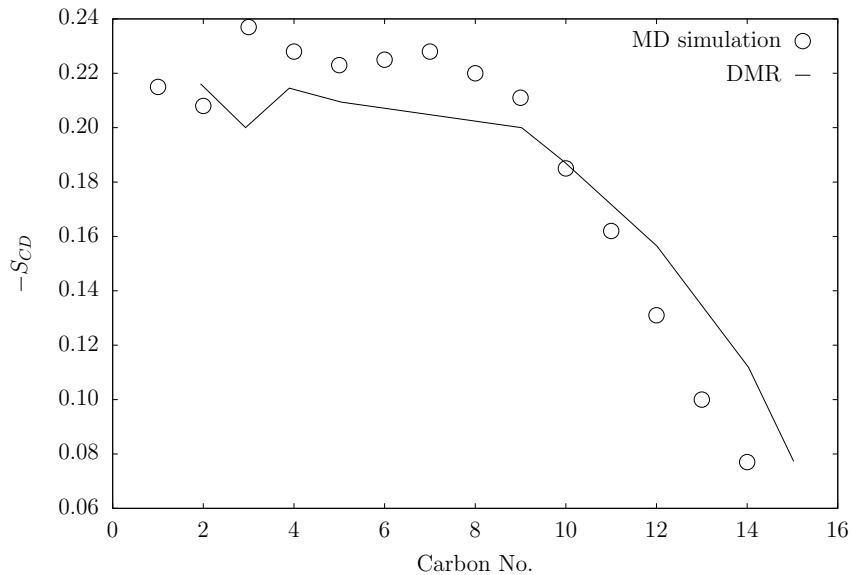

Figure 8.15 – MD order parameter [circles] calculated as well as DMR experiment [line][137,138] on the bilayer in the L_α phase. The x-axis corresponds to the length of the fatty acid: x = 0 corresponds to C$_{16}$, and x = 16 to C$_1$.

8.2.2   Calculation of the first hyperpolarizability of the chromophore using QM and MM approaches

As mentioned in Chapter 6.2.2, the MD simulation of chromophore **1a** embedded in a DPPC bilayer is performed, combining three different FFs: C36[98,108] FF for lipids, GAFF[88] for **1a**, and SPC/Fw[87] FF for water. Eventually, the β values were calculated for structures extracted from 120 uncorrelated snapshots (every 2 ns of the production run). These contain explicitly the coordinates of chromophore **1a** and its environment. The environment is represented using the ESP charges of the surrounding lipids. Each lipid possessing at least one atom in a 5 Å radius defined around every atom of **1a** was selected entirely. These β calculations were performed at the TDDFT/M06-2X/6-311+G* level for a 1064 nm wavelength. Additional surrounging effects were modeled as solvent effects by using the IEFPCM[69–71] scheme. We made sure that the lipid charges were included in the PCM cavity.
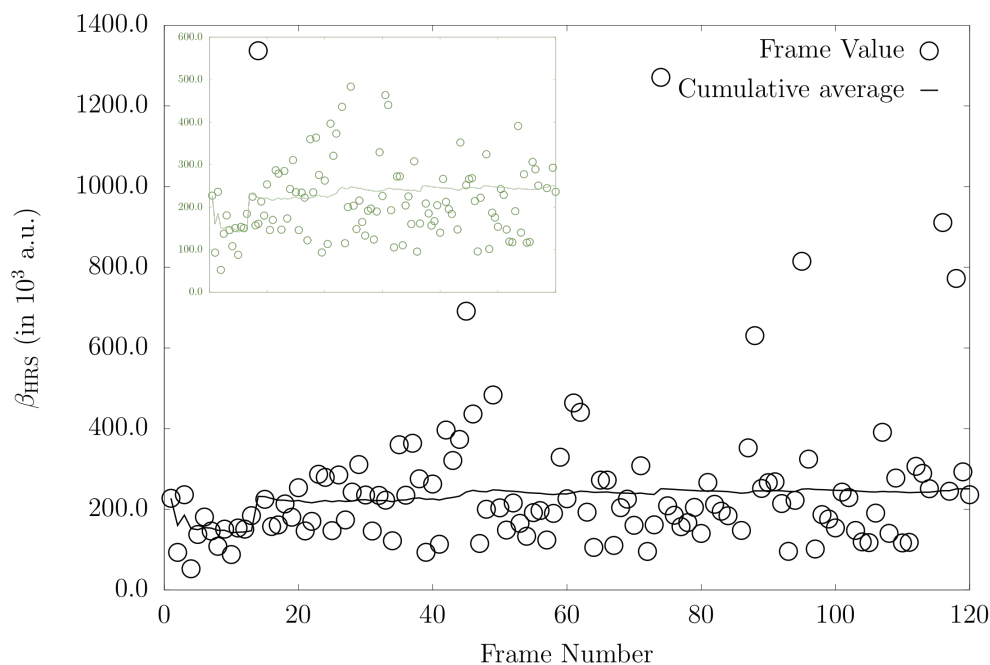
Figure 8.16 – Time evolution of TDDFT/M06-2X/IEFPCM β_{HRS} (in 10^3 a.u.) ($\lambda = 1064\,\mathrm{nm}$) [circles] and its cumulative average [line] for chromophore **1a** surrounded by lipid charges and implicit solvation [black] and zoom between 0.0 and 600.0 10^3 a.u. [green].

Figure 8.16 presents the time evolution of β_{HRS}, as well as of its cumulative average. Similarly to the simulation of **1a** in water, individual values vary strongly over time, even though the cumulative

average is quickly converging. The average β_{HRS} with its standard deviation calculated over the 120 snapshots amounts to 255.0 10^3 ± 197.8 10^3 a.u. [black]. First, this large standard deviation highlights the influence of the dynamical structural changes on the NLO responses. Moreover, in this case, it is amplified by the few extreme β_{HRS} values between 600.0 10^3 a.u. and 1400.0 10^3 a.u. (frames 14, 45, 74, 88, 95, 116 and 118). Note that, when excluding these frames, the average β_{HRS} and its standard deviation reduce to 213.2 10^3 ± 87.2 10^3 a.u.. These larger β_{HRS} responses are the consequence of resonant or near-resonant conditions. This is confirmed when looking at Figure 8.17, the visible absorption spectrum of these selected frames. The excitation energies were calculated using the same level of approximation employed for the β_{HRS} responses, i.e. the TDDFT/M06-2X/6-311+G* level by taking into account environmental effects using the lipid charges and the IEFPCM[69–71] scheme.
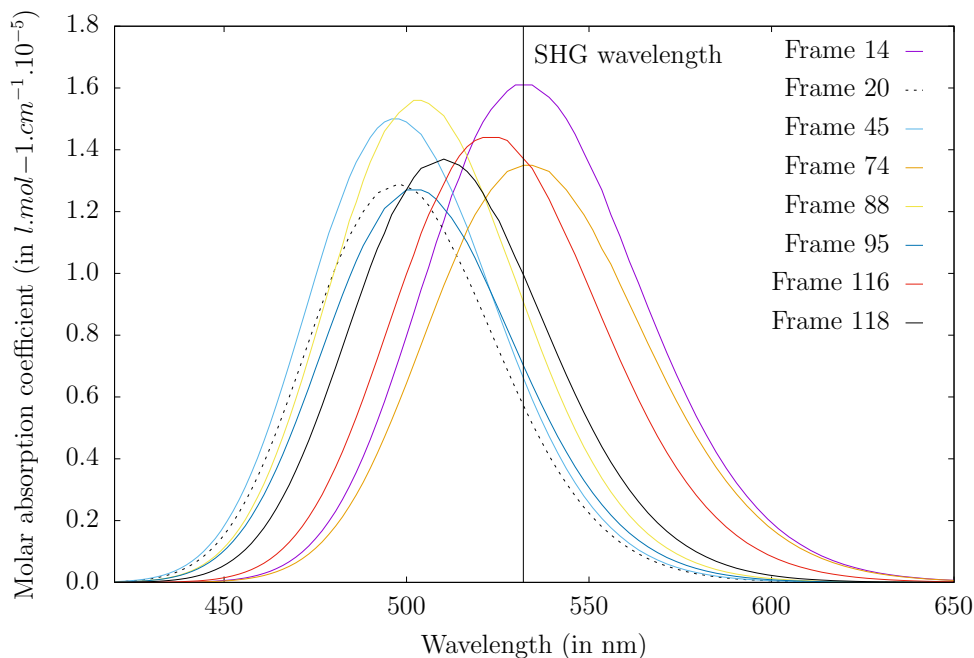
Figure 8.17 – Visible absorption spectrum of the frames presenting an extreme β_{HRS} value [plain lines]. The spectrum of frame 20 [dotted line], which displays a β_{HRS} response close to the average value, is also presented for comparison.

The more the excitation wavelength of the frame is close to 532 nm ($\lambda_{incident}/2$), the more it exhibits an intense NLO response. For example, frame 14 displays the largest β_{HRS} (1337.08 10^3 a.u.) and an excitation energy of exactly 532 nm. The remaining frames are in the near resonant region. For practical applications, it is interesting to have a large NLO response. However, within these resonant conditions, the advantage of the SHG is lost. Indeed, real states are excited

as opposed to interaction through virtual ones. As explained in Chapter 2, this can lead to photodamage. Experimentally, these resonant structures are inevitable. Fortunately, they are rare. In this study, this is only observed for a few frames.

As shown in Figure 8.18, no extremes values are present when considering the static β_{HRS}. This further confirms that the previously-selected frames were in near resonance or resonance when dealing with a 1064 nm wavelength. As a consequence, the standard deviation is much smaller than in the dynamic regime. Indeed, the average β_{HRS} and its standard deviation amounts to 32.26 10^3 ± 4.82 10^3 a.u.. Besides that, this Figure also highlights the fact that static β_{HRS} values are approximately one order of magnitude smaller (i.e. 10^4 a.u. instead of 10^5 a.u.) than those obtained at 1064 nm.
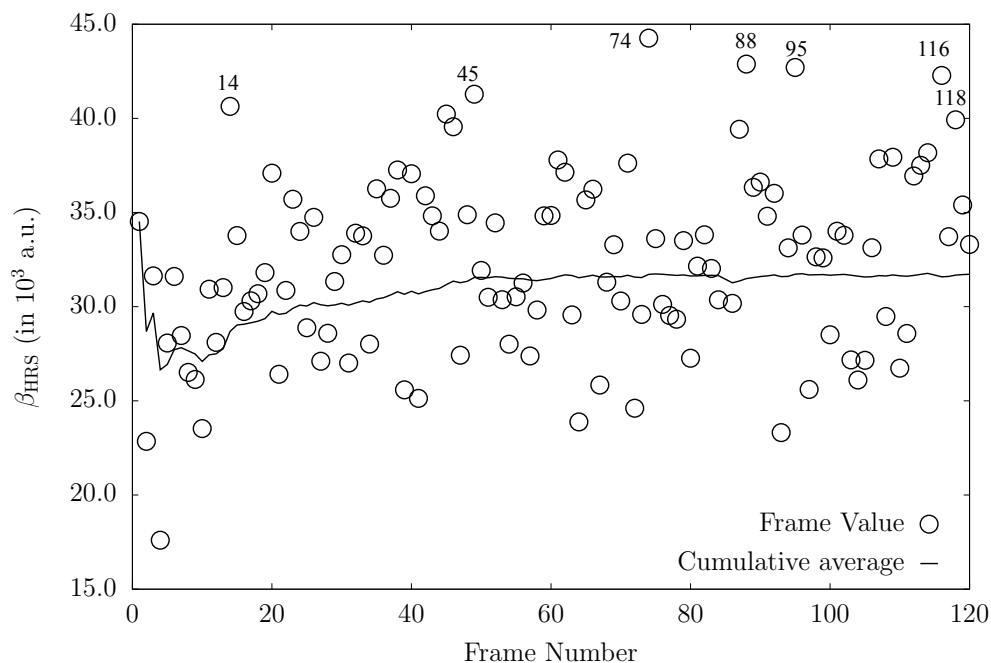
Figure 8.18 – Time evolution of TDDFT/M06-2X/IEFPCM β_{HRS} (in 10^3 a.u.) ($\lambda = \infty$) [circles] and its cumulative average [line] for chromophore **1a** surrounded by lipid charges and implicit solvation. The frames exhibiting a large dynamic β_{HRS} at 1064 nm are specified on the graph.

Note that the average DR at 1064 nm (4.99 ± 0.01) is consistent with that of a one-dimensional π-conjugated push-pull molecules. The small standard deviation indicates that it does not vary much during the simulation, i.e. by the dynamical nature of the system.

In order to find structure-property relationships, statistical analysis were performed considering

structural parameters such as the BLA and the dihedral angles, to try to explain the dispersion of the β_{HRS} values. Before going into details, Table 8.5 shows that the average values and standard deviations of the BLA values calculated over the 120 snapshots extracted from the bilayer MD simulation are similar to those obtained in the previous Chapter. This is particularly true for the dihedrals angles, for which the averages differ by less than 1° between the two sets of simulations.

	BLA	θ_1	θ_2	θ_3
QM	0.12	180	180	180
Average MM (in water)	0.10 ± 0.03	170.93 ± 7.56	170.97 ± 6.57	169.25 ± 6.24
Average MM (in bilayer)	0.06 ± 0.03	171.44 ± 7.36	170.75 ± 7.13	170.38 ± 6.24

Table 8.5 – BLA (in Å) and dihedral angles (in °) values as determined in different environments using different methods of calculation.

The average BLA and standard deviation value, of **1a** in the bilayer, amounts to 0.06 ± 0.03 Å. This value is clearly smaller than the one obtained for chromophore **1a** in the water environment. As explained in Section 7.3, a decrease of the BLA value goes hand-in-hand with an increase of the NLO response. This is consistent with the increase of β_{HRS} observed when considering the bilayer environment. When looking closely at the individual variations of BLA from one frame to another (Figure 8.19a), some extreme values of β_{HRS} can be explained. The frame numbers displaying particularly small or large BLA values are detailed on the graph and some of them can be linked to the extreme β_{HRS} values observed in Figure 8.16. Still, as shown in Figure 8.20a, which displays the variations of β_{HRS} with respect to the BLA values, there is no global correlation. Indeed, a correlation coefficient inferior to 0.03 is found. This shows that the BLA is not the only geometrical parameter determining β_{HRS}. The entire structure fluctuates, which is different from modifying one parameter at a time and rigidifying the rest of the molecule. Similar conclusions are drawn for the dihedral angles. Some extreme β_{HRS} values can again be explained by extreme θ_1 and/or θ_2 and/or θ_3 value(s). As for the BLA, interesting frame numbers are indicated on the graphs, as seen in Figures 8.19b, 8.19c, and 8.19d. Again the correlation coefficients are close to zero, indicating the absence of one-to-one correlation. Note that, the fluctuations of β_{HRS} can also be induced by variations of the lipid environment.

Another parameter influencing the NLO response are the alkyl chains conformations of **1a**. Indeed, for the DFT-optimized geometry, both alkyl chains are in all-trans conformation. Therefore,
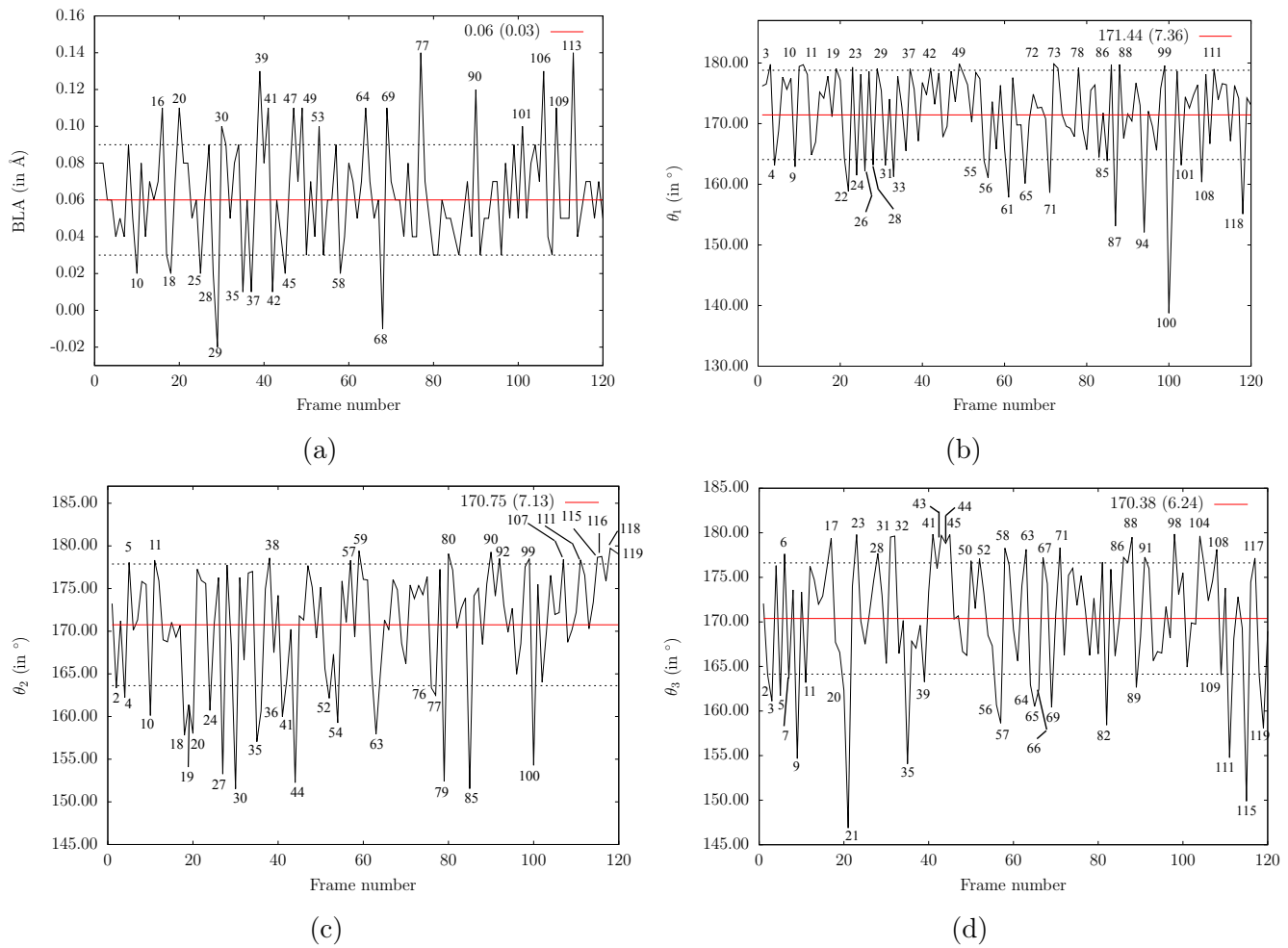
Figure 8.19 – Evolution of **(a)** the BLA; **(b)** θ_1; **(c)** θ_2, and **(d)** θ_3 over the 120 snapshots, as well as their average values [red line] and standard deviations [dashed lines]. The frames number displaying a value outside the "one standard deviation" range are specified on each graph.

there is centrosymmetry and no β_{HRS} response coming from these chains. When dealing with the structure extracted from the MD simulations, the structures are more flexible and dynamic. The conformational analysis of several snapshots shows that, most of the time, there is a lost of the all-trans conformation. As a consequence, the centrosymmetry is broken and so the alkyl chains can contribute (mildly) to the NLO response.
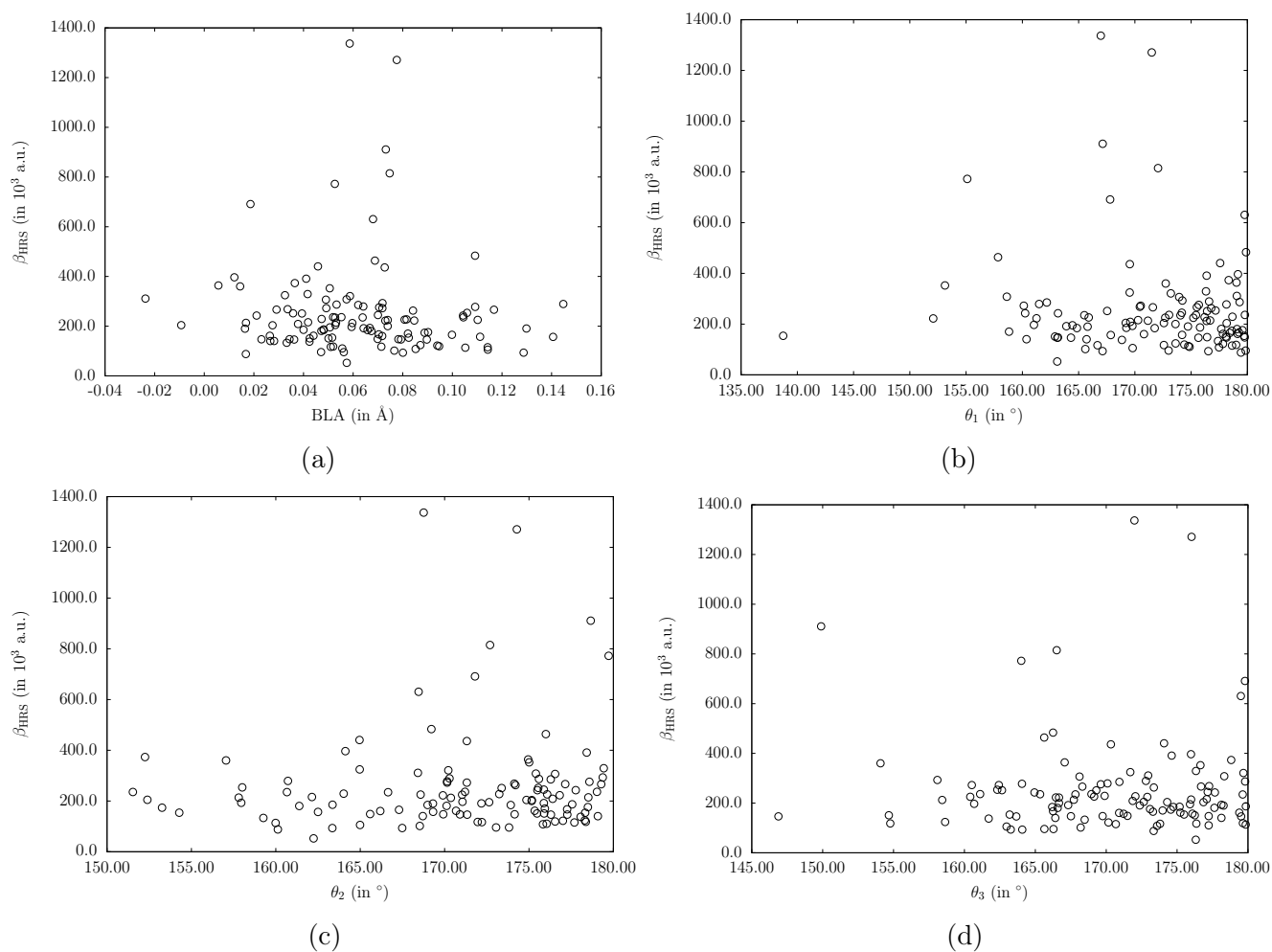
Figure 8.20 – Correlation between the β_{HRS} values and **(a)** the BLA values; **(b)** θ_1; **(c)** θ_2, and **(d)** θ_3.

8.3   Conclusions

These Chapters focused on calculating and then analyzing the NLO response of a dye in increasingly complex surroundings. These dyes and their environments were modeled by means of MD simulations. First, the FFs have been validated by confirming that bulk properties are reproduced, and, in particular, that they are able to reproduce the targeted structure and properties. For the water molecules, SPC/Fw FF has been selected and validated after a density and RDF check. For the di-8-ANEPPS chromophore, by using DFT results, GAFF had to be re-parameterized to better reproduce key structural parameters, which influence β_{HRS}. The Adaptative Biaising Force Method was used to refine the description of the dihedral angles energy terms on the basis of DFT rigid PESs. Amongst other changes, atom types were also added to modulate bond lengths in the aromatic rings. Finally, CHARMM36 FF has also been legitimized for the DPPC molecules. This has been achieved by considering the MD trajectories, the membrane thickness, the lipid tilt angles, the density profiles, and the chain order parameter. In all cases, good agreement has been observed with experimental data as well as related simulations from the literature.

Then, the static and dynamic β_{HRS} have been computed at the M06-2X/6-311+G* level and analyzed. In both the water environment and the lipid bilayer, the chomophore exhibits individual NLO responses spread over a wide range of values from one frame to another, even though the cumulative averages are quickly converging. This results in large standard deviations. The average β_{HRS} of chromophore **1a** and standard deviation amounts to 124.4 10^3 ± 39.4 10^3 a.u. in water and to 255.0 10^3 ± 197.8 10^3 a.u in the bilayer. These highlight the influence of the flexibility of the chromophore structure, accounted for using MD simulations. This can be further seen when analyzing two types of structural parameters, the BLA and the dihedral angles values, for which we observe a broad distribution. However it is not possible to establish one-to-one correlation between these parameters and the β_{HRS}. Indeed, the entire structure of the molecule fully fluctuates at each step. Finally, the dependence of the NLO response on its environment was confirmed, chromophore **1a** displaying, globally, the largest β_{HRS} when embedded in DPPC molecules. This is interesting for the use of these ANEP-like compounds to enhance the contrast in SHG experiments. Furthermore, the environmental-induced modulations of β_{HRS} can be used to highlight bilayer structural changes.

Part IV

General conclusions and perspectives

Chapter 9

General conclusions

In the context of biological imaging, this work aimed at bringing a better understanding of the second-order nonlinear optical responses of ANEP-like compounds. These are styryl amphiphilic dyes that can be classified as push-pull molecules. Indeed, they posses an electron acceptor moiety connected by a π-conjugated path to an electron donor moiety. These compounds are often used as Second Harmonic Generation (SHG) probes. The SHG phenomenon consists of the conversion of two incident photons of ω frequency into single photons of 2ω frequency when an intense and focused laser beam passes through an active medium. At the molecular level, this phenomenon is caused by the first hyperpolarizability, β. The β values reported in this work correspond to the quantities that can be obtained using the experimental hyper-Rayleigh scattering (HRS) method.

First, we focused on the β-structure relationships of ANEP-like compounds. This study was carried out at the quantum mechanics (QM) level in diluted gas phase, as well as by using implicit solvation to describe aqueous solutions. Secondly, we focused on analyzing the NLO responses of one molecule of the ANEP family, the di-8-ANEPPS, in increasingly complex environments. This has been achieved by using a two-step approach. First MD simulations were performed to investigate the dynamics and structure of the systems. Then, the chromophore NLO responses were evaluated at the QM level for selected snapshots extracted from the MD simulations. In these simulations, the chromophore was, successively, considered in water, and then inside a DPPC bilayer.

The key β_{HRS} and depolarization ratios (DR) values for the different environments are summarized below from the simplest "environment" (i.e. diluted gas phase) to the most complex one, the lipid bilayer :
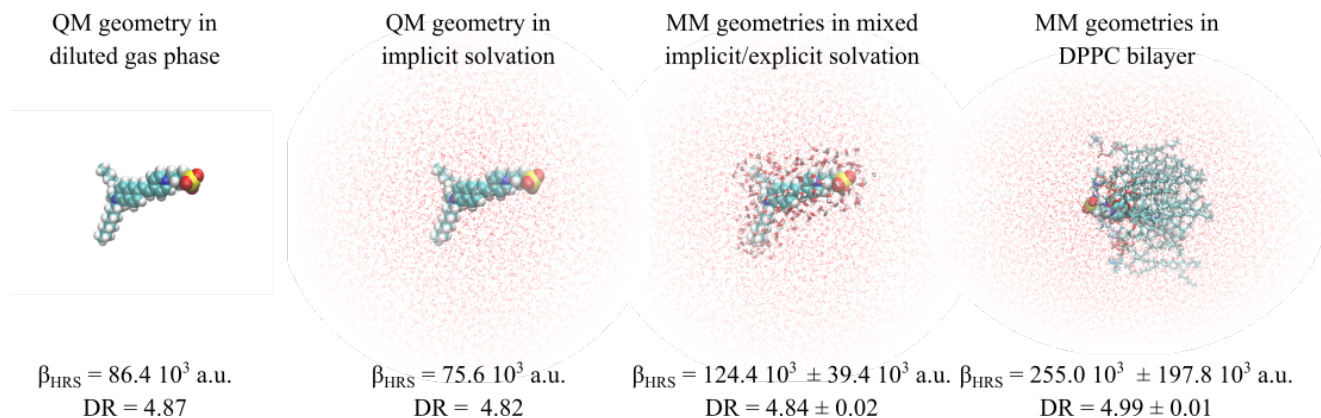

Figure 9.1 – TDDFT/M06-2X/6-311+G* β_{HRS} and DR ($\lambda = 1064\,\text{nm}$) of di-8-ANEPS computed in different environments : **i)** diluted gas phase; **ii)** water with implicit solvation; **iii)** water using mixed implicit and explicit solvations, and **iv)** DPPC bilayer.

Fot the simplest cases, i.e. in gas phase and in water using the implicit solvation, a single DFT-optimized (QM geometry) has been considered and therefore the compound is characterized by unique β_{HRS} responses. On the other hand, MD simulations generate a lot of snapshots, accounting for the dynamical behavior of the system. Therefore, for selected snapshots extracted from the MD simulations (MM geometries), the averages value and their standard deviations are presented. Environmental effects are first highlighted by the small decrease of β_{HRS} when going from the gas phase to the implicit aqueous phase (86.4 10^3 a.u. versus 75.6 10^3 a.u., respectively). This has been interpreted as resulting from a reduction of the acceptor character of the methyl-pyridinium group of the ANEP dyes by the solvent. Then, on the other hand, the inclusion of structural flexibility, which is achieved by using the MD snapshots, leads to a substantial increase of β_{HRS} of di-8-ANEPPS in water (124.4 10^3 $\pm$ 39.4 10^3 a.u.). The quite large standard deviations account for the geometrical fluctuations and the sensitivity of β_{HRS} to the geometry. Then, moving to the bilayer environment leads to another substantial increase of β_{HRS} (255.0 10^3 $\pm$ 197.8 10^3 a.u.), which highlights both the specific effects of the environment and of the dynamical behavior. Along the different models, DR remain more or less constant, adopting the characteristic value observed in push-pull molecules.

A major contribution of this Master Thesis was the elaboration of a general method to predict and subsequently analyze β of chromophores in real environments. It consists of a two-step procedure, combining MM and QM levels of calculations. For the MM part, the FFs used during the simulations were validated and/or re-parametrized. This was done to make sure that they could either reproduce the bulk properties of the environments (SPC/Fw for water and C36 for lipid) or reproduce the NLO responses of the chromophore (GAFF for chromophore), with respect to the QM geometry. In the case of the QM calculations, the M06-2X functional and the 6-311+G* basis were selected.

Finally, this work was made possible thanks to the increase of high performance computing power, which allows larger and longer simulations. This was particularly important when dealing with the second research axis. Indeed, to represent accurately those surroundings, a large number of molecules (i.e. a large number of atoms) have to be included into the calculations. Finally, because biological membranes are generally found in L_α phase, meaningful and useful atomic level models must be dynamic rather than static, which multiply the number of calculations via the number of snapshots.

Chapter 10

Perspectives

The elaboration and validation of this MD-then-QM method open the field of applications and characterization of SHIM chromophores in biological environments. Immediate future targets consist in studying other dyes in the same DPPC lipid bilayer environment and in analyzing their SHG responses as a function of their structures. As discussed in Chapter 7, the length of the alkyl substituents, the position of donor/acceptor substituents, as well as of the π-conjugated linker can be varied. Would these structure variations modify the position and orientation of the chromophore in the leaflet, its dynamics, and consequently its SHG response? Another family to assess includes the chiral dyes, having the ability to provide a SHG signal even when both leaflets are stained. These investigations of chromophores in bilayers will be accompanied by their characterization in solvents of various polarity, including non-polar solvents since they could model the hydrophobic environments created by the lipid alkyl chains inside the cell membranes.

A longer-term objective is the study of a selected chromophore, e. g. di-8-ANEPPS, in various lipid bilayers environments, and the assessment of the variations of the SHG response when the lipid composition is altered. Moreover, we aim at studying the variations of the SHG response as a function of the membrane potential, which results from differences of ions concentrations between the inner and outer bilayer regions. These investigations and rationalizations in terms of structure-property relationships will open the way towards the SHIM characterization of cellular structural modifications caused by diseases. In addition, they will contribute finding the best chromophores, exhibiting the largest contrasts, for revealing these structure/composition modifications.

Part V

References

Bibliography

[1] Thomas, J. A. Optical Imaging Probes for Biomolecules: An Introductory Perspective. *Chem. Soc. Rev.* **2015**, *44*, 4494–4500.

[2] Freund, I.; Deutsch, M.; Sprecher, A. Optical Second-Harmonic Microscopy, Crossed-beam Summation, and Small-Angle Scattering in Rat-tail Tendon. *Biophys. J.* **1986**, *50*, 693–712.

[3] Brown, R. M.; Millard, A. C.; Campagnola, P. J. Macromolecular Structure of Cellulose studied by Second-Harmonic Generation Imaging Microscopy. *Opt. Lett.* **2003**, *28*, 2207–2209.

[4] Campagnola, P. J.; de Wei, M.; Loew, L. M. High-Resolution Nonlinear Optical Imaging of Live Cells by Second Harmonic Generation. *Biophys. J.* **1999**, *77*, 3341–3349.

[5] Moreaux, L.; Sandre, O.; Mertz, J. Membrane Imaging by Second-Harmonic Generation Microscopy. *J. Opt. Soc. Am.* **2000**, *17*, 1685–1694.

[6] Moreaux, L.; Sandre, O.; Charpak, S.; Blanchard-Desce, M.; Mertz, J. Coherent Scattering in Multi-Harmonic Light Microscopy. *Biophys. J.* **2001**, *80*, 1588–1574.

[7] Kobayashi, M.; Fujita, K.; Kaneko, T. Second-Harmonic-Generation Microscope with a Microlens Array Scanner. *Opt. Lett.* **2002**, *27*, 1324–1326.

[8] Ries, R. S.; Choi, H.; Blunck, R.; Bezanilla, F.; Heath, J. R. Black Lipid Membranes: Visualizing the Structure, Dynamics, and Substrate Dependence. *J. Phys. Chem. B* **2004**, *108*, 16040–16049.

[9] Millard, A. C.; Jin, L.; de Wei, M.; Wuskell, J. P.; Lewis, A.; Loew, L. M. Sensitivity of Second Harmonic Generation from Styryl Dyes to Transmembrane Potential. *Biophys. J.* **2004**, *69*, 1169–1176.

[10] Millard, A. C.; Terasaki, M.; Loew, L. M. Second Harmonic Imaging of Exocytosis at Fertilization. *Biophys. J.* **2005**, *88*, 46–48.

[11] Bouevitch, O.; Lewis, A.; Pinevsky, I.; Wuskell, J.; Loew, L. Probing Membrane Potential with Nonlinear Optics. *Biophys. J.* **1993**, *65*, 672–679.

[12] Ben-Oren, I.; Peleg, G.; Lewis, A.; Minke, B.; Loew, L. Infrared Nonlinear Optical Measurements of Membrane Potential in Photoreceptor Cells. *Biophys. J.* **1996**, *71*, 1616–1620.

[13] Millard, A. C.; Jin, L.; Lewis, A.; Loew, L. M. Direct Measurement of the Voltage Sensitivity of Second-Harmonic Generation from Membrane Dye in Patch-Clamped Cells. *Opt. Lett.* **2003**, *28*, 1221–1223.

[14] Fluhler, E.; Burnham, V. G.; Loew, L. M. Spectra, Membrane Binding, and Potentiometric Responses of New Charge Shift Probes. *Biochemistry* **1985**, *24*, 5749–5755.

[15] Loew, L. M. Potentiometric Dyes: Imaging Electrical Activity of Cell Membranes. *Pure and Appl. Chem.* **1996**, *68*, 1405–1409.

[16] Reeve, J. E.; Anderson, H. L.; Clays, K. Dyes for Biological Second Harmonic Generation Imaging. *Phys. Chem. Chem. Phys.* **2010**, *12*, 13484–13498.

[17] Sanderson, M. J.; Smith, I.; Parker, I.; Bootman, M. D. Fluorescence Microscopy. *Cold Spring Harb Protoc.* **2014**, *10*, 1042–1065.

[18] Clays, K.; Persoons, A. Hyper-Rayleigh Scattering in Solution. *Phys. Rev. Lett.* **1991**, *66*, 2980–2983.

[19] Kishida, H.; Hasegawa, T.; Iwasa, Y.; Koda, T.; Tokura, Y.; Tachibana, H.; Matsumoto, M.; Wada, S.; Lay, T. T.; Tashiro, H. Electric-Field-Induced Second-Harmonic Generation Mediated by One-Dimensional Excitons in Polysilanes. *Phys. Rev. B* **1994**, *50*, 7786–7792.

[20] Manaka, T.; Iwamoto, M. Optical Second-Harmonic Generation Measurement for Probing Organic Device Operation. *Light Sci. Appl.* **2016**, *5*, 1–10.

[21] Franken, P. A.; Hill, A. E.; Peters, C. W.; Weinreich, G. Generation of Optical Harmonics. *Phys. Rev. Lett.* **1961**, *7*, 118–120.

[22] Shen, Y. R. Surface Properties Probed by Second-Harmonic and Sum-Frequency Generation. *Nature* **1989**, *337*, 519–525.

[23] Eisenthal, K. B. Liquid Interfaces Probed by Second-Harmonic and Sum-Frequency Spectroscopy. *Chem. Rev.* **1996**, *96*, 1343–1360.

[24] Sheppard, C.; Gannaway, J.; Kompfner, R.; Walsh, D. The Scanning Optical Microscope. *IEEE J. Quantum Electron* **1977**, *13*, 912.

[25] Radojević, S. K. Z. L. V.; Milutinović, A.; Romčević, M.; Romčević, N.; Valčić, A. Study of Structural and Optical Properties of YAG and Nd:YAG Single Crystals. *Mater. Res. Bull.* **2015**, *63*, 80–87.

[26] Campagnola, P. J.; Millard, A. C.; Terasaki, M.; Hoppe, P. E.; Malone, C. J.; Mohler, W. A. Three-Dimensional High-Resolution Second-Harmonic Generation Imaging of Endogenous Structural Proteins in Biological Tissues. *Biophys. J.* **2002**, *81*, 493–508.

[27] Montana, V.; Farkas, D. L.; Loew, L. M. Dual-Wavelength Fluorescence Measurements of Membrane Potential. *Biochemistry* **1989**, *28*, 4536–4539.

[28] Rusu, C. F.; Laning, H.; Othersen, O. G.; Kryschi, C.; Clark, T. Monitoring Biological Menbrane-Potential Changes: A CI QM/MM Study. *J. Phys. Chem. B* **2008**, *112*, 2445–2455.

[29] Gailhouste, L.; Grand, Y. L.; Odin, C.; Guyader, D.; B.Turlin,; Ezan, F.; Deesille, Y.; Guilbert, T.; Bessard, A.; Freemin, C.; Theret, N.; Baffet, G. Fibrillar Collagen Scoring by Second Harmonic Microscopy: A New Tool in the Assessment of Liver Fibrosis. *Hepatology* **2010**, *52*, 398–406.

[30] Shelton, D. P.; Rice, J. E. Measurements and Calculations of the Hyperpolarizabilities of Atoms and Small Molecules in the Gas Phase. *Chem. Rev.* **1994**, *94*, 3–29.

[31] Verbiest, T.; Clays, K.; Rodriguez, V. *Second-Order Nonlinear Optical Characterization Techniques: An Introduction*; CRC Press, 2009.

[32] Barzoukas, M.; Runser, C.; Fort, A.; Blanchard-Desce, M. A Two-State Description of (hyper) Polarizabilities of Push-Pull Molecules Based on a Two-Form Model. *Chem. Phys. Lett.* **1996**, *257*, 531–537.

[33] Bourhill, G.; Brédas, J.-L.; Cheng, L.-T.; Marder, S. R.; Meyers, F.; Perry, J. W.; Tiemann, B. G. Experimental Demonstration of the Dependence of the First Hyperpolarizability of Donor-Acceptor-Substituted Polyenes on the Ground-State Polarization and Bond Length Alternation. *J. Am. Chem. Soc.* **1994**, *116*, 2619 – 2620.

[34] Oudar, J. L. Optical Nonlinearities of Conjugated Molecules. Stilbene Derivatives and Highly Polar Aromatic Compounds. *J. Chem. Phys.* **1977**, *67*, 446–457.

[35] Oudar, J. L.; Chemla, D. S. Hyperpolarizabilities of the Nitroanilines and their Relations to the Excited State Dipole Moment. *J. Chem. Phys.* **1977**, *66*, 2264–2268.

[36] Peleg, G.; Lewis, A.; Linial, M.; Loew, L. M. Nonlinear Optical Measurements of Membrane Potential around Single Molecules at Selected Cellular Sites. *Proc. Natl. Acad. Sci.* **1999**, *96*, 6700–6704.

[37] Alberts, B.; Johnson, A.; Lewis, J. *The Lipid Bilayer from Molecular Biology of the Cell. 4th edition*; Garland Science, 2002.

[38] Yeagle, P. *The Structure of Biological Membranes, 3rd edition.*; CRC Press, 2011.

[39] Harayama, T.; Riezman, H. Understanding the Diversity of Membrane Lipid Composition. *Nat. Rev. Mol. Cell. Biol.* **2018**, *19*, 281–296.

[40] Takaoka, Y.; Pasenkiewicz-Gierula, M.; Miyagawa, H.; Kitamura, K.; Tamura, Y.; Kusumi, A. Molecular Dynamics Generation of Nonaribtrary Membrane Models Reveals Lipid Orientational Correlations. *Biophys. J.* **2000**, *79*, 3118–3138.

[41] McWeeny, R. *Methods of Molecular Quantum Mechanics, 2nd edition*; Academic Press, 1992.

[42] Szabo, A.; Ostlund, N. S. *Modern Quantum Chemistry: Introduction to Advanced Electronic Structure Theory*; Dover Publications, 1996.

[43] Hurley, A. C. *Electron Correlation in Small Molecules*; Academic Press, 1976.

[44] Dunning, T. H. Gaussian Basis Functions for Use in Molecular Calculations. III. Contraction of (10s6p) Atomic Basis Sets for the FirstRow Atoms. *J. Chem. Phys.* **1971**, *55*, 716–723.

[45] Huzinaga, S. *Gaussian Basis Sets for Molecular Calculations*; Elsevier Science, 1984.

[46] Poirier, R.; Kari, R.; Csizmadia, I. G. *Handbook of Gaussian Basis Sets*; Elsevier Science, 1985.

[47] K. I. Ramachandran, K. N., G. Deepa *Computational Chemistry and Molecular Modeling: Principles and Applications*; Springer-Verlag Berlin Heidelberg, 2008.

[48] Karna, S. P.; Dupuis, M. Frequency Dependent Nonlinear Optical Properties of Molecules:

Formulation and Implementation in the HONDO Program. *J Comput. Chem.* **1991**, *12*, 487–504.

[49] Parr, R. G.; Yang, W. *Density-Functional Theory of Atoms and Molecules*; Oxford University Press, 1989.

[50] Koch, W.; Holthausen, M. C. *A Chemist's Guide to Density Functional Theory, 2nd edition*; Wiley-VCH Verlag GmbH, 2001.

[51] Hohenberg, P.; Kohn, W. Inhomogeneous Electron Gas. *Phys. Rev.* **1964**, *136*, 864–871.

[52] Cohen, A. J.; Mori-Sánchez, P.; Yang, W. Challenges for Density Functional Theory. *Chem. Rev.* **2012**, *112*, 289–320.

[53] Tsuneda, T. *Density Functional Thoery in Quantum Chemistry*; Springer Japan, 2014.

[54] Biscout, D.; Martin, F. *Quantum Mechanical Simulation Methods for Studying Biological Systems*; Springer-Verlag Berlin Heidelberg, 1996.

[55] Kohn, W.; Becke, A. D.; Parr, R. G. Density Functional Theory of Electronic Structure. *J. Phys. Chem.* **1996**, *100*, 12974–12980.

[56] Perdew, J. P.; Schmidt, K. Jacob's Ladder of Density Functional Approximations for the Exchange-Correlation Energy. *AIP Conf. Proc.* **2001**, *577*, 1–20.

[57] Perdew, J. P.; Ruzsinszky, A.; Tao, J.; Staroverov, V. N.; Scuseria, G. E. Prescription for the Design and Selection of Density Functional Approximations: More Constraint Satisfaction with Fewer Fits. *J. Chem. Phys.* **2005**, *123*, 062201.

[58] Grimme, S.; Neese, F. Double-Hybrid Density Functional Theory for Excited Electronic States of Molecules. *J. Chem. Phys.* **2007**, *127*, 154116.

[59] Grimme, S. Density Functional Theory with London Dispersion Corrections. *Comput. Mol. Sci.* **2011**, *1*, 211–228.

[60] Walker, M.; Harvey, A. J. A.; Sen, A.; Dessent, C. E. H. Performance of M06, M06-2X, and M06-HF Density Functionals for Conformationally Flexible Anionic Clusters: M06 Functionals Perform Better than B3LYP for a Model System with Dispersion and Ionic Hydrogen-Bonding Interactions. *J. Phys. Chem. A* **2013**, *117*, 12590–12600.

[61] Zhao, Y.; Truhlar, D. G. The M06 Suite of Density Functionals for Main Group Thermochemistry, Thermochemical Kinetics, Noncovalent Interactions, Excited States, and Transition Elements: Two New Functionals and Systematic Testing of Four M06-Class Functionals and 12 Other Functionals. *Theor. Chem. Acc.* **2008**, *120*, 215–241.

[62] Runge, E.; Gross, E. K. U. Density-Functional Theory for Time-Dependent Systems. *Phys. Rev. Lett.* **1984**, *52*, 997–1000.

[63] Marques, M. A. L.; Ulrich, C. A.; Nogueira, F.; Rubio, A.; Burke, K.; Gross, E. K. U. *Time-Dependent Density-Functional Theory*; Springer Berlin Heidelberg New York, 2006.

[64] Petersilka, M.; Gossmann, U. J.; Gross, E. K. U. Excitation Energies from Time-Dependent Density-Functional Theory. *Phys. Rev. Lett.* **1996**, *76*, 1212–1215.

[65] Peach, M. J. G.; Benfield, P.; Helgaker, T.; Tozer, D. J. Excitation Energies in Density

Functional Theory: An Evaluation and a Diagnostic Test. *J. Chem. Phys.* **2008**, *128*, 044118.

[66] Bauernschmitt, R.; Ahlrichs, R. Treatment of Electronic Excitations within the Adiabatic Approximation of Time Dependent Density Functional Theory. *Chem. Phys. Lett.* **1996**, *256*, 454–464.

[67] Seminario, J. M. *Recent Developments and Applications of Modern Density Functional Theory*; Elsevier Science, 1996; Vol. 4.

[68] Jacquemin, D.; Perpète, E. A.; Ciofini, I.; Adamo, C.; Valero, R.; Zhao, Y.; Truhlar, D. G. On the Performances of the M06 Family of Density Functionals for Electronic Excitation Energies. *J. Chem. Theory Comput.* **2010**, *6*, 2071–2085.

[69] Mennucci, B.; Cancès, E.; Tomasi, J. Evaluation of Solvent Effects in Isotropic and Anisotropic Dielectrics and in Ionic Solutions with a Unified Integral Equation Method: Theoretical Bases, Computational Implementation, and Numerical Applications. *J. Chem. Phys. B* **1997**, *101*, 10506–10517.

[70] Miertus, S.; Scrocco, E.; Tomasi, J. Electrostatic Interactions of a Solute with a Continuum. A direct Utilization of Ab Initio Molecular Potrialls for the Prevision of Solvent Effects. *Chem. Phys.* **1981**, *55*, 117–129.

[71] Tomasi, J.; Mennucci, B.; Cammi, R. Quantum Mechanical Continuum Solvation Models. *Chem. Rev.* **2005**, *105*, 2999−3093.

[72] Lipkowitz, K. B.; Boyd, D. B. *Reviews in Computational Chemistry II*; Wiley-VCH, 1991.

[73] Phillips, J.; Braun, R.; Wang, W.; Gumbart, J.; Tajkhorshid, E.; Villa, E.; Chipot, C.; Skeel, R.; Kalé, L.; Schulten, K. Scalable Molecular Dynamics with NAMD. *J. Comput. Chem.* **2005**, *26*, 1781–1802.

[74] Rapaport, D. C. *The Art of Molecular Dynamics Simulation*; Cambridge University Press, 2004.

[75] Attig, N.; Binder, K.; Grubmüller, H.; Kremer, K. *Computational Soft Matter: From Synthetic Polymers to Proteins, Lecture Notes*; NIC Series, 2004; Vol. 23.

[76] Tsai, D. H. The Virial Theorem and Stress Calculation in Molecular Dynamics. *J. Chem. Phys.* **1979**, *70*, 1375–1382.

[77] Berendsen, H. J. C.; Postma, J. P. M.; van Gunsteren, W. F.; DiNola, A.; Haak, J. Molecular Dynamics with Coupling to an External Bath. *J. Chem. Phys.* **1998**, *81*, 3684–3690.

[78] Tieleman, D. P.; Berendsen, H. J. Molecular Dynamics Simulations of A Fully Hydrated Dipalmitoylphosphatidylcholine Bilayer with Different Macroscopic Boundary Conditions and Parameters. *J. Chem. Phys.* **1998**, *105*, 4871–4880.

[79] Sankararamakrishnan, R.; Weinstein, H. Surface Tension Parametrization in Molecular Dynalics Simulations of a Phosholipid-Bilayer Membrane: Calibration and Effects. *J. Phys. Chem. B* **2004**, *108*, 11802–11811.

[80] Barker, J. A.; Henderson, D. What is "liquid"? Understanding the States of Matter. *Rev. Mod. Phys.* **1976**, *48*, 587 – 671.

[81] Piana, S.; Lindorff-Larsen, K.; Dirks, R. M.; Salmon, J. K.; Dror, R. O.; Shaw, D. E. Evaluating the Effects of Cutoffs and Treatment of Long-range Electrostatics in Protein Folding Simulations. *PLOS ONE* **2012**, *7*, 1–6.

[82] Frisch, M. J. et al. Gaussian 16 Revision A.03. 2016; Gaussian Inc. Wallingford CT.

[83] Martinez, L.; Andrade, R.; Birgin, E. G.; Martinez, J. M. Packmol: A Package for Building Initial Configurations for Molecular Dynamics Simulations. *J. Comput. Chem.* **2009**, *30*, 2157–2164.

[84] Husslein, T. D.; Newns, P. C.; Pattnaik, Q.; Moore, P. B. Constant Pressure and Temperature Molecular Dynamics Simulation of the Hydrated Diphytanolphosphatidylcholine Lipid Bilayer. *J. Chem. Phys.* **1998**, *109*, 2826–2832.

[85] Tu, K.; Tobias, D. J.; Blasie, J. K.; Klein, M. L. Molecular Dynamis Investigation of the Structure of a Fully Hydrated Gel-Phase Dipalmitoylphosphatidylcholine Bilayer. *Biophys. J.* **1996**, *70*, 595–608.

[86] Humphrey, W.; Dalke, A.; Schulten, K. VMD: Visual Molecular Dynamics. *J. Molec. Graphics* **1996**, *14*, 33–38.

[87] Wu, Y.; Tepper, H. L.; Voth, G. A. Flexible Simple Point-Charge Water Model with Improved Liquid-State Properties. *J. Chem. Phys.* **2006**, *124*, 024503.

[88] Wang, J.; Wolf, R. M.; Caldwell, J. W.; Kollman, P. A.; Case, D. A. Development and Testing of a General Amber Force Field. *J. Comput. Chem.* **2004**, *25*, 1157–1174.

[89] van der Ploeg, P.; Berendsen, H. J. C. Molecular Dynamics Simulation of a Bilayer Membrane. *J. Chem. Phys.* **1982**, *76*, 3271–3276.

[90] Tu, K.; Klein, D. J. T. M. L. Constant Pressure and Temperature Molecular Dynamics Simulation of a Fully Hydrated Liquid Crystal Phase Dipalmitoylphosphatidylcholine Bilayer. *Biophys. J.* **1995**, *69*, 2558–2562.

[91] Berger, O.; Edholm, O.; Jähnig, F. Molecular Dynamics Simulations of a Fluid Bilayer of Dipalmitoylphosphatidylcholine at Full Hydration, Constant Pressure, and Constant Temperature. *Biophys. J.* **1997**, *72*, 2002–2013.

[92] Feller, S. E.; Yin, D.; Pastor, E. W.; MacKerell, A. D. Molecular Dynamics Simulation of Unsaturated Lipid Bilayers at Low Hydration: Parameterization and Comparison with Diffraction Studies. *Biophys. J.* **1997**, *73*, 2269–2279.

[93] Marrink, S. J.; Berger, O.; Tieleman, P.; Jähnig, F. Adhesion Forces of Lipids in a Phospholipid Membrane Studied by Molecular Dynamics Simulations. *Biophys. J.* **1998**, *74*, 931–943.

[94] Forest, L. R.; Sansom, M. S. Membrane Simulations: Bigger and Better? *Curr. Opin. Struct. Biol.* **2000**, *10*, 174–181.

[95] Mashl, R. J.; Scott, H. L.; Subramaniam, S.; Jakobsson, E. Molecular Simulation of Dioleoylphosphatidylcholine Lipid Bilayers at Differing Levels of Hydration. *Biophys. J.* **2001**, *81*, 3005–3015.

[96] Mukhopadhyay, P.; Tieleman, L. M. D. P. Molecular Dynamics Simulation of a Palmitoyl-

Oleoyl Phosphatidylserine Bilayer with Na$^+$ Counterions and NaCl. *Biophys. J.* **2004**, *86*, 1601–1609.

[97] Benz, R. W.; Castro-Roman, F.; Tobias, D. J.; H., S. Experimental Validation of Molecular Dynamics Simulations of Lipid Bilayers: A New Approach. *Biophys. J.* **2005**, *88*, 805–817.

[98] Klauda, J. B.; Venable, R. M.; Freites, J. A.; o'Connor, J. W.; Tobias, D. T.; Mondragon-Ramirez, C.; Vorobyov, I.; Jr., A. D. M.; Pastor, R. W. Update of the CHARMM All-Atom Additive Force Field for Lipids: Validation on Six Lipid Types. *J. Phys. Chem. B* **2010**, *114*, 7830–7843.

[99] Robinson, D.; Besley, N. A.; O'Shea, P.; Hirst, J. D. Di-8-ANEPPS Emission Spectra in Phospholipid/Cholesterol Membranes: A Theoretical Study. *J. Phys. Chem. B* **2011**, *115*, 4160 – 4167.

[100] Jämbeck, J. P. M.; Lyubartsev, A. P. Derivation and Systematic Validation of a Refined All-Atom Force Field for Phosphatidylcholine lipids. *J. Phys. Chem. B* **2012**, *116*, 3164–3179.

[101] Jurkiewicz, P.; Cwiklik, L.; Vojtiskova, A.; Jungwirth, P.; Hoff, M. Structure, Dynamics, and Hydration of POPC/POPS Bilayers Suspended in NaCl, KCl, and CsCl Solutions. *Bioch. Biophys. Acta* **2012**, *1818*, 609–616.

[102] Mori, T.; Miyashita, N.; Im, W.; Feig, M.; Sugita, Y. Molecular Dyanmics Simulations of Biological Membranes and Membranes Proteins Using Enhanced Conformational Sampling Algorithms. *Bioch. Biophys. Acta* **2016**, *1858*, 1635–1651.

[103] Lyubartsev, A. P.; Rabinovich, A. L. Force Field Develpment for Lipid Membrane Simulations. *Bioch. Biophys. Acta* **2016**, *1858*, 2483–2497.

[104] Macchiagodena, M.; Frate, G. D.; Brancato, G.; Chandramouli, B.; Mancini, G.; Barone, V. Computational Study of DPAP Molecular Rotor in Various Environments: from Force Field Development to Molecular Dynamic Simulations and Spectroscopic Calculations. *Phys. Chem. Chem. Phys.* **2017**, *2*, 30590–30602.

[105] Ruocco, M. J.; Shipley, G. G. Characterization of the Sub-Transition of Hydrated Dipalmitoylphosphatidylcholine Bilayers. Kinetic, Hydration and Structural Study. *Biochim. Biophys. Acta* **1982**, *691*, 309–320.

[106] Inoko, Y.; Mitsui, T. Structural Parameters of dipalmitoyl phosphatidylcholine lamellar phases and bilayer phase transitions. *J. Phys. Soc. Japan* **1978**, *44*, 1918–1924.

[107] Janiak, M. J.; Small, D. M.; Shipley, G. G. Nature of the Thermal Pretransition of Synthetic Phospholipids: Dimyristoyl- and Dipalmitoyllecithin. *Biochemistry* **1976**, *15*, 4575–4580.

[108] Pastor, R. W.; Jr., A. D. M. Development of the CHARMM Force Field for Lipids. *J. Phys. Chem. Lett.* **2011**, 1526–1532.

[109] Feller, S. E.; Zhang, Y.; Pastor, R. W.; Brooks, B. R. Constant Pressure Molecular Dynmics Simulation: The Langevin Piston Method. *J. Chem. Phys.* **1995**, *103*, 4613–4621.

[110] Bishop, D. M.; Champagne, B.; Kirtman, B. Relationship Between Static Vibrational and Electronic Hyperpolarizabilities of π-Conjugated Push–Pull Molecules within the Two-State

Valence-Bond Charge-Transfer Model. *J. Chem. Phys.* **1198**, *109*, 9987–9994.

[111] Comer, J.; Gumbart, J. C.; Hénin, J.; Lelièvre, T.; Pohorille, A.; Chipot, C. The Adaptive Biasing Force Method: Everything You Always Wanted To Know but Were Afraid to Ask. *J. Phys. Chem.* **2015**, *119*, 1 219– 1151.

[112] Sorenson, J. M.; Hura, G.; Glaeser, R. M.; Head-Gordon, T. What Can X-Ray Scattering Tell us About the Radial Distribution Functions of Water? *J. Chem. Phys.* **2000**, *113*, 9149–9161.

[113] Soper, A.; Phillips, M. A New Determination of the Structure of Water at 25°C. *J. Chem. Phys.* **1986**, *107*, 47–60.

[114] Clark, G. N. I.; Cappa, C. D.; Smith, J. D.; Saykally, R. J.; Head-Gordon, T. The Structure of Ambient Water. *Mol. Phys.* **2010**, *108*, 1415–1433.

[115] Lide, D. R. *Handbook of Chemistry and Physics*; CRC Press, 2005.

[116] Maroulis, G. Hyperpolarizability of H_2O. *J. Chem. Phys.* **1991**, *94*, 1182–1190.

[117] Mackerell, A. D. Empirical Force Fields for Biological Macromolecules: Overview and Issues. *J. Comput. Chem.* **2004**, *25*, 1584–1604.

[118] Lis, L.; McAlister, M.; Fuller, N.; Rand, R. Interactions Between Neutral Phospholipid Bilayer Membranes. *Biophys. J.* **1982**, *37*, 657–665.

[119] Lewis, B. A.; Engelman, D. M. Lipid Bilayer Thickness Varies Linarly with Acyl Chain Length in Fluid Phosphatidylcholine Vesicle. *J. Mol. Biol.* **1983**, *166*, 211–217.

[120] Schindler, H.; Seelig, J. Deuterium Order Parameters in Relation to Thermodynamic Properties of a Phospholipid Bilayer. A Statistical Mechanical Interpretation. *Biochemistry* **1975**, *14*, 2283–2287.

[121] Pace, R.; Chan, S. Molecular Motions in Lipid Bilayers. III. Lateral and Transverse Diffusion in Bilayers. *J. Chem. Phys.* **1982**, *76*, 4241–4247.

[122] Young, L. D.; Dill, K. Solute Partitioning into Lipid Bilayer Membranes. *Biochemistry* **1988**, *27*, 5281–5289.

[123] Thurmond, R.; Dodd, S.; Brown, M. Molecular Areas of Phospholipids as Determined by H NMR Spectroscopy. *Biophys. J.* **1991**, *59*, 108–113.

[124] Egbert, E.; Marrink, S.-J.; Berendsen, H. J. C. Molecular Dynamics Simulation of a Phospholipid Membrane. *Eur. Biophys. J.* **1994**, *22*, 423–436.

[125] Chapman, D.; Williams, R. M.; Ladbrooke, B. D. Physical Studies of Phospholipids. *Chem. Phys.Lipid* **1967**, *1*, 445–475.

[126] Tardieu, A. V. Structure and Polymorphism of the Hydration Chains of Lipids. A Study of LecithinWwater Phases. *J. Mol. Biol.* **1973**, *75*, 711–733.

[127] Levine, Y. K. Physical Studies of Membrane Structure. *Prog. Biophys. Mol. Biol.* **1972**, *24*, 3–74.

[128] Levine, Y. K. X-Ray Diffraction Studies of Membranes. *Prog. Surf. Sci.* **1973**, *3*, 279–352.

[129] Hui, S. W. The Tilting of the Hydrocarbon Chains in a Single Bilayer of Phospholipid. *Chem.*

Phys. Lipids **1976**, *16*, 9–18.

[130] Janiak, M. J.; Small, D. M.; Shipley, G. G. Nature of the Thermal Pretransition of Synthetic Phospholipids: Dimyristoyl and Dipalmitoyl Lecithin. *Biochemistry* **1976**, *15*, 4575–4580.

[131] Büldt, G.; Gally, H. U.; Seelig, J. Neutron Diffraction Studies on Selectively Deuterated Phospholipid Bilayers. *Nature* **1978**, *271*, 180–184.

[132] Pasenkiewicz-Gierula, M.; Talaoka, Y.; Miyagawa, H.; Kitamura, K.; Kusumi, A. Hydrogen Bonding of Water to Phosphatidylcholine in the Membrane as Studied by a Molecular Dynamics Simulation: Location, Geometry, and Lipid-Lipid Bridging via Hydrogen-Bonded Water. *J. Phys. Chem. A* **1997**, *101*, 3677–3691.

[133] Arnold, K.; Pratsch, L.; Gawrisch, K. Effect of the Polyethylene Glycol on Phospholipid Hydration and Polarity of the External Phase. *Biochim. Biophys. Acta.* **1983**, *728*, 121–128.

[134] Disalvo, E. A. *Membrane Hydration. The Role of Water in the Structure and Function of Biological Membranes*; Springer International Publishing, 2015; Vol. 71.

[135] Finer, E. G.; Darke, D. Phospholipid Hydration Studied by Deuteron Magnetic Resonance Spectroscopy. *Chem. Phys. Lipids* **1974**, *12*, 1–16.

[136] Lopez, C. F.; Nielsen, S. O.; Klein, M. L.; Moore, P. B. Hydrogen Bonding Structure and Dynamics of Water at the Dimyristoylphosphatidylcholine Lipid Bilayer Surface from a Molecular Dynamics Simulation. *J. Phys. Chem. B* **2004**, *108*, 6603–6610.

[137] Seelig, A.; Seelig, J. The Dynamic Structure of Fatty Acyl Chains in a Phospholipid Bilayer Measured by Deuterium Magnetic Resonance. *Biochemistry* **1974**, *13*, 4839–4845.

[138] Seelig, A.; Seelig, J. Lipid Conformation in Model Membranes and Biological Membranes. *Quart Rev. Biophys.* **1980**, *13*, 19–61.

[139] Nagle, J. F. Area/Lipid of Bilayer from NMR. *Biophys. J.* **1993**, *64*, 1476–1481.

[140] Chiu, S.-W.; Clark, M.; Balaji, V.; Subramaniam, S.; Scott, H. L.; Jakobsson, E. Incorporation of Surface Tension into Molecular Dynamics Simulation of an Interface: A Fluid Phase Lipid Bilayer Membrane. *Biophys. J.* **1995**, *69*, 1230–1245.

[141] Damodaran, K.; Merz, K. A Comparison of DMPC- and DLPE-Based Lipid Bilayers. *Biophys. J.* **1994**, *66*, 1076–1087.

[142] Horvath, L. I.; Cirak, J.; Vigh, L. Relation of Raman Order Parameters to Spin Labeling Parameters. *Chem. Phys. Lipid* **1980**, *27*, 237–250.

[143] Meier, P.; Ohmes, E.; Kothe, G. Multipulse Dynamic Nuclear Magnetic Resonance of Phospholipid Membranes. *J. Chem. Phys.* **1986**, *85*, 3598–3614.